Fall 1995

Buckling Analysis and Optimum Design of Multidirectionally Stiffened Composite Curved Panel

Navin R. R. Jaunky
Old Dominion University

BUCKLING ANALYSIS AND OPTIMUM DESIGN OF MULTIDIRECTIONALLY STIFFENED COMPOSITE CURVED PANEL

NAVIN R. R. JAUNKY

BTECH (HONS) MAY 1988,
Indian Institute of Technology, Kharagpur, India

Master of Science, May 1993,
Old Dominion University, Norfolk, VA 23529

A Dissertation Submitted To The Faculty Of
Old Dominion University In Partial Fulfillment Of The
Requirements For The Degree of

DOCTOR OF PHILOSOPHY
MECHANICAL ENGINEERING

OLD DOMINION UNIVERSITY
DECEMBER 1995

Approved by:

Dr. Norman F. Knight, Jr.	Dr. Damodar R. Ambur
Dr. Gene J-W. Hou	Dr. Chuh Mei

ABSTRACT

BUCKLING ANALYSIS AND OPTIMUM DESIGN OF
MULTIDIRECTIONALLY STIFFENED
COMPOSITE CURVED PANEL

Navin Jaunky
Old Dominion University

Director: Dr. Norman F. Knight

Continuous filament grid-stiffened structure is a stiffening concept that combines structural efficiency and damage tolerance. However, buckle resistant design optimization of such structures using a finite element method is expensive and time consuming due to the number of design parameters that can be varied. An analytical optimization procedure which is simple, efficient and supports the preliminary design of grid-stiffened structures for application to combined loading cases is needed.

An analytical model for a general grid-stiffened curved panel is developed using an improved smeared theory with a first-order, shear-deformation theory to account for transverse shear flexibilities and local skin-stiffener interaction effects. The local skin-stiffener interaction effects are accounted for by computing the stiffness due to the stiffener and the skin in the skin-stiffener region using the neutral surface profile of the skin-stiffener semi-infinite plate model. The neutral surface profile for the skin-stiffener semi-infinite plate model is obtained analytically using a stress function approach, minimum potential energy principle, and statics conditions.

Analysis methods for buckling of general parallelogram-shaped and general triangular-shaped curved panels are developed. These analyses are required in order

to assess the local buckling of grid-stiffened curved skin segments. The buckling analysis makes use of "circulation" functions as Ritz functions which account for material anisotropy and different boundary conditions. The local buckling of stiffener segments between stiffener interaction points are also assessed.

Using these analyses and a genetic algorithm as optimizer, an optimization tool is developed for minimum weight design of composite grid-stiffened panel subjected to combined in-plane loads with a global buckling design constraint. Design variables are the axial and transverse stiffener spacings, the stiffener height and thickness, and the stiffener pattern.

Results are presented for buckling loads of composite grid-stiffened panels which are obtained using the improved smeared theory and are compared with detailed finite element analysis. Buckling loads for anisotropic skewed and triangular plates, and curved panels are presented and compared with results from finite element analysis. Finally, designs for grid-stiffened panels obtained using the design optimization process are presented.

ACKNOWLEDGEMENTS

I am very grateful and obliged to my advisor Dr. N. F. Knight Jr. for giving me the opportunity to work with him, to the Structural Mechanics Branch of NASA Langley Research Center, especially to Dr. D. R. Ambur and Dr. J. H. Starnes Jr. for providing me with the opportunity to participate in on-site research at a research center of prime importance such as NASA Langley Research Center. The valuable advice by Dr N. F. Knight Jr., as thesis advisor and Dr. D. R. Ambur as grant technical monitor is deeply appreciated.

I show the same gratitude to the other committee members, namely Dr. Gene Hou and Dr. C. Mei, for their cooperation. The support from the School of Mechanical and Aerospace Engineering as a graduate teaching assistant is acknowledged. Assistance from some other members of the Structural Mechanics Branch, and friends is hereby also gratefully acknowledged.

Finally, I deeply appreciate the continuous encouragement of my parents, brother and his wife, all my relatives, and close friends.

This research was supported by the NASA Contract NAS1-19858, Task No. 21 and NASA Grant NAG-1-1588.

Navin Jaunky

November 1995

TABLE OF CONTENTS

LIST OF TABLES

LIST OF FIGURES

Chapter 1

INTRODUCTION

1.1 MOTIVATION

In aircraft structures, structural efficiency dictates that most of the primary structure be of stiffened construction. In conventional metallic structures, stiffened structures are assemblies predominantly of a large number of structural elements including skin, stringers, spars, ribs, and clips put together by bonding or mechanically fastening them together. Such an approach is not cost effective due to a large part count and assembly costs. Metallic structures are susceptible to corrosion and fatigue problems which need additional expensive treatments and periodic inspections to prolong their life considerably. The advent of composite materials makes it possible to overcome most of these problems if structures utilizing these materials are designed to exploit their improved mechanical properties, tailorability, and fabricated in a cost-effective manner.

The types of composite materials that are widely used in primary structural applications are graphite-epoxy material systems. These materials have high specific modulus and strength to make them efficient for aircraft structural applications. Corrosion problems that are typical of most metallic structures are virtually eliminated, and the designs are mostly driven by static-strength requirements rather than fatigue-life considerations. But composite structures are generally more expensive

than metallic structures due to their high material and manufacturing costs. There is potential for composite structural cost reductions by using automated manufacturing processes to make large subassemblies in a single process. Such efforts led to cocuring/cobonding processes which dramatically reduce part count. With higher utilization of composite materials in larger transport aircraft and in a variety of other classes of aircraft, the material cost per pound is expected to come down making composites a viable structural material.

The design driver for the current generation graphite-epoxy materials is their tolerance to low-velocity impact damage. Even at impact velocities that result in barely visible damage, the residual strength of composite structures reduces by half compared to undamaged laminates. For this reason, the damage tolerance constraint limits the applied strains to about 4500μ *in./in.*, even though commonly used composite laminates are capable of loading to $10{,}000\mu$ *in./in.*

Continuous filament grid-stiffened structural design concept [1] is a damage tolerant stiffening concept that combines the structural efficiency of a stiffened structure with the advantages of composite materials in an automated manufacturing process. High volume manufacturing processes like filament winding and tow placement, have been used in the past to produce these structures in a cost efficient manner [2],[3].

In aerospace vehicles, most of the structural components have a curved panel geometry. The fuselage structure of an aircraft can be designed as an assembly of curved panels of different radii. Figure 1.1 shows a typical aircraft fuselage construction. The fuselage is in general a non-circular cylinder, but the portion between two bulkheads and longerons approximates a simply-supported cylindrical panel. Design configurations for a grid-stiffened shell [4] include isogrid, orthogrid or generalized orthogrid layout of stiffener.

Composite grid-stiffening structures are efficient as they utilize the 0° fibers placed along the length of the stiffener for large axial and bending stiffnesses. Unlike prismatically and orthogonally stiffened structures, the general grid-stiffened structures have diagonal stiffeners which are capable of carrying inplane shear due to fuselage twisting. The improved damage tolerance of grid-stiffened structures is due to a multiplicity of load paths to redistribute the loads [3].

Continuous filament grid-stiffened structures also present structural stiffness tailoring possibilities by skewing the stiffener with respect to load direction [4],[5] and tapering the height of the stiffeners in the grid along both length and width of the stiffened panel.

An aircraft in flight is subjected to air loads which are imposed by maneuver and gusts. Figure 1.2 shows typical aerodynamic force resultants experienced by an aircraft in steady flight. These force resultants act on isolated curved segments of the fuselage as shown in Figure 1.1 The aerodynamic drag acting on the fuselage and the bending moment due to the lift on the fuselage induce an axial loading which changes from tension to compression around the fuselage. Cabin pressure results in circumferential or hoop tensile loading and a tensile axial load as well. In-plane shear loading results from load transfer between bulkheads and longitudinal frames, due to rolling and yawing of the aircraft, since these motions involve a differential lift on the wings and from gust loading on the vertical fin. This combined load state may cause a panel segment of the fuselage to buckle. The deformation pattern associated with a buckling load may be an overall or global mode or it may be local to some segment of the fuselage or to a panel skin or stiffener element. A need for understanding the buckling response of general composite grid-stiffened curved panels subjected to combined loading is needed in order to identify the best-suited geometries for different locations of fuselage and wing structures since loading conditions on these structures is a function of spatial variables. Additionally, understanding the buckling response

of general grid-stiffened curved panel with variable curvature is needed in order to identify best-suited geometries for fuselage and wing cross-sections.

1.2 REVIEW OF PAST WORK

Most of the research work on stiffened panels presented in the literature addresses axially stiffened panels subjected to compression. A limited amount of work has been reported on stiffened panels subjected to combined in-plane loading. Axially stiffened prismatic panels subjected to axial compression and in-plane shear was considered by Stroud, Greene and Anderson [6]. Stroud et. al. [6] used complex Fourier series in their analysis and compared their results with finite element analysis. Their solution was essentially exact for axially stiffened panels subjected to axial compression. Gendron and Gurdal [7] considered grid-stiffened composite cylindrical shells subjected to axial compression and torsional shear loadings. They used finite element analysis and a gradient based optimizer to optimize composite grid-stiffened cylinders. Finite element analysis was again used by Rao and Tripathy [8] for buckling analysis of composite orthogrid cylindrical panels. They used the method of ranking to determine the optimum lay-up for orthogrid skins. Buckling of grid-stiffened cylindrical shells subjected to combined in-plane loading is reported by Reddy, Valisetty, and Rehfield [9]. A smeared stiffener approach was used to obtain the global buckling response for the cylindrical shells and simplified analysis was used to determine the local buckling response of skin and stiffener segments.

Apart from the published research work on buckling of stiffened plates and shells utilizing the finite element method, research work on buckling of stiffened plates and shells utilize three different modeling approaches. These approaches are method of elastic equivalence or smeared stiffener approach, the column approach, and discrete stiffener plate approach.

In the first approach, the stiffness of the stiffeners are "smeared" over the panel, and the final equilibrium equations for a generally orthotropic panel are then solved numerically (e.g., see [9]-[17]). In Ref. [9] and [17], a First-Order Shear-Deformation Theory (FSDT) [18] has been used in constructing the smeared stiffener approach. The smeared stiffener approach is applicable in general to stiffened panels where the local buckling load is equal to or greater than the global buckling load. This approach for preliminary design is consistent with the widely used aeronautical design philosophy where the design goal is a buckling-resistant design. As observed in Refs. [6],[7] and [17], the traditional or conventional smeared stiffener approach may overestimate the buckling load of stiffened panels for a certain range of geometric parameters because the traditional smeared stiffener approach does not account for local skin-stiffener interactions. This effect should be included in an improved smeared stiffener approach to make the approach a more reliable tool for the analysis and design of grid-stiffened panels.

The column approach [19] has been widely used in design codes due to its simplicity. Here it is assumed that the portion of the stiffened panel between the stiffeners can be modeled mathematically as a uniformly compressed plate, simply supported along its loaded edges and built-in or clamped along its unloaded edges (i.e., those abutting the stiffeners) The compressive force and bending moment on the section can be derived as functions of the local and overall buckling deflections. This approach has been extensively used in studying interaction phenomena between local and global buckling. However, this approach is restricted to plates with stiffeners running in one direction only, (i.e., prismatically stiffened plates).

The discrete stiffener approach (e.g., see [20]-[22]) considers the discrete effects of stiffeners in the plate buckling behavior by modeling stiffeners as lines of bending (EI) and torsion (GJ) stiffnesses on panel skin. The stiffener's axial stiffness (EA) is included in the overall prebuckling stress state determination. Some

local cross-sectional deformations are lost when stiffeners are modeled as EI and GJ stiffeners. This approach becomes difficult for plates stiffened in more than two directions and also when the stiffener is not symmetric with respect to the mid-surface of the skin. Most of the work done using the discrete stiffener approach involved the Classical Laminated Plate Theory (CLPT) rather than the FSDT.

The buckling analysis of a curved panel with variable curvature appears to have drawn much less attention by researchers. In 1946, Marguerre [23] addressed this problem for isotropic panels. He expanded the curvature term, $(1/R)$, which is a function of the arc length along the panel in a Fourier series and then solved the buckling problem using trigonometric series as Ritz functions. The approach, however, becomes tedious if a large number of terms is required to represent the curvature of the panel accurately. For elliptical cylindrical shells where very few terms are required to represent the curvature of the shell, Marguerre's approach has been used successfully (see [24]).

1.3 SCOPE OF PRESENT STUDY

Finite element analysis has been used for the analysis of grid-stiffened panels (e.g., [7]). Such a method, even though sophisticated and accurate, poses problems in modeling such panels. There are a number of factors to be considered while creating the finite element model. The finite element model involves detailed discretization of each stiffened panel which is very tedious and time consuming and thereby limits the number and type of configurations that can be readily examined by the designer. The buckling load prediction is influenced by the type of elements used in modeling the structure, the form of prebuckling stress state, and the type of boundary conditions that are applied. Buckling loads obtained from finite element solutions involve solving a large eigenvalue problem and hence not well suited within a design optimization procedure.

The overall objective of this dissertation is to develop and validate an analytical tool for design and analysis of composite grid-stiffened circular cylindrical panels exhibiting global buckling. This analytical tool involves the development of an improved smeared stiffener theory for the global buckling analyses, and a Rayleigh-Ritz-type buckling analysis for panels with general parallelogram-shaped and general triangular planform to assess local skin buckling, and the integration of these analysis tools with a design optimization process for discrete design variable. The improved smeared stiffener theory is implemented through a mathematical study of the stress state in an isolated semi-infinite stiffened panel leading to the location of the neutral surface as a function of distance away from the stiffener in the semi-infinite stiffened panel. The effect of skin-stiffener interaction is then introduced in the smeared stiffener theory by computing the stiffness due to the stiffener with respect to a shift in the neutral surface. As grid-stiffened cylindrical shells have closely spaced stiffeners, smeared stiffener approach with a first-order, shear-deformation theory can be used for an elastic buckling analysis under combined loading. FSDT is preferred over CLPT because it has been shown that buckling loads of composite stiffened plates are overestimated by 8 to 20 percent when transverse shear effects are neglected (e.g., [17]). The Rayleigh-Ritz-type buckling analysis for general parallelogram-shaped and general triangular-shaped planform with various boundary conditions is achieved through the use of a "circulation" function and accounts for material anisotropy and combined in-plane membrane loadings. The crippling of a stiffener segment is examined using the procedure given in Ref. [9]. The global and local buckling analyses are performed repeatedly in a design cycle until optimum or near-optimum design is obtained.

1.4 ORGANIZATION

The remainder of this dissertation is organized as follows. Chapter 2 presents the formulation of the improved smeared stiffener theory. Results for grid-stiffened

panels obtained from the improved smeared theory are compared with those from the traditional smeared theory and also with those obtained from detailed finite element analyses. Chapter 3 deals with the buckling analysis using the Rayleigh-Ritz method and a "circulation" function. The method is implemented using different shell theories and addresses general parallelogram-shaped and general triangular-shaped plate planforms. Buckling loads for cylindrical panels are presented and compared with those obtained using finite element analyses. Buckling loads for skewed and triangular plates are presented and compared with those from obtained using finite element analyses and with existing solutions when available. Chapter 4 presents the design strategy for optimal design of grid-stiffened panels for global buckling. The design strategy utilizes the Genetic Algorithm ([25]) and results are presented for panels with different in-plane loading conditions. Finally, conclusions from this study and suggested future directions are listed in Chapter 5.

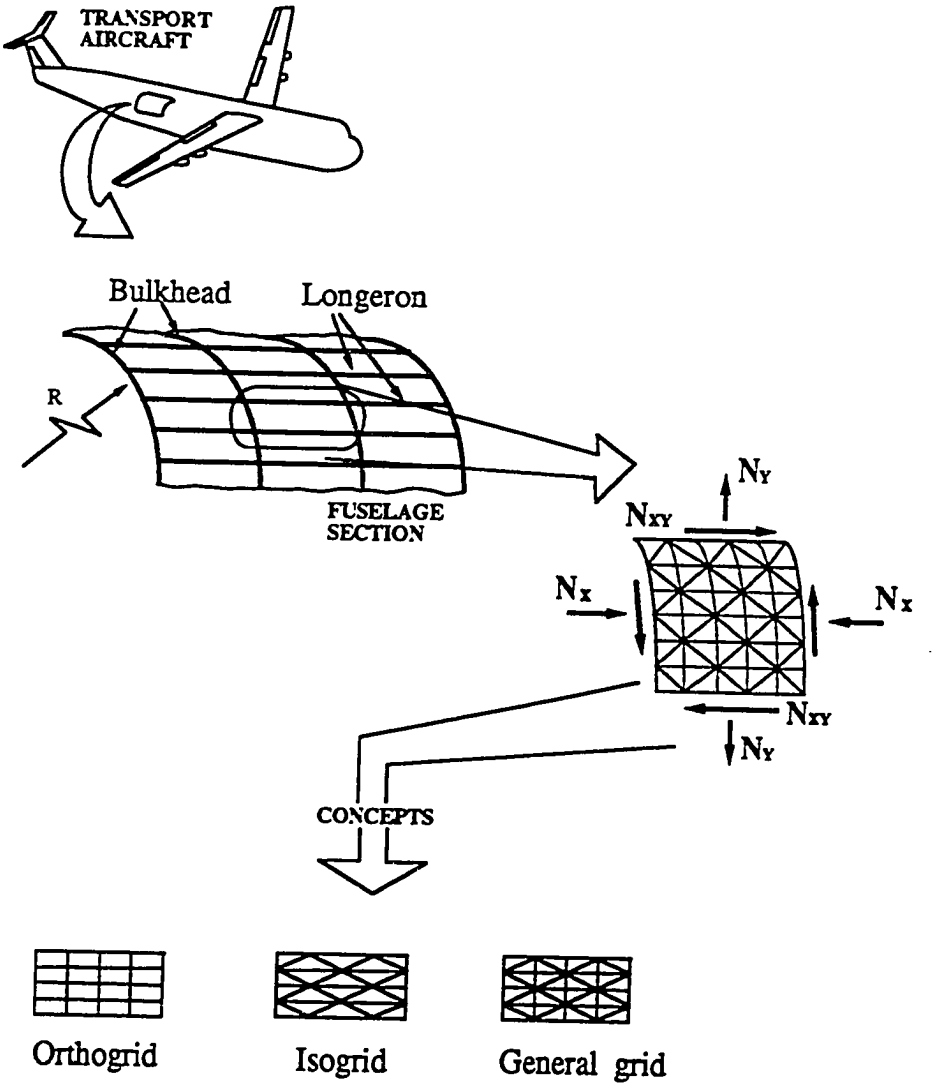

Figure 1.1 Aircraft structural applications.

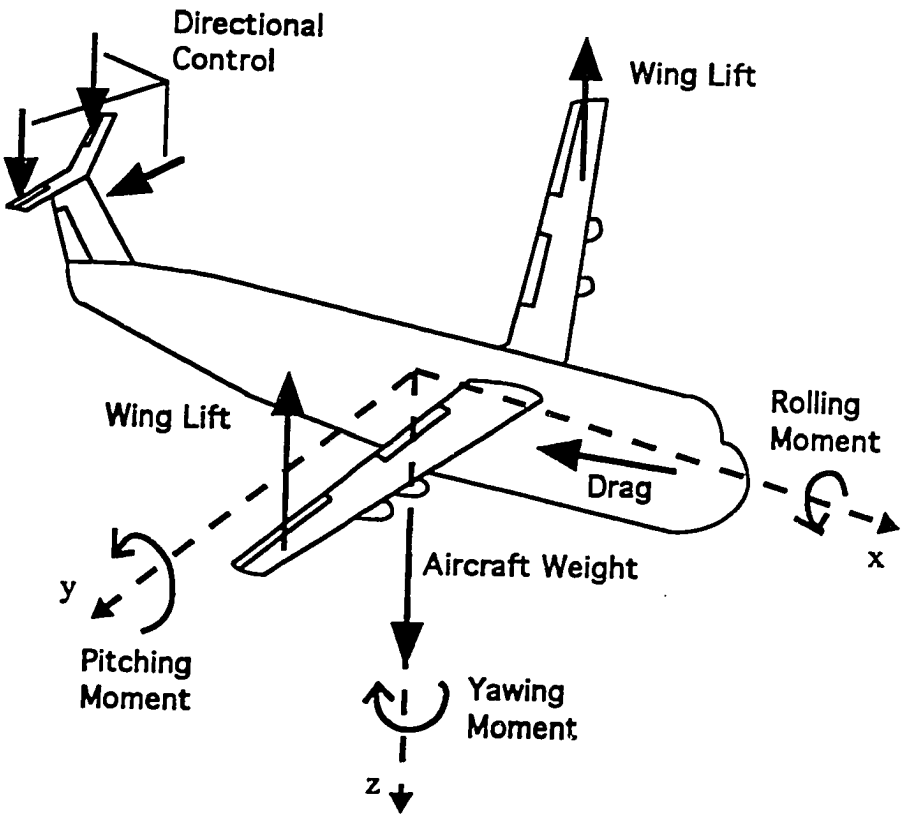

Figure 1.2 Typical resultants forces due to air loads on airplane.

Chapter 2

IMPROVED SMEARED STIFFENER THEORY

An improved smeared stiffener theory for stiffened panels is presented that includes skin-stiffener interaction effects. The neutral surface profile of the skin-stiffener combination is developed analytically using the minimum potential energy principle and statics conditions. The skin-stiffener interaction is accounted for by computing the bending and coupling stiffness due to the stiffener and the skin in the skin-stiffener region about a shifted in the neutral axis at the stiffener. Buckling load results for axially stiffened, orthogrid, and general grid-stiffened panels are obtained using the smeared stiffness combined with a Rayleigh-Ritz method and are compared with results from detailed finite element analyses.

2.1 ANALYTICAL APPROACH

If a stiffened plate is bent while it is supported on all four edges, the neutral surface in the neighborhood of the stiffener will lie between the mid-plane of the plate and the mid-plane of the stiffener. It is convenient to think of this as a shift of the neutral surface from the mid-plane of the stiffener. Hence, the approximate stiffness added by a stiffener to the skin stiffness will then be due to the plate-stiffener combination being bent about its neutral surface rather than due to the stiffener being bent about its own neutral surface or the plate neutral surface. The location of the neutral surface

is determined theoretically through a study of the local stress distribution near the skin-stiffener interface similar to the approach presented in Ref. [26] for a panel with a blade stiffener. However, the study presented in Ref. [26] does not provide a general solution that is applicable to all classes of symmetric laminates.

A grid-stiffened panel may be considered to be an assembly of repetitive units or unit cells (see Figure 2.1). Any stiffener segment in the unit cell may be isolated in a semi-infinite skin-stiffener model as shown in Figure 2.1 for a diagonal stiffener. An approach for obtaining the stress distribution in a semi-infinite stiffened panel is given below.

The average membrane stresses in the local coordinate system of the semi-infinite stiffened panel model for the plate are obtained by combining the constitutive relations with the strain compatibility equations and the use of a stress function approach. The stress function is

$$P_x = \partial^2 F/\partial y^2,\ P_y = \partial^2 F/\partial x^2,\ P_{xy} = -\partial^2 F/\partial x \partial y \tag{2.1}$$

where F is defined as the stress function and P_x, P_y, and P_{xy} are the average axial, transverse, and in-plane shear membrane stresses and are given by;

$$\begin{Bmatrix} \epsilon_x^0 \\ \epsilon_y^0 \\ \gamma_{xy}^0 \end{Bmatrix} = \begin{bmatrix} A_{11}/t & A_{12}/t & A_{16}/t \\ A_{12}/t & A_{22}/t & A_{26}/t \\ A_{16}/t & A_{26}/t & A_{66}/t \end{bmatrix}^{-1} \begin{Bmatrix} P_x \\ P_y \\ P_{xy} \end{Bmatrix} \tag{2.2}$$

where ϵ_x^0, ϵ_y^0 and γ_{xy}^0 are the membrane strains, A_{ij} is the extensional stiffness coefficients obtained from the classical lamination theory ([27]), and t is the skin thickness. The stress function F satisfies the conditions for equilibrium of a rectangular plate element. The compatibility equation is

$$\partial^2 \epsilon_x^0/\partial y^2 + \partial^2 \epsilon_y^0/\partial x^2 = \partial^2 \gamma_{xy}^0/\partial x \partial y \tag{2.3}$$

Using Equation (2.1) and substituting for the strains from Equation (2.2) in Equation (2.3), a fourth-order partial differential equation is obtained

$$A_{11}^* \frac{\partial^4 F}{\partial x^4} - 2A_{26}^* \frac{\partial^4 F}{\partial x^3 \partial y} + (2A_{12}^* + A_{66}^*) \frac{\partial^4 F}{\partial x^2 \partial y^2} - 2A_{16}^* \frac{\partial^4 F}{\partial x \partial y^3} + A_{22}^* \frac{\partial^4 F}{\partial y^4} = 0 \tag{2.4}$$

where A^*_{ij} is given by $[A_{ij}/t]^{-1}$. Dividing Equation (2.4) by A^*_{11} and transforming the y coordinate by $\eta = e_0 y$ results in

$$\frac{\partial^4 F}{\partial x^4} - 2e_0\frac{A^*_{26}}{A^*_{11}}\frac{\partial^4 F}{\partial x^3 \partial \eta} + e_0^2\frac{(2A^*_{12} + A^*_{66})}{A^*_{11}}\frac{\partial^4 F}{\partial x^2 \partial \eta^2} - 2e_0^3\frac{A^*_{16}}{A^*_{11}}\frac{\partial^4 F}{\partial x \partial \eta^3} + \frac{\partial^4 F}{\partial \eta^4} = 0 \quad (2.5)$$

where $e_0 = [A^*_{11}/A^*_{22}]^{1/4}$. This equation is solved by assuming that stresses decay rapidly as the distance, y, away from the stiffener centerline becomes large, that the stresses are localized near the stiffener, and that a symmetric loading condition exists along the stiffener. The membrane stress function is assumed to be of the form

$$F = Real(e^{imk(x+ire_0 y)}) = Real(e^{imk(x+ir\eta)}) \quad (2.6)$$

where $k = \frac{\pi}{L}$, $m = 1, 2, 3, ...$, r is an unknown, and x and y are local coordinates in the semi-infinite model. Substituting this stress function into the fourth-order differential equation (Equation (2.5)) results in a quartic equation in terms of the unknown r. The roots of the quartic equation are computed using subroutine CXPOLY from the Mathematical and Statistical Software (Ref. [28]) at NASA Langley Research Center. The roots of the quartic equation occur as two pairs of complex numbers given by

$$r = \begin{cases} \pm r_{R1} + ir_{I1} \\ \pm r_{R2} + ir_{I2} \end{cases} \quad (2.7)$$

The membrane solution corresponds to the root with the largest magnitude of the real part for r and is developed as follows

$$F_{1m} = Real[e^{imk[x+i(r_R+ir_I)\eta]}] = e^{-r_R mk\eta}cos[mk(x - r_I\eta)], \quad for \ \eta > 0$$

$$F_{2m} = Real[e^{imk[x+i(-r_R+ir_I)\eta]}] = e^{-r_R mk\eta}cos[mk(x + r_I\eta)], \quad for \ \eta < 0$$

$$F_m = \frac{A_m}{2}(F_{1m} + F_{2m})$$

$$= A_m e^{-mke_0 r_R(y - t_s/2)}cos[mkx]cos[mke_0 r_I(y - t_s/2)] \quad (2.8)$$

where r_R and r_I are the real and imaginary parts of the root, respectively, t_s is the thickness of the stiffener, and A_m are the unknown coefficients to be determined.

A similar approach is taken for the bending solution using the fourth-order partial differential equation for the out-of-plane deflection in terms of the local co-ordinate system, which requires that the resulting moments acting on a rectangular element vanish. That is,

$$\frac{\partial^4 w}{\partial x^4} + 4e_b \frac{D_{16}}{D_{11}} \frac{\partial^4 w}{\partial x^3 \partial \eta} + 2e_b^2 \frac{(2D_{12} + D_{66})}{D_{11}} \frac{\partial^4 w}{\partial x^2 \partial \eta^2} + 4e_b^3 \frac{D_{26}}{D_{11}} \frac{\partial^4 w}{\partial x \partial \eta^3} + \frac{\partial^4 w}{\partial \eta^4} = 0 \quad (2.9)$$

where D_{ij} are the bending stiffness coefficients of the skin, $e_b = [D_{11}/D_{22}]^{1/4}$ and $\eta = e_b y$. The solution for the out-of-plane deflection is obtained by assuming that the out-of-plane deflection decays as y becomes large and that the loading is symmetric along the stiffener. The out-of-plane deflection is assumed to be of the form

$$w = Real(e^{imk(x+ire_b y)}) \quad (2.10)$$

which on substitution into Equation (2.9) gives another quartic equation in r. The solution for the out-of-plane displacement corresponds to the root with the smallest non-zero magnitude of real part for part for r and is developed as follows

$$\begin{aligned}
w_{1m} &= e^{imk[x+i(r_{Rb}+ir_{Ib})\eta]} \text{ for } \eta > 0 \\
w_{2m} &= e^{imk[x+i(-r_{Rb}+ir_{Ib})\eta]} \text{ for } \eta < 0 \\
w_m &= \tfrac{1}{2} Real[iB_m w_{1m} + C_m w_{1m} - iB_m w_{2m} + C_m w_{2m}] \\
w_m &= e^{-mke_b r_{Rb}(y-t_s/2)} \{ B_m \, sin[mke_b r_{Ib}(y - t_s/2)] \\
&\quad + C_m \, cos[mke_b r_{Ib}(y - t_s/2)] \} \, cos[mkx]
\end{aligned} \quad (2.11)$$

where r_{Rb} and r_{Ib} are the real and imaginary parts of the root, respectively, and B_m and C_m are the unknown coefficients to be determined.

Expressions for the membrane strains and the curvatures can now be obtained using Equation (2.8) and (2.11). The membrane strains are obtained by also using Equation (2.2):

$$
\begin{aligned}
\epsilon_x^0 &= A_m\, k^2\, m^2 e^{-mke_0 r_R(y-t_s/2)} \times \\
&\{\, [\, (A_{11}^{*}(r_R^2 - r_I^2)e_0^2 - A_{12}^{*})cos(mkx) \;-\; e_0 r_R A_{16}^{*} sin(mkx)\,] \\
&\times cos(mke_0 r_I(y - t_s/2)) \\
&+ [\, 2e_0^2 A_{11}^{*} r_I r_R cos(mkx) \;-\; e_0 r_I A_{16}^{*} sin(mkx)\,] \\
&\times sin(mke_0 r_I(y - t_s/2))\, \} \\
\epsilon_y^0 &= A_m\, k^2\, m^2 e^{-mke_0 r_R(y-t_s/2)} \times \\
&\{\, [\, (A_{12}^{*}(r_R^2 - r_I^2)e_0^2 - A_{22}^{*})cos(mkx) \;-\; e_0 r_R A_{26}^{*} sin(mkx)\,] \\
&\times cos(mke_0 r_I(y - t_s/2)) \\
&+ [\, 2e_0^2 A_{12}^{*} r_I r_R cos(mkx) \;-\; e_0 r_I A_{26}^{*} sin(mkx)\,] \\
&\times sin(mke_0 r_I(y - t_s/2))\, \} \\
\gamma_{xy}^0 &= A_m\, k^2\, m^2 e^{-mke_0 r_R(y-t_s/2)} \times \\
&\{\, [\, (A_{16}^{*}(r_R^2 - r_I^2)e_0^2 - A_{26}^{*})cos(mkx) \;-\; e_0 r_R A_{66}^{*} sin(mkx)\,] \\
&\times cos(mke_0 r_I(y - t_s/2)) \\
&+ [\, 2e_0^2 A_{16}^{*} r_I r_R cos(mkx) \;-\; e_0 r_I A_{66}^{*} sin(mkx)\,] \\
&\times sin(mke_0 r_I(y - t_s/2))\, \} \\
-\frac{\partial^2 w}{\partial x^2} &= k^2\, m^2 e^{-mke_1 r_{Rb}(y-t_s/2)} cos(mkx) \\
&[\, C_m cos(mke_1 r_{Ib}(y - t_s/2)) \;+\; B_m sin(mke_1 r_{Ib}(y - t_s/2))\,] \\
-\frac{\partial^2 w}{\partial y^2} &= -k^2\, m^2 e_1^2\, e^{-mke_1 r_{Rb}(y-t_s/2)} cos(mkx) \\
&\{\, [\, (r_{Rb}^2 - r_{Ib}^2)C_m - 2r_{Rb} r_{Ib} B_m\,] cos(mke_1 r_{Ib}(y - t_s)) \\
&+ [\, (r_{Rb}^2 - r_{Ib}^2)B_m + 2r_{Rb} r_{Ib} C_m\,] sin(mke_1 r_{Ib}(y - t_s))\, \} \\
-2\frac{\partial^2 w}{\partial x y} &= -4k^2\, m^2 e_1\, e^{-mke_1 r_{Rb}(y-t_s/2)} sin(mkx) \\
&\{\, [\, r_{Rb} C_m - r_{Rb} B_m\,] cos(mke_1 r_{Ib}(y - t_s)) \\
&+ [\, r_{Ib} C_m + r_{Rb} B_m\,] sin(mke_1 r_{Ib}(y - t_s))\, \}
\end{aligned}
\tag{2.12}
$$

These two solutions (Equations (2.8) and (2.11)) are valid near the skin-stiffener interface but not within the stiffener itself (i.e., $y \geq t_s/2$). It is assumed that, since the stiffener is thin, the strain within the stiffener is approximately equal to the strain at the edge of the stiffener (at $y = t_s/2$). The total strain energy, U_T, of the skin-stiffener combination is developed next from expressions for the out-of-plane deflection, w_m, and the membrane stress function, F_m. The total strain energy is obtained by evaluating the following integrals:

1. The strain energy of the skin is

$$U_{skin} = \int_{t_s/2}^{\infty} \int_{-L}^{L} \left(\{\epsilon_0\}^T [A_{ij}] \{\epsilon_0\} + \{\kappa\}^T [D_{ij}] \{\kappa\} \right) dx dy \qquad (2.13)$$

   where $\{\epsilon_0\} = \{\epsilon_x^0 \ \epsilon_y^0 \ \gamma_x^0\}$ are the membrane strains and $\{\kappa\} = \{\kappa_x \ \kappa_y \ \kappa_{xy}\}$ are the curvatures.

2. The strain energy of the stiffener is

$$U_{stiff} = \frac{1}{2} t_s \int_{-(t/2+h)}^{-t/2} \int_{-L}^{L} Q_{11} \left(\epsilon_x^0 + z\kappa_x \right)_{y=t_s/2}^2 dx dz \qquad (2.14)$$

   where Q_{11} is the longitudinal modulus of the stiffener and t is the total thickness of the skin.

3. The strain energy of the skin attached to the stiffener is

$$U_{attach} = \frac{t_s}{2} \int_{-L}^{L} \left(A_{11} (\epsilon_x^0)_{y=t_s/2}^2 + D_{11} (\kappa_x)_{y=t_s/2}^2 \right) dx \qquad (2.15)$$

Hence, the expression for the total strain energy, U_T, is obtained by summing these contributions to obtain

$$U_T = C_A A_m^2 + C_B B_m^2 + C_C C_m^2 + C_{AC} A_m C_m + C_{CB} C_m B_m \qquad (2.16)$$

where the coefficients C_A, C_B, C_C, C_{AC} and C_{CB} are obtained by evaluating the strain energy integrals and A_m, B_m, and C_m are the unknown coefficients of the assumed functions F_m in Equation (2.8) and w_m in Equation (2.11).

The total bending moment transmitted at any cross-section perpendicular to the longitudinal axis of the stiffener due to the eccentricity of the stiffener for the symmetric case can be represented by the series

$$M = \sum_{m=1}^{\infty} M_m \, cos(mkx) \tag{2.17}$$

From statics, the normal stresses over the cross-section of plate-stiffener combination must satisfy the following conditions

$$\int_A \sigma_x dA =$$
$$2\int_{-t/2}^{t/2}\int_{t_s/2}^{\infty} \sigma_x dz dy + t_s \int_{-(t/2+h)}^{t/2} Q_{11}(\epsilon_x^0 + z\kappa_x)_{y=t_s/2} \, dz = 0 \tag{2.18}$$

$$\int_A z\sigma_x dA =$$
$$2\int_{-t/2}^{t/2}\int_{t_s/2}^{\infty} z\sigma_x dz dy + t_s \int_{-(t/2+h)}^{t/2} zQ_{11}(\epsilon_x^0 + z\kappa_x)_{y=t_s/2} \, dz$$
$$= \sum_{m=1}^{\infty} M_m \, cos(mkx) \tag{2.19}$$

where t is the total thickness of the skin, t_s is the total thickness of the stiffener, h is the height of the stiffener above the outer surface of the skin, and σ_x is the normal stress distribution over the cross-section. Evaluating the integrals defined by Equations (2.18) and (2.19) results in the following relations after neglecting coefficients of $sin(mkx)$ which are due to the A_{16} and D_{16} terms in the extensional and bending stiffness matrices, respectively, and also due to A_{16}^* in the expression for ϵ_x^0 in Equation (2.12):

$$S_{11}A_m + S_{13}C_m = 0$$
$$S_{21}A_m + S_{22}B_m + S_{23}C_m = M_m \tag{2.20}$$

where S_{ij} coefficients are determined by collecting like coefficients multiplying the unknowns A_m, B_m and C_m in Equations (2.18) and (2.19). Using Equations (2.20), the following expressions for B_m and C_m are obtained in terms of A_m and M_m

$$\begin{aligned} C_m &= S^*_{11} A_m \\ B_m &= S^*_{21} A_m + S^*_{22} M_m \end{aligned} \tag{2.21}$$

where

$$S^*_{11} = -S_{11}/S_{13}, \quad S^*_{21} = (S_{11}S_{23} - S_{21}S_{13}) \; / \; S_{13}S_{22}$$
$$\text{and} \quad S^*_{22} = 1/S_{22} \tag{2.22}$$

Equations (2.21) are substituted into Equation (2.16) and the total energy is minimized with respect to A_m to yield

$$A_m = -V_M M_m / V_A \tag{2.23}$$

where

$$\begin{aligned} V_A &= 2(C_A + C_B(S^*_{21})^2 + C_C(S^*_{11})^2 C_{CB} S^*_{11} S^*_{21} \\ \text{and } V_M &= 2C_B S^*_{21} S^*_{22} + C_{CB} S^*_{11} S^*_{22} \end{aligned} \tag{2.24}$$

Using Equation (2.23), B_m and C_m can be expressed in terms of M_m, V_M and V_A, with M_m as the only unknown. That is,

$$\begin{aligned} C_m = S^*_{11} A_m &= -S^*_{11} \frac{V_M M_m}{V_A} \\ B_m = S^*_{21} A_m + S^*_{22} M_m &= -S^*_{21} \frac{V_M M_m}{V_A} + S^*_{22} M_m \end{aligned} \tag{2.25}$$

The expression for axial strain in the skin-stiffener combination is obtained from Equation (2.12) as

$$\epsilon_x = \epsilon^0_x - z \frac{\partial^2 w}{\partial x^2} \tag{2.26}$$

Substituting for A_m, B_m and C_m in Equation (2.26) from Equations (2.23) and (2.25) and solving for the value of z for which ϵ_x is zero, an expression for the neutral surface,

$Z'(y)$, is obtained. Only one term ($m = 1$) in the series expansion is used to obtain the expression for $Z'(y)$

$$Z'(y) = \epsilon_x^0 \ / \ \frac{\partial^2 w}{\partial x^2} \tag{2.27}$$

where

$$\begin{aligned}
\epsilon_x^0 &= -\frac{V_m M_m}{V_A} k^2 m^2 e^{-mke_0 r_R(y-t_s/2)} \times \\
&\{ (A_{11}^*(r_R^2 - r_I^2)e_0^2 - A_{12}^*)cos(mkx) \times cos(mke_0 r_I(y - t_s/2)) \\
&+ 2e_0^2 A_{11}^* r_I r_R cos(mkx) \times sin(mke_0 r_I(y - t_s/2)) \} \\
\frac{\partial^2 w}{\partial x^2} &= -k^2 m^2 Exp[-mke_b r_{Rb}(y - t_s/2)] \, cos[mkx] \times \\
&\{ (-S_{11}^* \frac{V_M M_m}{V_A}) \, cos[mke_b r_{Ib}(y - t_s/2)] \\
&+ (-S_{21}^* \frac{V_M M_m}{V_A} + S_{22}^* M_m) sin[mke_b r_{Ib}(y - t_s/2)]\}
\end{aligned} \tag{2.28}$$

The coefficients of $sin(mkx)$ in the expression for ϵ_x^0 are neglected. These coefficients are due to A_{16}^* and hence, the expression for $Z'(y)$ is independent of M_m and the axial distance x. Since the expression for Z' involves $exp[mk(e_b r_{Rb} - e_0 r_R)(y - t_2/2)]$, the choice of roots for the solution of the stress function, F, and the out-of-plane deflection, w, ensures that the neutral surface $Z'(y)$ decays as the distance away from the centerline, y, becomes large. Finally, the shift in the neutral surface at the stiffener is obtained by setting $y = t_s/2$ in the expression for $Z'(y)$.

$$Z_n = -\frac{(A_{11}^* e_0^2(r_R^2 - r_I^2) \ - \ A_{12}^*)}{S_{11}^*} \tag{2.29}$$

A typical profile of the neutral surface for a skin-stiffener combination is shown in Figure 2.2. The distance y^* represents the distance from the centerline of the stiffener to the point where the neutral surface coincides with the mid-surface of the skin. The average of the neutral profile over the distance y^* is Z^*. The quantities y^* and Z^* are obtained numerically.

The smeared stiffnesses of a stiffened panel is obtained by mathematically converting the stiffened panel to an unstiffened panel (Ref. [17]. The smeared

stiffnesses are developed on the basis that the strain energy of the stiffened panel should be the same as that of the equivalent unstiffened panel. These smeared stiffnesses can then be used in a Rayleigh-Ritz type analysis to solve for buckling loads of the stiffened panel. In Reference [17], the strain energy of the skin and stiffeners in the unit cell is obtained by using stiffnesses of the skin and the stiffeners which are computed about the mid-surface of the skin. Since, there is a shift in the neutral surface at the stiffener, the stiffness of the stiffeners and the skin segment directly above it has to be computed about a shift in the neutral surface so as to account for the skin-stiffener interactions.

The correction to the smeared stiffnesses due to the skin-stiffener interaction is herein introduced by computing the stiffness of the stiffener and the skin segment directly contiguous to it according to the following criteria.

1. If $y^* < t/4$, then the reference surface for the stiffener is Z_n.

2. If $y^* > t/4$, then the reference surface for the stiffener is Z^*.

In either case, the reference surface of the skin is taken to be its mid-surface. Other more elaborate and accurate schemes can be used to introduce the skin-stiffener interaction using the neutral surface profile. However, the one described herein is simple, and provides sufficiently accurate buckling loads for the preliminary structural design.

2.2 NUMERICAL RESULTS

Three stiffened panels with different stiffener configurations and simply-supported boundary conditions are used as examples to demonstrate the present analytical approach. Panel 1 is an axially-stiffened panel, Panel 2 is an orthogrid-stiffened panel, and Panel 3 is an example for a general grid-stiffened panel. Detailed finite element analyses of these three panels have been conducted to verify the results of the present analytical approach. The finite element analysis codes STAGS ([29]) and DIAL ([30])

have been used for this purpose. In the STAGS finite element model, a nine-node shear-flexible element (i.e., STAGS element 480) is used while an eight-node isoparametric shear-flexible element is used in the DIAL model. Finite element analysis results for all panels indicate that the panels buckle globally under the applied in-plane loading conditions.

Panel 1

Panel 1 is 30.0-in. long and 30.0-in. wide with axial stiffeners only. The stiffener height and thickness are 1.86958 in. and 0.20084 in., respectively. The unit cell is 30.0-in. long and 10.0-in. wide (see Figure 2.3). The skin ply stacking sequence is $[\pm 45/\mp 45/0/90]_s$ with thicknesses of 0.00637 in. for the $45°$ and $-45°$ plies, 0.0249 in. for the $0°$ plies and 0.0416 in. for the $90°$ plies. The stiffener ply stacking sequence is $[\pm 45/\mp 45/0]_s$ with thicknesses of 0.00823 in. for the $45°$ and $-45°$ plies and 0.0675 in. for the $0°$ plies. The nominal ply mechanical properties used are: longitudinal modulus = 19.0 Msi; transverse modulus = 1.89 Msi; shear modulus = 0.93 Msi and major Poisson's ratio = 0.38.

The four panel load cases considered are shown in Table 2.1 The STAGS analysis results are compared with solutions from the smeared stiffener approach without skin-stiffener interaction effects included (the traditional approach) and with skin-stiffener interaction effects included (the present approach). It can be seen that the value of Z_n for the axial stiffener is not small compared to the height of the stiffener. The result obtained from the traditional approach is in good agreement with the STAGS analysis result for the case of axial compression and the result from present approach is less than the STAGS analysis result by 7.5 percent. For the other load cases shown in the Table 2.1, the results obtained by the traditional approach are greater than those of STAGS by 8 to 13 percent and those of the present approach are in good agreement with the STAGS results.

Panel 2

Panel 2 is 60.0-in. long and 36.0-in. wide with axial and transverse stiffeners only. The stiffener height and thickness are 0.5 in. and 0.12 in., respectively. The unit cell is 20.0-in. long and 9.0-in. wide (see Figure 2.4). The skin ply stacking sequence is $[\pm 45/90/0]_s$ and each ply thickness is 0.008 in. The stiffener is made of graphite epoxy material with 0° orientation. The nominal ply mechanical properties used are: longitudinal modulus = 24.5 Msi; transverse modulus = 1.64 Msi; shear modulus = 0.87 Msi and major Poisson's ratio = 0.3.

The panel buckling response when subjected to four loading conditions is indicated in Table 2.2. The DIAL analysis results are compared in Table 2.2 with solutions from the smeared stiffener approach with and without skin-stiffener interaction effects included. The value of Z_n for the transverse stiffener is not small compared to the height of the stiffener. The results obtained using the traditional approach overestimate the DIAL analysis result by 12.6 percent for the axial compression load case, by 4.0 percent for the transverse compression load case, and by 8.4 percent for the combined load cases. Results from the present approach agree with the DIAL analysis results except for the transverse compression load case where the present result is 5.2 percent less than the DIAL analysis result.

Panel 3

Panel 3 is 56.0-in. long and 20.0-in. wide with transverse and diagonal stiffeners only. The stiffener height and thickness are 0.276 in. and 0.1125 in., respectively. The unit cell dimensions for this panel are 7.0 in. in length and 5.0 in. in width (see Figure 2.5). The skin stacking sequence is $[45/90/-45]_s$, and each ply thickness is 0.008 in. The stiffener for this case is also made of 0° material. The nominal ply mechanical properties used are: longitudinal modulus = 24.5 Msi; transverse modulus = 1.64 Msi; shear modulus = 0.87 Msi and major Poisson's ratio = 0.3.

The panel is analyzed for the three load conditions shown in Table 2.3. The DIAL analysis results are compared with results from the smeared stiffener approach with and without skin-stiffener interaction effects in Table 2.3. For this panel, the values of Z_n are small compared to the height of the stiffener. The results obtained from the traditional approach are approximately 11 percent greater than the DIAL analysis results, and the results obtained using the present approach are approximately 6.5 percent less than the DIAL analysis results. For this panel, the results obtained using the present approach are conservative since the contribution due to stiffness terms A_{16} and D_{16}, and the flexibility term A_{16}^* to P_x (Equation 2.2) and ϵ_x^0 (Equation 2.12) are not small and does influence the neutral surface profile position for the diagonal stiffener.

2.3 SUMMARY

An improved smeared stiffener theory that includes skin-stiffener interaction effects has been developed. The skin-stiffener interaction effects are introduced by computing the stiffness of the stiffener and the skin at the stiffener region about the neutral axis at the stiffener. The neutral surface profile for the skin-stiffener combination is obtained analytically through a study of the local stress distribution near the skin-stiffener interface.

The results from the numerical examples considered suggest that skin-stiffener interaction effects should be included in the smeared stiffener theory to obtain good correlation with results from detailed finite element analyses. In a few cases, the present analysis appears to underestimate the buckling load by 5 to 7 percent. In spite of this limitation, the smeared stiffener theory with skin-stiffener interaction effects included is still a useful preliminary design tool and results in buckling loads that are more accurate than the results from the traditional smeared stiffener approach.

Table 2.1 Results for axially stiffened panel (Panel 1).

X-stiffener: Z_n = -0.4386 in., Z^* = -0.1020 in., y^* = 4.7512 in.

		Critical Eigenvalue		
N_x lbs/in.	N_{xy} lbs/in.	STAGS	Traditional Approach	Present Approach
1000	0	9.9636	9.9659	9.2135
0	1000	6.3016	6.7985	6.3483
1000	1000	4.9512	5.6018	4.9491
500	1000	5.5023	6.2007	5.5838

Table 2.2 Results for orthogrid panel (Panel 2).

X-stiffener: Z_n = -0.0949 in., Z^* = -0.0165 in., y^* = 0.0280 in.
Y-stiffener: Z_n = -0.1295 in., Z^* = -0.0177 in., y^* = 0.0131 in.

			Critical Eigenvalue		
N_x lbs/in.	N_y lbs/in.	N_{xy} lbs/in.	DIAL	Traditional Approach	Present Approach
400	0	0	0.7909	0.8903	0.8161
0	200	0	0.6281	0.6536	0.5956
400	200	0	0.3504	0.3799	0.3463
400	200	50	0.3500	0.3796	0.3458

Table 2.3 Results for grid-stiffened panel (Panel 3).

Y-stiffener: Z_n = -0.0135 in., Z^* = -0.0043 in., y^* = 2.3636 in.
D-stiffener: Z_n = -0.0698, Z^* = -0.0349 in., y^* = 0.0239 in.

			Critical Eigenvalue		
N_x lbs/in.	N_y lbs/in.	N_{xy} lbs/in.	DIAL	Traditional Approach	Present Approach
0.0	400	0.0	0.3290	0.3646	0.3045
0.0	400	300	0.3224	0.3595	0.3008
100	400	300	0.3121	0.3486	0.2917

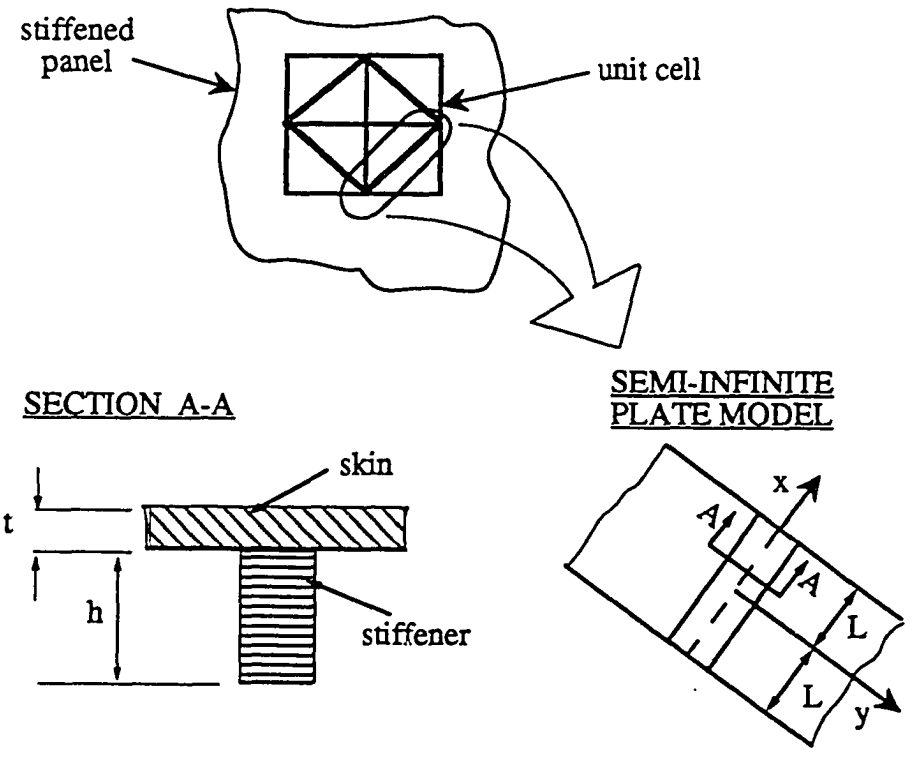

Figure 2.1 Semi-infinite plate model for skin-stiffener element.

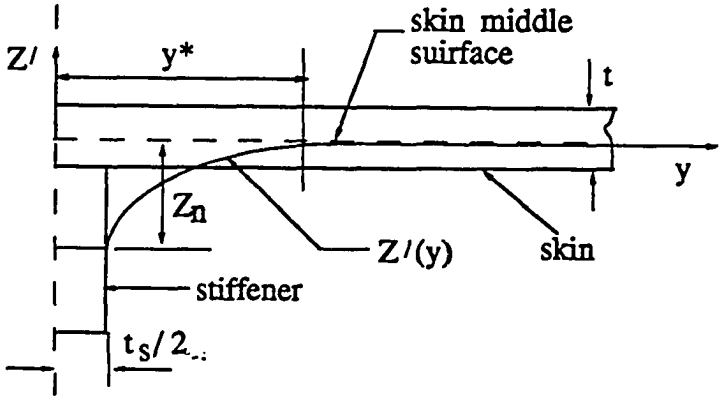

Figure 2.2 Typical profile for neutral surface for skin-stiffener element.

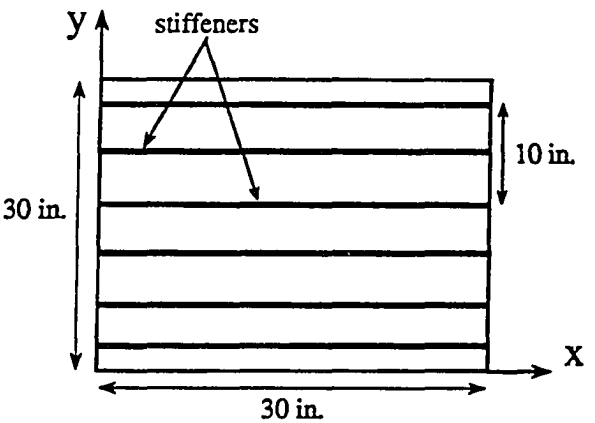

Figure 2.3 Simply supported axially stiffened panel

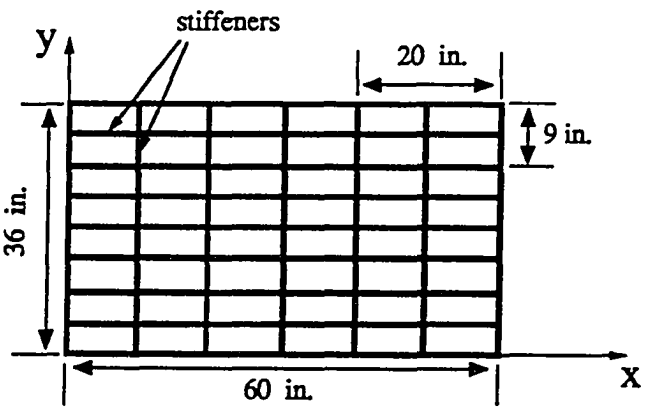

Figure 2.4 Simply supported orthogrid-stiffened panel.

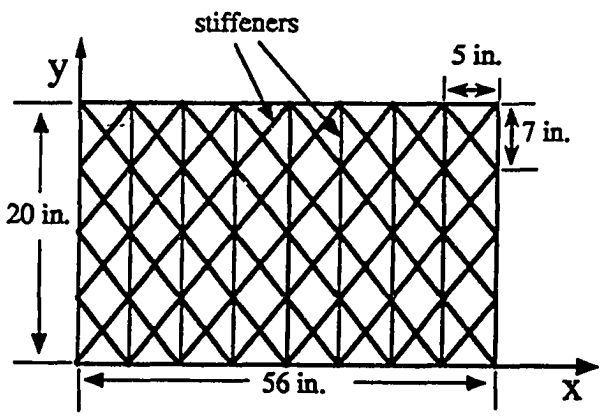

Figure 2.5 Simply supported grid-stiffened panel.

Chapter 3

BUCKLING ANALYSIS OF CURVED PANELS

This chapter deals with the buckling analysis of curved panels and makes use of the principle of minimum potential energy and a Rayleigh-Ritz solution procedure based on high-order complete polynomial functions. These polynomials are expressed in terms of natural coordinates for a quadrilateral plate geometry and in terms of area coordinates for a triangular plate geometry. The approach makes use of finite element concepts for mapping an arbitrary quadrilateral plate geometry to a square plate geometry and mapping a general triangular plate geometry to an equilateral triangular plate geometry. The Ritz functions include "circulation" functions that can be used to impose different boundary conditions. The mapping is important so as to facilitate computations of linear and geometric stiffness matrices and imposition of boundary conditions. The formulation accounts for transverse shear flexibility and for material anisotropy. Buckling loads are presented for flat skew parallelogram-shaped plates, triangular plates, and curved cylindrical panels. Results are compared with existing solutions and finite element solutions.

3.1 PREAMBLE

The stiffener pattern on a grid-stiffened panel is determined primarily by the combination of in-plane axial, transverse and shear loading experienced by the structure.

In the case of a diagonal-stiffener configuration, the skin segments have a rhombic geometry. Even for the case of a more conventional orthogonal stiffener pattern used for a swept-back wing, the skin segments have a skewed quadrilateral geometry. For a stiffener pattern with diagonal and axial stiffeners, the skin segments have a triangular geometry. The boundary conditions imposed on the structural skin segments are determined by the stiffness of the stiffeners. Therefore, the buckling analysis method for composite skin segments should be general enough to include different boundary conditions, general quadrilaterals and triangular geometries, and anisotropic material properties in order to assess accurately the local buckling response of the composite skin segments in composite grid-stiffened panels.

A review of the existing literature on the buckling of arbitrary quadrilateral plates indicates that some aspects have been addressed, mostly for skewed isotropic plates using classical laminated plate theory (CLPT). A thorough review of the literature for buckling of skewed plates with different boundary conditions using CLPT and the Rayleigh-Ritz method is presented in Ref. [31]. Results are compared with those published by different authors. None of the references cited in Ref. [31] or any other recent publications in the open literature (e.g., Ref. [32] and [33]), address the buckling of skewed or rhombic anisotropic plates with or without transverse-shear flexibility. Most authors focus only on the vibration response rather than buckling.

The problem of buckling and vibration of triangular plates has been addressed mostly for isotropic plates. Buckling solutions for simply supported equilateral triangular isotropic plates were presented in 1933 by Woinowsky-Krieger as cited in [11] and validated in 1957 by Taylor [34]. The structural stability of simply supported, right-angle isosceles triangular isotropic plates subjected to in-plane shear loading was presented in 1951 by Klitcheiff [35]. In 1953, Wittrick [36] improved Klitcheiff's solution to include combined in-plane normal loading and different boundary conditions. In 1956, Li-Chow [37] obtained the buckling solution for a

simply-supported $30° - 60° - 90°$ triangular isotropic plate subjected to compression. This solution was validated in 1963 by Reipert [38]. Finally, Valisetty and Reddy [39] presented solutions for simply supported isosceles triangular orthotropic plates in 1985. However, the solutions in Ref. [39] do not satisfy the zero-moment conditions at all points along the plate boundaries. The solutions in these references use classical laminated plate theory (CLPT). The vibration analysis of triangular plates has been studied to a larger extent than the buckling analysis. Vibration of triangular isotropic and/or orthotropic plates are addressed in references [32], [40]-[42], using CLPT and in Ref. [43] using a first-order, shear-deformation theory (FSDT). The only work dealing with triangular anisotropic plates is reported in Ref. [44] which deals with the free vibration of right-angle triangular plate using CLPT. No work has been reported on the buckling of anisotropic triangular plates with or without transverse shear flexibility.

The following sections describe the analysis methods developed for the buckling of general parallelogram-shaped and general triangular-shaped anisotropic panels using FSDT, and the results obtained using these methods are presented.

3.2 STRAIN-DISPLACEMENT RELATIONS

The displacement field for a cylindrical shell, according to a first-order, shear-deformation theory is given by

$$\begin{aligned} u(x,y,z) &= u_0(x,y) + z\phi_x(x,y) \\ v(x,y,z) &= v_0(x,y) + z\phi_y(x,y) \\ w(x,y,z) &= w_0(x,y) \end{aligned} \tag{3.1}$$

where u_0 is the membrane displacement in the x-direction, v_0 is the membrane displacement in the y-direction, w_0 is the out-of-plane transverse displacement in the z-direction, ϕ_x and ϕ_y are the cross-sectional rotations about the x and y axes, respectively.

According to FSDT, cross-sections normal to the reference plane before deformation are assumed to remain planar but not necessarily normal to the mid-surface after deformation. Figure 3.1 shows a cylindrical shell element with the coordinate axes, notations and sign convention given. The circumferential coordinate θ is replaced by $y = R\theta$, where R is the radius of the cylindrical shell segment. Noting that $\partial y = R\partial\theta$, the linear strain-displacement relations [45] can be written as;

$$\begin{aligned}
\epsilon_{xL} &= \epsilon_x^0 + z\kappa_x \\
\epsilon_{yL} &= \epsilon_y^0 + z\kappa_y \\
\gamma_{xyL} &= \gamma_{xy}^0 + z\kappa_{xy} \\
\gamma_{xzL} &= \gamma_{xz}^0 \\
\gamma_{yzL} &= \gamma_{yz}^0
\end{aligned}$$

where

$$\begin{aligned}
\epsilon_x^0 &= \frac{\partial u_0}{\partial x} \\
\epsilon_y^0 &= \frac{\partial v_0}{\partial y} + \frac{w_0}{R} \\
\gamma_{xy}^0 &= \frac{\partial u_0}{\partial y} + \frac{\partial v_0}{\partial x} \\
\kappa_x &= \frac{\partial \phi_x}{\partial x} \\
\kappa_y &= \frac{\partial \phi_y}{\partial y} \\
\kappa_{xy} &= \frac{\partial \phi_x}{\partial y} + \frac{\partial \phi_y}{\partial x} + \frac{C_2}{2R}\left(\frac{\partial v_0}{\partial x} - \frac{\partial u_0}{\partial y}\right) \\
\gamma_{xz}^0 &= \phi_x + \frac{\partial w_0}{\partial x} \\
\gamma_{yz}^0 &= \phi_y + \frac{\partial w_0}{\partial y} - C_1\frac{v_0}{R}
\end{aligned} \tag{3.2}$$

Here C_1 and C_2 are "tracer" coefficients used to implement different strain-displacement relations or shell theories. Accordingly when $C_1 = C_2 = 1$, the first approximation of Sanders-Koiter shell theory [46, 47] is obtained and when $C_1 = 1$, $C_2 = 0$, Love's shell theory [48] including transverse shear deformations is obtained. Finally, when $C_1 = 0$ and $C_2 = 0$, Donnell's shell theory [49] including transverse shear deformation is obtained. The linear strain-displacement relations with tracer coefficients can be written in matrix form as

$$\mathbf{E_p} = \begin{Bmatrix} \epsilon_x^0 \\ \epsilon_y^0 \\ \gamma_{xy}^0 \\ \kappa_x \\ \kappa_y \\ \kappa_{xy} \\ \gamma_{xz} \\ \gamma_{yz} \end{Bmatrix} = \begin{bmatrix} \frac{\partial}{\partial x} & 0 & 0 & 0 & 0 \\ 0 & \frac{\partial}{\partial y} & \frac{1}{R} & 0 & 0 \\ \frac{\partial}{\partial y} & \frac{\partial}{\partial x} & 0 & 0 & 0 \\ 0 & 0 & 0 & \frac{\partial}{\partial x} & 0 \\ 0 & 0 & 0 & 0 & \frac{\partial}{\partial y} \\ \frac{-C_2}{2R}\frac{\partial}{\partial y} & \frac{C_2}{2R}\frac{\partial}{\partial x} & 0 & \frac{\partial}{\partial y} & \frac{\partial}{\partial x} \\ 0 & 0 & \frac{\partial}{\partial x} & 1 & 0 \\ 0 & \frac{-C_1}{R} & \frac{\partial}{\partial y} & 0 & 1 \end{bmatrix} \begin{Bmatrix} u_0 \\ v_0 \\ w \\ \phi_x \\ \phi_y \end{Bmatrix} \tag{3.3}$$

The nonlinear strain-displacement relations for a circular cylindrical shell or panel as given by Ref. [50] are

$$\begin{aligned}
\epsilon_x &= u_{,x} + \frac{1}{2}(v_{,x}^2 + w_{,x}^2) \\
&= \epsilon_{xL} + \epsilon_{xNL} \\
\epsilon_y &= v_{,y} + \frac{w}{R} + \frac{1}{2}[u_{,y}^2 + (w_{,y} - \frac{v}{R})^2] \\
&= \epsilon_{yL} + \epsilon_{yNL} \\
\gamma_{xy} &= u_{,y} + v_{,x} + \frac{C_2}{2R}(v_{0,x} - u_{0,y}) - u_{,y}(v_{,y} + \frac{w}{R}) - v_{,x}u_{,x} + w_{,x}(w_{,y} - \frac{v}{R}) \\
&= \gamma_{xyL} + \gamma_{xyNL} \\
\gamma_{xz} &= w_{,x} + u_{,z} - w_{,x}u_{,x} - w_{,z}u_{,z} + v_{,x}v_{,z} \\
&= \gamma_{xzL} + \gamma_{xzNL} \\
\gamma_{yz} &= w_{,y} + v_{,z} - C_1\frac{v}{R} - (w_{,y} - \frac{v}{R})(v_{,y} + \frac{w}{R}) - v_{,z}w_{,z} + u_{,y}u_{,z} \\
&= \gamma_{yzL} + \gamma_{xyNL}
\end{aligned} \tag{3.4}$$

where a comma is used to indicate differentiation with respect to the next subscripted independent variable and the subscripts "L" and "NL" denote the linear part and the nonlinear part, respectively. For example $u_{,x}$ denotes $\frac{\partial u}{\partial x}$, ϵ_{xL} denotes the linear part of the axial strain ϵ_x, and ϵ_{xNL} denotes the nonlinear part of the axial strain ϵ_x. Substituting Equation (3.1) in (3.4), neglecting higher-order terms for the cross-sectional rotations since in the prebuckled state the cross-sectional rotations tend to zero, the nonlinear terms in the transverse shear strains, and the z/R terms, these nonlinear strains reduce to the following form:

$$\begin{aligned}
\epsilon_x &= u_{0,x} + z\phi_{x,x} + \frac{1}{2}(v_{0,x}^2 + w_{,x}^2) \\
&= \epsilon_{xL} + \epsilon_{xNL} \\
\epsilon_y &= v_{0,y} + \frac{w}{R} + z\phi_{y,y} + \frac{1}{2}[u_{0,y}^2 + (w_{,y} - \frac{v_0}{R})^2] \\
&= \epsilon_{yL} + \epsilon_{yNL} \\
\gamma_{xy} &= u_{0,y} + v_{0,x} + \frac{C_2}{2R}(v_{0,x} - u_{0,y}) + z(\phi_{x,y} + \phi_{y,x}) \\
&\quad -u_{0,y}(v_{0,y} + \frac{w}{R}) - v_{0,x}u_{0,x} + w_{,x}(w_{,y} - \frac{v_0}{R}) \\
&= \gamma_{xyL} + \gamma_{xyNL} \\
\gamma_{xz} &= w_{,x} + \phi_x \\
&= \gamma_{xzL} \\
\gamma_{yz} &= w_{,y} + \phi_y - C_1\frac{v_0}{R} \\
&= \gamma_{yzL}
\end{aligned} \tag{3.5}$$

3.3 PHYSICAL AND COMPUTATIONAL DOMAINS

The buckling analysis of these local skin segments is enhanced by mapping their physical domain into a computational domain. Consider a general quadrilateral or triangular panels subjected to a state of combined in-plane loading as shown in Figure 3.2, where the loading and material properties are defined using the coordinate system

shown. The transformation from a physical domain to computational domain is necessary when dealing with general quadrilateral and triangular geometries in order to facilitate the computation of linear stiffness and geometric stiffness matrices and imposition of boundary conditions.

The physical domain $\mathcal{D}[x,y]$ is transformed to a computational domain $\mathcal{D}[\xi,\eta]$ as indicated in Figure 3.2. The mapping for a quadrilateral is

$$\begin{aligned} x(\xi,\eta) &= \sum_{i=1}^{4} N_i(\xi,\eta)x_i \\ y(\xi,\eta) &= \sum_{i=1}^{4} N_i(\xi,\eta)y_i \end{aligned} \tag{3.6}$$

where $x_i(i=1,2,3,4)$ and $y_i(i=1,2,3,4)$ are the physical coordinates of the i^{th} corner of the plate, ξ and η are the natural coordinates for the quadrilateral geometries, and N_i $(i=1,2,3,4)$ are the bilinear mapping functions given by

$$\begin{aligned} N_1(\xi,\eta) &= \frac{1}{4}(1-\xi)(1+\eta) \\ N_2(\xi,\eta) &= \frac{1}{4}(1+\xi)(1+\eta) \\ N_3(\xi,\eta) &= \frac{1}{4}(1+\xi)(1-\eta) \\ N_4(\xi,\eta) &= \frac{1}{4}(1-\xi)(1-\eta) \end{aligned}$$

The Jacobian of the transformation is

$$\mathbf{J} = \begin{bmatrix} \frac{\partial x}{\partial \xi} & \frac{\partial y}{\partial \xi} \\ \frac{\partial x}{\partial \eta} & \frac{\partial y}{\partial \eta} \end{bmatrix} \tag{3.7}$$

which is independent of the natural coordinates for general parallelogram-shaped geometries. This results in substantial computational savings in the overall formulation.

The mapping for a general triangle is

$$\begin{aligned} x(\xi,\eta,\rho) &= \xi x_1 + \eta x_2 + \rho x_3 \\ y(\xi,\eta,\rho) &= \xi y_1 + \eta y_2 + \rho y_3 \end{aligned} \tag{3.8}$$

where ξ, η and ρ are the area coordinates for the case of triangular geometries, and $x_i(i = 1,2,3)$ and $y_i(i = 1,2,3)$ are the physical coordinates of the i^{th} corner of the plate. Note that the third area coordinate will be expressed in terms of the other two or $\rho = (1 - \xi - \eta)$ based on the constraint that the sum of the area coordinates must be equal to one. The Jacobian of the transformation is independent of the area coordinates. The Jacobian, in either case, is used to relate derivatives in the two domains.

3.4 STRESS-STRAIN RELATIONS

The stresses are related to the strains for the k^{th} ply of a laminate by ([27])

$$\begin{Bmatrix} \sigma_x \\ \sigma_y \\ \tau_{xy} \\ \tau_{xz} \\ \tau_{yz} \end{Bmatrix}_k = \begin{bmatrix} Q_{11} & Q_{12} & Q_{16} & 0 & 0 \\ Q_{12} & Q_{22} & Q_{26} & 0 & 0 \\ Q_{16} & Q_{26} & Q_{66} & 0 & 0 \\ 0 & 0 & 0 & Q_{44} & Q_{45} \\ 0 & 0 & 0 & Q_{45} & Q_{55} \end{bmatrix}_k \begin{Bmatrix} \epsilon_x \\ \epsilon_y \\ \gamma_{xy} \\ \gamma_{xz} \\ \gamma_{yz} \end{Bmatrix}_k \tag{3.9}$$

The force and moment resultants acting on the differential element shown in Figure 3.1 are

$$\begin{Bmatrix} N_x \\ N_y \\ N_{xy} \\ M_x \\ M_y \\ M_{xy} \\ Q_x \\ Q_y \end{Bmatrix} = \int \begin{Bmatrix} \sigma_x \\ \sigma_y \\ \tau_{xy} \\ z\sigma_x \\ z\sigma_y \\ z\tau_{xy} \\ \tau_{xz} \\ \tau_{yz} \end{Bmatrix}_k dz \tag{3.10}$$

Substituting Equation (3.9) in Equation (3.10) and carrying out integration over the laminate thickness gives;

$$\begin{Bmatrix} N_x \\ N_y \\ N_{xy} \\ M_x \\ M_y \\ M_{xy} \\ Q_x \\ Q_y \end{Bmatrix} = \begin{bmatrix} A_{11} & A_{12} & A_{16} & B_{11} & B_{12} & B_{16} & 0 & 0 \\ A_{12} & A_{22} & A_{26} & B_{12} & B_{22} & B_{26} & 0 & 0 \\ A_{16} & A_{26} & A_{66} & B_{16} & B_{26} & B_{66} & 0 & 0 \\ B_{11} & B_{12} & B_{16} & D_{11} & D_{12} & D_{16} & 0 & 0 \\ B_{12} & B_{22} & B_{26} & D_{12} & D_{22} & D_{26} & 0 & 0 \\ B_{16} & B_{26} & B_{66} & D_{16} & D_{26} & D_{66} & 0 & 0 \\ 0 & 0 & 0 & 0 & 0 & 0 & C_{44} & C_{45} \\ 0 & 0 & 0 & 0 & 0 & 0 & C_{45} & C_{55} \end{bmatrix} \begin{Bmatrix} \epsilon_x^0 \\ \epsilon_y^0 \\ \gamma_{xy}^0 \\ \kappa_x \\ \kappa_y \\ \kappa_{xy} \\ \gamma_{xz} \\ \gamma_{yz} \end{Bmatrix} \tag{3.11}$$

where A_{ij} are the extensional stiffness coefficients, B_{ij} are the coupling stiffness coefficients, D_{ij} are the bending stiffness coefficients, and C_{rs} are the transverse shear stiffness coefficients.

3.5 THE MINIMUM ENERGY PRINCIPLE

The strain energy of a three-dimensional body is

$$\overline{U} = \frac{1}{2}\int_V (\sigma_x\epsilon_x + \sigma_y\epsilon_y + \sigma_z\epsilon_z + \tau_{xy}\gamma_{xy} + \tau_{xz}\gamma_{xz} + \tau_{yz}\gamma_{yz})dV \tag{3.12}$$

Substituting the strains from Equation (3.5) and the stresses from Equation (3.9) in Equation (3.12) for the potential energy functional leads to

$$\begin{aligned}
\overline{U} = \frac{1}{2}\int_V & \\
&\{\epsilon_{xL}(Q_{11}\epsilon_{xL} + Q_{12}\epsilon_{yL} + Q_{16}\gamma_{xyL}) + \epsilon_{xL}(Q_{11}\epsilon_{xNL} + Q_{12}\epsilon_{yNL} + Q_{16}\gamma_{xyNL}) \\
&+\epsilon_{xNL}(Q_{11}\epsilon_{xL} + Q_{12}\epsilon_{yL} + Q_{16}\gamma_{xyL}) + \epsilon_{xNL}(Q_{11}\epsilon_{xNL} + Q_{12}\epsilon_{yNL} + Q_{16}\gamma_{xyNL})\} \\
&+\{\epsilon_{yL}(Q_{22}\epsilon_{yL} + Q_{12}\epsilon_{xL} + Q_{26}\gamma_{xyL}) + \epsilon_{yL}(Q_{22}\epsilon_{yNL} + Q_{12}\epsilon_{xNL} + Q_{26}\gamma_{xyNL}) \\
&+\epsilon_{yNL}(Q_{22}\epsilon_{yL} + Q_{12}\epsilon_{xL} + Q_{26}\gamma_{xyL}) + \epsilon_{yNL}(Q_{22}\epsilon_{yNL} + Q_{12}\epsilon_{xNL} + Q_{26}\gamma_{xyNL})\} \\
&+\{\gamma_{xyL}(Q_{16}\epsilon_{xL} + Q_{26}\epsilon_{yL} + Q_{66}\gamma_{xyL}) + \gamma_{xyL}(Q_{16}\epsilon_{xNL} + Q_{26}\epsilon_{yNL} + Q_{66}\gamma_{xyNL}) \\
&+\gamma_{xyNL}(Q_{16}\epsilon_{xL} + Q_{26}\epsilon_{yL} + Q_{66}\gamma_{xyL}) + \gamma_{xyNL}(Q_{16}\epsilon_{xNL} + Q_{26}\epsilon_{yNL} + Q_{66}\gamma_{xyNL})\} \\
&+\{\gamma_{xzL}(Q_{44}\gamma_{xzL} + Q_{45}\gamma_{yzL})\} \\
&+\{\gamma_{yzL}(Q_{55}\gamma_{yzL} + Q_{45}\gamma_{xzL})\}dV
\end{aligned} \tag{3.13}$$

Terms like $\epsilon_{xL}(Q_{11}\epsilon_{xL} + Q_{12}\epsilon_{yL} + Q_{16}\gamma_{xyL})$ contribute to the linear stiffness matrix whereas terms like $\epsilon_{xL}(Q_{11}\epsilon_{xNL} + Q_{12}\epsilon_{yNL} + Q_{16}\gamma_{xyNL})$ and $\epsilon_{xNL}(Q_{11}\epsilon_{xNL} + Q_{12}\epsilon_{yNL} + Q_{16}\gamma_{xyNL})$ contribute to the nonlinear stiffness matrix. In a linear buckling analysis, the nonlinear stiffness matrix is linearized and higher-order terms neglected. If a uniform prebuckling stress state is prescribed then

$$\overline{N}_x = \int \overline{\sigma}_x dz = \int (Q_{11}\overline{\epsilon}_{xL} + Q_{12}\overline{\epsilon}_{yL} + Q_{16}\overline{\gamma}_{xyL})dz$$
$$\overline{N}_y = \int \overline{\sigma}_y dz = \int (Q_{12}\overline{\epsilon}_{xL} + Q_{22}\overline{\epsilon}_{yL} + Q_{26}\overline{\gamma}_{xyL})dz$$
$$\overline{N}_{xy} = \int \overline{\tau}_{xy} dz = \int (Q_{16}\overline{\epsilon}_{xL} + Q_{26}\overline{\epsilon}_{yL} + Q_{66}\overline{\gamma}_{xyL})dz \qquad (3.14)$$

where $\overline{N}_x$, $\overline{N}_y$, and $\overline{N}_{xy}$ are the prescribed in-plane loadings in terms of the membrane prebuckling stress resultants based on a linearized analysis.

Hence considering a linear buckling analysis and a uniform prescribed pre-stress state, the potential energy for a circular cylindrical panel or shell is

$$\pi = \frac{1}{2}\int_V$$
$$\{\ \epsilon_{xL}(Q_{11}\epsilon_{xL} + Q_{12}\epsilon_{yL} + Q_{16}\gamma_{xyL}) + \epsilon_{yL}(Q_{12}\epsilon_{xL} + Q_{22}\epsilon_{yL} + Q_{26}\gamma_{xyL}) +$$
$$\gamma_{xyL}(Q_{16}\epsilon_{xL} + Q_{26}\epsilon_{yL} + Q_{66}\gamma_{xyL}) + \gamma_{xzL}(Q_{44}\gamma_{xzL} + Q_{45}\gamma_{yzL}) +$$
$$\gamma_{yzL}(Q_{55}\gamma_{yzL} + Q_{45}\gamma_{xzL})\ \}dV$$
$$-\frac{1}{2}\int_A (\ \overline{N}_x\epsilon_{xNL} + \overline{N}_y\epsilon_{yNL} + \overline{N}_{xy}\gamma_{xyNL}\ )\ dA \qquad (3.15)$$

The volume integral represents the linear elastic strain energy, and the area integral represents the work done by the in-plane prebuckling stress state. The critical loading is determined on the basis that during buckling the elastic strain energy stored in the structure is equal to the work done by the applied loading [51, 52]. The potential energy is thus minimized to yield the critical buckling load of the structure. The above expression for the potential energy functional will be used with a Rayleigh-Ritz method to develop the buckling analysis formulation for panels with parallelogram-shaped and general triangular-shaped geometries. The linear strain used will be that of Equation (3.5) in order to implement different shell theories.

3.6 THE RAYLEIGH-RITZ METHOD

The Rayleigh-Ritz method is an approximate method for solving a certain class of problems. Accordingly, trial functions with some unknown coefficients and satisfying the essential or geometric boundary conditions are introduced in the energy functional of the problem. The minimum conditions of this functional are then imposed, and resulting algebraic equations are solved for the unknown coefficients. These trial functions are called the "Ritz" functions.

The Ritz functions used here are expressed in terms of natural coordinates for the quadrilateral geometry or area coordinates for the triangular geometry for displacement field. The components of the displacement vector are three translations $(D_1, D_2, D_3 = u_0, v_0, w)$ and two cross-sectional or bending rotations $(D_4, D_5 = \phi_x, \phi_y)$ when considering transverse-shear deformation effects. Each displacement component is approximated independently by a different Ritz function. The approximation for the i^{th} component of the displacement vector is given by

$$\begin{aligned} D_i(\xi,\eta) &= \sum_{j=1}^{N} a_{ij} d_{ij} \\ &= \sum_{j=1}^{N} a_{ij} \Gamma_i(\xi,\eta) f_j(\xi,\eta) \quad \text{for } i = 1,2,3,4,5 \end{aligned} \tag{3.16}$$

where d_{ij} represents the j^{th} term in the N-term approximation for the i^{th} displacement component, a_{ij} are unknown coefficients to be determined, and $\Gamma_i(\xi,\eta)$ are the circulation functions.

The circulation functions Γ_i in Equation (3.16) are the used to impose different boundary conditions along each edge of the plate. Each term Γ_i is the product of three functions in the case of the triangular plate geometry and four functions in the case of the quadrilateral plate geometry. Each function is the equation of an edge of the triangular or quadrilateral plate as shown in Figure 3.2 raised to an independent exponent for each displacement component. Thus, the circulation functions for the

quadrilateral plate are

$$\Gamma_i = (1-\eta)^{p_i}(1-\xi)^{q_i}(1+\eta)^{r_i}(1+\xi)^{s_i}$$

and for the triangular plate are

$$\Gamma_i = \xi^{p_i}\eta^{q_i}(1-\xi-\eta)^{r_i} \tag{3.17}$$

For example, considering the quadrilateral plate case, p_i refers to edge 1, q_i refers to edge 2, r_i refers to edge 3, s_i refers to edge 4 as indicated in Figure (3.2) These exponents are used to impose different boundary conditions. If the i^{th} displacement component is restrained or free on a given edge, then the exponent for that edge will have a value of zero. If the i^{th} displacement component is constrained on a given edge, then the exponent for that edge will have a value of one. Only geometric boundary conditions are imposed in this approach. Thus, a simply supported condition for bending fields can be imposed on edge 1 by setting:

- $p_3 = 1$ for w, $p_4 = 0$, for ϕ_x $p_5 = 0$ for ϕ_y

A clamped conditions for bending fields can be imposed on edge 1 by setting:

- $p_3 = 1$ for w, $p_4 = 1$ for ϕ_x, $p_5 = 1$ for ϕ_y

A free-edge condition can be imposed on edge 1 by setting:

- $p_i = 0$ for u_0, v_0, w, ϕ_x and ϕ_y

In the case of classical laminated plate theory, these exponents takes on different values depending on the type of boundary conditions. If the i^{th} displacement component is free on a given edge, then the exponent for that edge is zero. If the i^{th} displacement component is constrained but not clamped, then the exponent for that edge is one. If the i^{th} displacement component is constrained and clamped, then the exponent for that edge is two which will force the slope to be zero as well. Thus a simply supported condition for bending can be imposed on edge 1 by setting:

- $p_3 = 1$ for w

A clamped conditions for bending fields can be imposed on edge 1 by setting:

- $p_3 = 2$ for w

A free-edge condition can be imposed on edge 1 by setting:

- $p_i = 0$ for u_0, v_0 and w

The term f_j in Equation (3.16) is a polynomial function in ξ and η, and in its simplest form is a power series in ξ and η (regular polynomial) and is expressed as

$$f_j(\xi,\eta) = \xi^{m_j}\eta^{n_j}$$
$$m_j,\ n_j = (0,0),\ (1,0),\ (0,1),\ (2,0),\ (1,1),\ (0,2),\ldots \qquad (3.18)$$

The values of m_j and n_j are used basically to define terms in a two-dimensional Pascal's triangle. The number of terms N in Equation (3.16) defines the order of a complete function in two variables. One disadvantage of this polynomial function is the tendency for ill-conditioning that occurs when N is very large. Characteristic orthogonal polynomials can be used to overcome the ill-conditioning problem (e.g., Ref. [42]). These are generated by the Gram-Schmidt process which can be summarized as follows. Let

$$d_i = \sum_{j=1}^{N} a_{ij}\Phi_j$$

where

$$\Phi_j = \Gamma_{ij} - \sum_{k=1}^{j-1} \alpha_{jk}\Phi_k$$

then

$$\Gamma_{i1} = \Gamma_i(\xi,\eta),\quad \Gamma_{ij} = \Gamma_i(\xi,\eta)\xi^{m_j}\eta^{n_j}$$

and

$$\alpha_{jk} = \frac{\int\int \Gamma_{ij}\Phi_k d\xi d\eta}{\int\int \Phi_k\Phi_k d\xi d\eta} \qquad (3.19)$$

The use of characteristic orthogonal polynomials, however, significantly increases the computing time needed to evaluate the linear and geometric stiffness matrices.

In the case of the quadrilateral plate geometry, most of the orthogonalizing coefficients

are zero corresponding to a circulation function (Γ_i) as defined by Equation (3.17). Orthogonal polynomials such as Legendre polynomials [53] can also be used where the function term f_j is defined as

$$\begin{aligned} f_j &= P_{m_j}(\xi)P_{n_j}(\eta) \\ m_j,\, n_j &= \begin{cases} (0,0),\ (0,1),\ (0,2),\ \ldots (0,N-1) \\ (1,0),\ (1,1),\ (1,2),\ \ldots (1,N-1)\ \ldots \\ (N-1,0),\ (N-1,1),\ (N-1,2),\ \ldots (N-1,N-1) \end{cases} \end{aligned} \tag{3.20}$$

where $P_{m_j}(\xi)$ denotes a Legendre polynomial of degree m_j in variable ξ. The Legendre polynomial, $P_n(\vartheta)$, is defined over the interval, $-1 \leq \vartheta \leq 1$ and it has some properties that can be exploited for computational efficiency in setting up the stiffness matrices. Regular polynomial will be used in buckling analyses of general parallelogram-shaped and general triangular-shaped geometries. The use of Legendre polynomial is restricted only to arbitrary quadrilateral geometries, because the natural coordinates are defined in the interval, $-1 \leq \xi, \eta \leq 1$, and (ξ, η) is an orthogonal coordinate system.

3.7 FORMULATION OF LINEAR STIFFNESS MATRIX

The linear stiffness matrix is derived from the linear elastic strain energy (Equation (3.15)) using the strain-displacement relation of Equation (3.3). Integrating in the z-direction the linear elastic strain energy, U, is

$$U = \tfrac{1}{2}\int_A \begin{Bmatrix} \epsilon_x^0 \\ \epsilon_y^0 \\ \gamma_{xy}^0 \\ \kappa_x \\ \kappa_y \\ \kappa_{xy} \\ \gamma_{xz} \\ \gamma_{yz} \end{Bmatrix}^T \begin{bmatrix} A_{11} & A_{12} & A_{16} & B_{11} & B_{12} & B_{16} & 0 & 0 \\ A_{12} & A_{22} & A_{26} & B_{12} & B_{22} & B_{26} & 0 & 0 \\ A_{16} & A_{26} & A_{66} & B_{16} & B_{26} & B_{66} & 0 & 0 \\ B_{11} & B_{12} & B_{16} & D_{11} & D_{12} & D_{16} & 0 & 0 \\ B_{12} & B_{22} & B_{26} & D_{12} & D_{22} & D_{26} & 0 & 0 \\ B_{16} & B_{26} & B_{66} & D_{16} & D_{26} & D_{66} & 0 & 0 \\ 0 & 0 & 0 & 0 & 0 & 0 & C_{44} & C_{45} \\ 0 & 0 & 0 & 0 & 0 & 0 & C_{45} & C_{55} \end{bmatrix} \begin{Bmatrix} \epsilon_x^0 \\ \epsilon_y^0 \\ \gamma_{xy}^0 \\ \kappa_x \\ \kappa_y \\ \kappa_{xy} \\ \gamma_{xz} \\ \gamma_{yz} \end{Bmatrix} dA$$

or

$$U = \mathbf{E_p}^T\, \mathbf{Q}\, \mathbf{E_p} \tag{3.21}$$

Since the physical domain of the structure has been transformed to a computational domain and the Ritz functions are expressed in terms of ξ and η, the strains have

to be expressed in terms of ξ and η. This can be done by using the elements of the inverse of the Jacobian, and therefore

$$\mathbf{E_p} = \mathbf{T}\,\mathbf{E_c} \tag{3.22}$$

where

$$\mathbf{T} =$$

$$\begin{bmatrix}
\xi_{,x} & \eta_{,x} & 0 & 0 & 0 & 0 & 0 & 0 & 0 & 0 & 0 & 0 & 0 & 0 \\
0 & 0 & \xi_{,y} & \eta_{,y} & 0 & 0 & 0 & 0 & 0 & 0 & 0 & \frac{1}{R} & 0 & 0 \\
\xi_{,y} & \eta_{,y} & \xi_{,x} & \eta_{,x} & 0 & 0 & 0 & 0 & 0 & 0 & 0 & 0 & 0 & 0 \\
0 & 0 & 0 & 0 & 0 & 0 & \xi_{,x} & \eta_{,x} & 0 & 0 & 0 & 0 & 0 & 0 \\
0 & 0 & 0 & 0 & 0 & 0 & 0 & 0 & \xi_{,y} & \eta_{,y} & 0 & 0 & 0 & 0 \\
-\frac{C_2}{2R}\xi_{,y} & -\frac{C_2}{2R}\eta_{,y} & \frac{C_2}{2R}\xi_{,x} & \frac{C_2}{2R}\eta_{,x} & 0 & 0 & \xi_{,y} & \eta_{,y} & \xi_{,x} & \eta_{,x} & 0 & 0 & 0 & 0 \\
0 & 0 & 0 & 0 & \xi_{,x} & \eta_{,x} & 0 & 0 & 0 & 0 & 0 & 0 & 1 & 0 \\
0 & 0 & 0 & 0 & \xi_{,y} & \eta_{,y} & 0 & 0 & 0 & 0 & \frac{-C_1}{R} & 0 & 0 & 1
\end{bmatrix} \tag{3.23}$$

and

$$\mathbf{E_c} =$$

$$\{\, u_{0,\xi} \quad u_{0,\eta} \quad v_{0,\xi} \quad v_{0,\eta} \quad w_{,\xi} \quad w_{,\eta} \quad \phi_{x,\xi} \quad \phi_{x,\eta} \quad \phi_{y,\xi} \quad \phi_{y,\eta} \quad v_0 \quad w \quad \phi_x \quad \phi_y \,\}^T \tag{3.24}$$

The elements of matrix $\mathbf{T}$ are all constant since the Jacobian for general parallelogram-shaped and general triangular plate geometries is independent of ξ and η.

The i^{th} term of the N-term approximation for the displacement vector is

$$\begin{Bmatrix} u_0 \\ v_0 \\ w \\ \phi_x \\ \phi_y \end{Bmatrix} = \begin{bmatrix} U_i & 0 & 0 & 0 & 0 \\ 0 & V_i & 0 & 0 & 0 \\ 0 & 0 & W_i & 0 & 0 \\ 0 & 0 & 0 & \Phi_{xi} & 0 \\ 0 & 0 & 0 & 0 & \Phi_{yi} \end{bmatrix} \begin{Bmatrix} a_{1i} \\ a_{2i} \\ a_{3i} \\ a_{4i} \\ a_{5i} \end{Bmatrix} \tag{3.25}$$

where U_i, V_i, W_i, Φ_{xi}, and Φ_{yi} are Ritz functions as discussed in the previous section.

Using Equation (3.25), $\mathbf{E_c}$ can be written as

$$\begin{Bmatrix} u_{0,\xi} \\ u_{0,\eta} \\ v_{0,\xi} \\ v_{0,\eta} \\ w_{,\xi} \\ w_{,\eta} \\ \phi_{x,\xi} \\ \phi_{x,\eta} \\ \phi_{y,\xi} \\ \phi_{y,\eta} \\ v_0 \\ w \\ \phi_x \\ \phi_y \end{Bmatrix} = \begin{bmatrix} U_{i,\xi} & 0 & 0 & 0 & 0 \\ U_{i,\eta} & 0 & 0 & 0 & 0 \\ 0 & V_{i,\xi} & 0 & 0 & 0 \\ 0 & V_{i,\eta} & 0 & 0 & 0 \\ 0 & 0 & W_{i,\xi} & 0 & 0 \\ 0 & 0 & W_{i,\eta} & 0 & 0 \\ 0 & 0 & 0 & \Phi_{xi,\xi} & 0 \\ 0 & 0 & 0 & \Phi_{xi,\eta} & 0 \\ 0 & 0 & 0 & 0 & \Phi_{yi,\xi} \\ 0 & 0 & 0 & 0 & \Phi_{yi,\eta} \\ 0 & V_i & 0 & 0 & 0 \\ 0 & 0 & W_i & 0 & 0 \\ 0 & 0 & 0 & \Phi_{xi} & 0 \\ 0 & 0 & 0 & 0 & \Phi_{yi} \end{bmatrix} \begin{Bmatrix} a_{1i} \\ a_{2i} \\ a_{3i} \\ a_{4i} \\ a_{5i} \end{Bmatrix}$$

or

$$\mathbf{E_c} = \mathbf{\Theta_i}\, \mathbf{q_i} \tag{3.26}$$

Therefore, using Equation (3.22) and (3.26) the strain vector, $\mathbf{E_p}$, is written as

$$\mathbf{E_p} = \mathbf{T\Theta_i q_i} \tag{3.27}$$

which on substitution in Equation (3.21) for the linear elastic strain energy gives

$$\begin{aligned} U &= \frac{1}{2} \int_{A_c} \mathbf{q_i}^T \left[\mathbf{\Theta_i}^T \mathbf{T}^T \mathbf{Q}\, \mathbf{T}\, \mathbf{\Theta_j} \right] \mathbf{q_j} \, |\mathbf{J}| \, d\xi d\eta \\ &= \frac{1}{2} \int_{A_c} \mathbf{q_i}^T \left[\mathbf{\Theta_i}^T \mathbf{H}\, \mathbf{\Theta_j} \right] \mathbf{q_j} \, |\mathbf{J}| \, d\xi d\eta \\ &= \frac{1}{2} \mathbf{q_i}^T \left\{ \int_{A_c} \bar{\mathbf{k}}_{\mathbf{ij}} \, |\mathbf{J}| \, d\xi d\eta \right\} \mathbf{q_j} \\ &= \frac{1}{2} \mathbf{q_i}^T \mathbf{K_{ij}}\, \mathbf{q_j} \end{aligned} \tag{3.28}$$

where

$$\begin{aligned} \mathbf{H} &= \mathbf{T}^T \mathbf{Q}\, \mathbf{T} \\ \bar{\mathbf{k}}_{\mathbf{ij}} &= \mathbf{\Theta_i}^T \mathbf{H}\, \mathbf{\Theta_j} \\ \mathbf{K_{ij}} &= \int_{A_c} \bar{\mathbf{k}}_{\mathbf{ij}} \, |\mathbf{J}| \, d\xi d\eta \end{aligned}$$

where A_c is the area for the computational domain.

The non-zero entries of matrix $\mathbf{H}$ are shown below in a generic manner. Although $\mathbf{H}$ is obtained numerically in the computerized implementation of the buckling

analysis, only the non-zero entries are used in computing the stiffness matrix to avoid unnecessary computations. The non-zero entries are identified for fully populated **J**, A_{ij}, B_{ij}, D_{ij}, and C_{pq} matrices. Hence,

$$\mathbf{H} = \begin{bmatrix}
h_{11} & h_{12} & h_{13} & h_{14} & 0 & 0 & h_{17} & h_{18} & h_{19} & h_{1,10} & 0 & h_{1,12} & 0 & 0 \\
h_{21} & h_{22} & h_{23} & h_{24} & 0 & 0 & h_{27} & h_{28} & h_{29} & h_{2,10} & 0 & h_{2,12} & 0 & 0 \\
h_{31} & h_{32} & h_{33} & h_{34} & 0 & 0 & h_{37} & h_{38} & h_{39} & h_{3,10} & 0 & h_{3,12} & 0 & 0 \\
h_{41} & h_{42} & h_{43} & h_{44} & 0 & 0 & h_{47} & h_{48} & h_{49} & h_{4,10} & 0 & h_{4,12} & 0 & 0 \\
0 & 0 & 0 & 0 & h_{55} & h_{56} & 0 & 0 & 0 & 0 & h_{5,11} & 0 & h_{5,13} & h_{5,14} \\
0 & 0 & 0 & 0 & h_{65} & h_{66} & 0 & 0 & 0 & 0 & h_{6,11} & 0 & h_{6,13} & h_{6,14} \\
h_{71} & h_{72} & h_{73} & h_{74} & 0 & 0 & h_{77} & h_{78} & h_{79} & h_{7,10} & 0 & h_{7,12} & 0 & 0 \\
h_{81} & h_{82} & h_{83} & h_{84} & 0 & 0 & h_{87} & h_{88} & h_{89} & h_{8,10} & 0 & h_{8,12} & 0 & 0 \\
h_{91} & h_{92} & h_{93} & h_{94} & 0 & 0 & h_{97} & h_{98} & h_{99} & h_{9,10} & 0 & h_{9,12} & 0 & 0 \\
h_{10,1} & h_{10,2} & h_{10,3} & h_{10,4} & 0 & 0 & h_{10,7} & h_{10,8} & h_{10,9} & h_{10,10} & 0 & h_{10,12} & 0 & 0 \\
0 & 0 & 0 & 0 & h_{11,5} & h_{11,6} & 0 & 0 & 0 & 0 & h_{11,11} & 0 & h_{11,13} & h_{11,14} \\
h_{12,1} & h_{12,2} & h_{12,3} & h_{12,4} & 0 & 0 & h_{12,7} & h_{12,8} & h_{12,9} & h_{12,10} & 0 & h_{12,12} & 0 & 0 \\
0 & 0 & 0 & 0 & h_{13,5} & h_{13,6} & 0 & 0 & 0 & 0 & h_{13,11} & 0 & h_{13,13} & h_{13,14} \\
0 & 0 & 0 & 0 & h_{14,5} & h_{14,6} & 0 & 0 & 0 & 0 & h_{14,11} & 0 & h_{14,13} & h_{14,14}
\end{bmatrix} \tag{3.29}$$

The matrix, $\overline{\mathrm{k}}_{\mathrm{ij}}$, is also fully populated and has the form

$$\overline{\mathrm{k}}_{\mathrm{ij}} = \begin{bmatrix}
\overline{k}_{11} & \overline{k}_{12} & \overline{k}_{13} & \overline{k}_{14} & \overline{k}_{15} \\
\overline{k}_{21} & \overline{k}_{22} & \overline{k}_{23} & \overline{k}_{24} & \overline{k}_{25} \\
\overline{k}_{31} & \overline{k}_{32} & \overline{k}_{33} & \overline{k}_{34} & \overline{k}_{35} \\
\overline{k}_{41} & \overline{k}_{42} & \overline{k}_{43} & \overline{k}_{44} & \overline{k}_{45} \\
\overline{k}_{51} & \overline{k}_{52} & \overline{k}_{53} & \overline{k}_{54} & \overline{k}_{55}
\end{bmatrix} \tag{3.30}$$

where

$$\overline{k}_{11} = (h_{11}U_{i,\xi} + h_{12}U_{i,\eta})U_{j,\xi} + (h_{12}U_{i,\xi} + h_{22}U_{i,\eta})U_{j,\eta}$$

$$\overline{k}_{12} = (h_{13}U_{i,\xi} + h_{23}U_{i,\eta})V_{j,\xi} + (h_{14}U_{i,\xi} + h_{24}U_{i,\eta})V_{j,\eta}$$

$$\overline{k}_{13} = (h_{1,12}U_{i,\xi} + h_{2,12}U_{i,\eta})W_j$$

$$\overline{k}_{14} = (h_{17}U_{i,\xi} + h_{27}U_{i,\eta})\Phi_{xj,\xi} + (h_{18}U_{i,\xi} + h_{28}U_{i,\eta})\Phi_{xj,\eta}$$

$$\overline{k}_{15} = (h_{19}U_{i,\xi} + h_{29}U_{i,\eta})\Phi_{yj,\xi} + (h_{1,10}U_{i,\xi} + h_{2,10}U_{i,\eta})\Phi_{yj,\eta}$$

$$\overline{k}_{21} = (h_{31}V_{i,\xi} + h_{41}V_{i,\eta})U_{j,\xi} + (h_{32}V_{i,\xi} + h_{42}V_{i,\eta})U_{j,\eta}$$

$$\overline{k}_{22} = (h_{33}V_{i,\xi} + h_{43}V_{i,\eta})V_{j,\xi} + (h_{34}V_{i,\xi} + h_{44}V_{i,\eta})V_{j,\eta} + h_{11,11}V_iV_j$$

$$
\begin{aligned}
\overline{k}_{23} &= h_{11,5}V_iW_{j,\xi} + h_{11,6}V_iW_{j,\eta} + h_{3,12}V_{i,\xi}W_j + h_{4,12}V_{i,\eta}W_j \\
\overline{k}_{24} &= (h_{37}V_{i,\xi} + h_{47}V_{i,\eta})\Phi_{xj,\xi} + (h_{38}V_{i,\xi} + h_{48}V_{i,\eta})\Phi_{xj,\eta} + h_{11,13}V_i\Phi_{xj} \\
\overline{k}_{25} &= (h_{39}V_{i,\xi} + h_{49}V_{i,\eta})\Phi_{yj,\xi} + (h_{3,10}V_{i,\xi} + h_{4,10}V_{i,\eta})\Phi_{yj,\eta} + h_{11,14}V_i\Phi_{yj} \\
\overline{k}_{31} &= (h_{1,12}U_{j,\xi} + h_{2,12}U_{j,\eta})W_i \\
\overline{k}_{32} &= h_{11,5}V_jW_{i,\xi} + h_{11,6}V_jW_{i,\eta} + h_{3,12}V_{j,\xi}W_i + h_{4,12}V_{j,\eta}W_i \\
\overline{k}_{33} &= (h_{55}W_{i,\xi} + h_{65}W_{i,\eta})W_{j,\xi} + (h_{56}W_{i,\xi} + h_{66}W_{i,\eta})W_{j,\eta} + h_{12,12}W_iW_j \\
\overline{k}_{34} &= h_{12,7}\Phi_{xj,\xi}W_i + h_{12,8}\Phi_{xj,\eta}W_i + (h_{5,13}W_{i,\xi} + h_{6,13}W_{i,\eta})\Phi_{xj} \\
\overline{k}_{35} &= h_{12,9}\Phi_{yj,\xi}W_i + h_{12,10}\Phi_{yj,\eta}W_i + (h_{5,14}W_{i,\xi} + h_{6,14}W_{i,\eta})\Phi_{yj} \\
\overline{k}_{41} &= (h_{71}\Phi_{xi,\xi} + h_{81}\Phi_{xi,\eta})U_{j,\xi} + (h_{72}\Phi_{xi,\xi} + h_{72}\Phi_{xi,\eta})U_{j,\eta} \\
\overline{k}_{42} &= (h_{73}\Phi_{xi,\xi} + h_{83}\Phi_{xi,\eta})V_{j,\xi} + (h_{74}\Phi_{xi,\xi} + h_{74}\Phi_{xi,\eta})V_{j,\eta} + h_{13,11}\Phi_{xi}V_j \\
\overline{k}_{43} &= h_{12,7}\Phi_{xi,\xi}W_j + h_{12,8}\Phi_{xi,\eta}W_j + (h_{5,13}W_{j,\xi} + h_{6,13}W_{j,\eta})\Phi_{xi} \\
\overline{k}_{44} &= (h_{77}\Phi_{xi,\xi} + h_{87}\Phi_{xi,\eta})\Phi_{xj,\xi} + (h_{78}\Phi_{xi,\xi} + h_{88}\Phi_{xi,\eta})\Phi_{xj,\eta} + h_{13,13}\Phi_{xi}\Phi_{xj} \\
\overline{k}_{45} &= (h_{79}\Phi_{xi,\xi} + h_{89}\Phi_{xi,\eta})\Phi_{yj,\xi} + (h_{7,10}\Phi_{xi,\xi} + h_{8,10}\Phi_{xi,\eta})\Phi_{yj,\eta} + h_{13,14}\Phi_{xi}\Phi_{yj} \\
\overline{k}_{51} &= (h_{91}\Phi_{yi,\xi} + h_{10,1}\Phi_{yi,\eta})U_{j,\xi} + (h_{92}\Phi_{yi,\xi} + h_{10,2}\Phi_{yi,\eta})U_{j,\eta} \\
\overline{k}_{52} &= (h_{93}\Phi_{yi,\xi} + h_{10,3}\Phi_{yi,\eta})V_{j,\xi} + (h_{94}\Phi_{yi,\xi} + h_{10,4}\Phi_{yi,\eta})V_{j,\eta} + h_{14,11}\Phi_{yi}V_j \\
\overline{k}_{53} &= (h_{9,12}\Phi_{yi,\xi} + h_{10,12}\Phi_{yi,\eta})W_j + (h_{14,5}W_{j,\xi} + h_{14,6}W_{j,\eta})\Phi_{yi} \\
\overline{k}_{54} &= (h_{97}\Phi_{yi,\xi} + h_{10,7}\Phi_{yi,\eta})\Phi_{xj,\xi} + (h_{98}\Phi_{yi,\xi} + h_{10,8}\Phi_{yi,\eta})\Phi_{xj,\eta} + h_{14,13}\Phi_{yi}\Phi_{xj} \\
\overline{k}_{55} &= (h_{99}\Phi_{yi,\xi} + h_{10,9}\Phi_{yi,\eta})\Phi_{yj,\xi} + (h_{9,10}\Phi_{yi,\xi} + h_{10,10}\Phi_{yi,\eta})\Phi_{yj,\eta} + h_{14,14}\Phi_{yi}\Phi_{yj}
\end{aligned}
\tag{3.31}
$$

Finally, the structure's stiffness matrix, $\mathbf{K_{ij}}$ is obtained on integrating $\overline{\mathbf{k}}_{\mathbf{ij}}$ over the computational domain. The integration is carried out analytically by utilizing symbolic computational techniques rather than numerical integration which result in significant savings in computational time. The analytical integration is discussed in Appendix A.

3.8 THE GEOMETRIC STIFFNESS MATRIX

The geometric stiffness matrix is derived from the work done, W_d, by the applied prebuckling loading as given by Equation (3.15) as identified by the linearization process. The formulation is done in a similar way as that for the linear stiffness matrix beginning with

$$W_d = \frac{1}{2}\int_A (\overline{N}_x \epsilon_{xNL} + \overline{N}_y \epsilon_{yNL} + \overline{N}_{xy} \gamma_{xyNL}) \, dA = \frac{1}{2}\int_A \varpi_d \, dA$$

where the nonlinear strain components from Equation (3.5) are

$$\begin{aligned} \epsilon_{xNL} &= \frac{1}{2}(v_{0,x}^2 + w_{,x}^2) \\ \epsilon_{yNL} &= \frac{1}{2}(u_{0,y}^2 + (w_{,y} - \frac{v_0}{R})^2) \\ \gamma_{xyNL} &= -u_{0,y}(v_{0,y} + \frac{w}{R}) - v_{0,x} u_{0,x} + w_{,x}(w_{,y} - \frac{v_0}{R}) \end{aligned} \tag{3.32}$$

This equation can be written in matrix form as;

$$\varpi_d = \begin{Bmatrix} w_{,x} \\ w_{,y} \\ v_{0,x} \\ v_{0,y} \\ u_{0,x} \\ u_{0,y} \\ \frac{v_0}{R} \\ \frac{w}{R} \end{Bmatrix}^T \begin{bmatrix} \overline{N}_x & \overline{N}_{xy} & 0 & 0 & 0 & 0 & -\overline{N}_{xy} & 0 \\ \overline{N}_{xy} & \overline{N}_y & 0 & 0 & 0 & 0 & -\overline{N}_y & 0 \\ 0 & 0 & \overline{N}_x & 0 & -\overline{N}_{xy} & 0 & 0 & 0 \\ 0 & 0 & 0 & 0 & 0 & -\overline{N}_{xy} & 0 & 0 \\ 0 & 0 & -\overline{N}_{xy} & 0 & 0 & 0 & 0 & 0 \\ 0 & 0 & 0 & -\overline{N}_{xy} & 0 & \overline{N}_y & 0 & -\overline{N}_{xy} \\ -\overline{N}_{xy} & -\overline{N}_y & 0 & 0 & 0 & 0 & \overline{N}_y & 0 \\ 0 & 0 & 0 & 0 & 0 & \overline{N}_{xy} & 0 & 0 \end{bmatrix} \begin{Bmatrix} w_{,x} \\ w_{,y} \\ v_{0,x} \\ v_{0,y} \\ u_{0,x} \\ u_{0,y} \\ \frac{v_0}{R} \\ \frac{w}{R} \end{Bmatrix}$$

or

$$\varpi_d = \mathbf{D_p}^T \, \mathbf{P} \, \mathbf{D_p} \tag{3.33}$$

Expressing the vector $\mathbf{D_p}$ in terms of ξ and η

$$\begin{Bmatrix} w_{,x} \\ w_{,y} \\ v_{0,x} \\ v_{0,y} \\ u_{0,x} \\ u_{0,y} \\ \frac{v_0}{R} \\ \frac{w}{R} \end{Bmatrix} = \begin{bmatrix} 0 & 0 & 0 & 0 & \xi_{,x} & \eta_{,x} & 0 & 0 \\ 0 & 0 & 0 & 0 & \xi_{,y} & \eta_{,y} & 0 & 0 \\ 0 & 0 & \xi_{,x} & \eta_{,x} & 0 & 0 & 0 & 0 \\ 0 & 0 & \xi_{,y} & \eta_{,y} & 0 & 0 & 0 & 0 \\ \xi_{,x} & \eta_{,x} & 0 & 0 & 0 & 0 & 0 & 0 \\ \xi_{,y} & \eta_{,y} & 0 & 0 & 0 & 0 & 0 & 0 \\ 0 & 0 & 0 & 0 & 0 & 0 & \frac{1}{R} & 0 \\ 0 & 0 & 0 & 0 & 0 & 0 & 0 & \frac{1}{R} \end{bmatrix} \begin{Bmatrix} u_{0,\xi} \\ u_{0,\eta} \\ v_{0,\xi} \\ v_{0,\eta} \\ w_{,\xi} \\ w_{,\eta} \\ v_0 \\ w \end{Bmatrix}$$

or

$$\mathbf{D_p} = \mathbf{T_g}\,\mathbf{D_c} \tag{3.34}$$

The i^{th} term of the N-term approximation for u_0, v_0, and w is

$$\begin{Bmatrix} u_0 \\ v_0 \\ w \end{Bmatrix} = \begin{bmatrix} U_i & 0 & 0 \\ 0 & V_i & 0 \\ 0 & 0 & W_i \end{bmatrix} \begin{Bmatrix} a_{1i} \\ a_{2i} \\ a_{3i} \end{Bmatrix} \tag{3.35}$$

and, thus $\mathbf{D_c}$ is expressed as

$$\begin{Bmatrix} u_{0,\xi} \\ u_{0,\eta} \\ v_{0,\xi} \\ v_{0,\eta} \\ w_{,\xi} \\ w_{,\eta} \\ v_0 \\ w \end{Bmatrix} = \begin{bmatrix} U_{i,\xi} & 0 & 0 \\ U_{i,\eta} & 0 & 0 \\ 0 & V_{i,\xi} & 0 \\ 0 & V_{i,\eta} & 0 \\ 0 & 0 & W_{i,\xi} \\ 0 & 0 & W_{i,\xi} \\ 0 & V_i & 0 \\ 0 & 0 & W_i \end{bmatrix} \begin{Bmatrix} a_{1i} \\ a_{2i} \\ a_{3i} \end{Bmatrix}$$

or

$$\mathbf{D_c} = \mathbf{\Theta_{gi}}\,\mathbf{q_{gi}} \tag{3.36}$$

Therefore, using Equation (3.34) and (3.36), $\mathbf{D_p}$ can be written in terms of the unknown coefficients as

$$\mathbf{D_p} = \mathbf{T_g}\,\mathbf{\Theta_{gi}}\,\mathbf{q_{gi}} \tag{3.37}$$

which on substitution into Equation (3.33) for the work done by the applied loading gives

$$\begin{aligned} W_d &= \frac{1}{2}\int_{A_e} \mathbf{q_{gi}}^T \left[\, \mathbf{\Theta_{gi}}^T\, \mathbf{T_g}^T\, \mathbf{P}\, \mathbf{T_g}\, \mathbf{\Theta_{gj}} \,\right] \mathbf{q_{gj}}\, |\mathbf{J}| d\xi d\eta \\ &= \frac{1}{2}\int_{A_e} \mathbf{q_{gi}}^T \left[\, \mathbf{\Theta_{gi}}^T\, \mathbf{G}\, \mathbf{\Theta_{gj}} \,\right] \mathbf{q_{gj}}\, |\mathbf{J}| d\xi d\eta \\ &= \frac{1}{2}\,\mathbf{q_{gi}}^T \left\{ \int_{A_e} \mathbf{\bar{k}_{gij}}\, |\mathbf{J}| d\xi d\eta \right\} \mathbf{q_{gj}} \\ &= \frac{1}{2}\,\mathbf{q_i}^T\, \mathbf{\bar{K}_{gij}}\, \mathbf{q_j} \end{aligned} \tag{3.38}$$

where

$$\begin{aligned} \mathbf{G} &= \mathbf{T_g}^T\, \mathbf{P}\, \mathbf{T_g} \\ \mathbf{\bar{k}_{gij}} &= \mathbf{\Theta_{gi}}^T\, \mathbf{G}\, \mathbf{\Theta_{gj}} \end{aligned}$$

$$\mathbf{K_{gij}} = \int_{A_e} \begin{bmatrix} [\,\overline{\mathbf{k}}_{\mathbf{gij}}\,]_{3\times3} & [\,0\,]_{3\times2} \\ [\,0\,]_{2\times3} & [\,0\,]_{2\times2} \end{bmatrix} |\mathbf{J}| d\xi d\eta$$

The non-zero entries of matrix **G** are shown below in a generic manner. Although **G** is obtained numerically in the computerized implementation of the buckling analysis, only the non-zero entries are used in computing the stiffness matrix to avoid unnecessary computations. These non-zero entries are identified for $\overline{N}_x$, $\overline{N}_y$, and $\overline{N}_{xy}$ combined in-plane loading.

$$\mathbf{G} = \begin{bmatrix} g_{11} & g_{12} & g_{13} & g_{14} & 0 & 0 & 0 & g_{18} \\ g_{21} & g_{22} & g_{23} & g_{24} & 0 & 0 & 0 & g_{28} \\ g_{31} & g_{32} & g_{33} & g_{34} & 0 & 0 & 0 & 0 \\ g_{41} & g_{42} & g_{43} & g_{44} & 0 & 0 & 0 & 0 \\ 0 & 0 & 0 & 0 & g_{55} & g_{56} & g_{57} & 0 \\ 0 & 0 & 0 & 0 & g_{65} & g_{66} & g_{67} & 0 \\ 0 & 0 & 0 & 0 & g_{75} & g_{76} & g_{77} & 0 \\ g_{81} & g_{82} & 0 & 0 & 0 & 0 & 0 & 0 \end{bmatrix} \tag{3.39}$$

The matrix $\overline{\mathbf{k}}_{\mathbf{gij}}$ is

$$\overline{\mathbf{k}}_{\mathbf{gij}} = \begin{bmatrix} \overline{k}_{g11} & \overline{k}_{g12} & \overline{k}_{g13} \\ \overline{k}_{g21} & \overline{k}_{g22} & \overline{k}_{g23} \\ \overline{k}_{g31} & \overline{k}_{g32} & \overline{k}_{g33} \end{bmatrix} \tag{3.40}$$

where

$$\begin{aligned}
\overline{k}_{g11} &= (g_{11}U_{i,\xi} + g_{21}U_{i,\eta})U_{j,\xi} + (g_{12}U_{i,\xi} + g_{22}U_{i,\eta})U_{j,\eta} \\
\overline{k}_{g12} &= (g_{13}U_{i,\xi} + g_{23}U_{i,\eta})V_{j,\xi} + (g_{14}U_{i,\xi} + g_{24}U_{i,\eta})V_{j,\eta} \\
\overline{k}_{g13} &= (g_{18}U_{i,\xi} + g_{28}U_{i,\eta})W_j \\
\overline{k}_{g21} &= (g_{31}V_{i,\xi} + g_{41}V_{i,\eta})U_{j,\xi} + (g_{32}V_{i,\xi} + g_{42}V_{i,\eta})U_{j,\eta} \\
\overline{k}_{g22} &= (g_{33}V_{i,\xi} + g_{43}V_{i,\eta})V_{j,\xi} + (g_{34}V_{i,\xi} + g_{44}V_{i,\eta})V_{j,\eta} + g_{77}V_iV_j \\
\overline{k}_{g23} &= (g_{75}V_i + g_{76}V_i)W_{j,\eta} \\
\overline{k}_{g31} &= (g_{81}U_{j,\xi} + g_{82}U_{j,\eta})W_i \\
\overline{k}_{g32} &= (g_{57}W_{i,\xi} + g_{67}W_{i,\eta})V_j \\
\overline{k}_{g33} &= (g_{55}W_{i,\xi} + g_{65}W_{i,\eta})W_{j,\xi} + (g_{56}W_{i,\xi} + g_{66}W_{i,\eta})W_{j,\eta}
\end{aligned} \tag{3.41}$$

Finally, the structure's geometric stiffness matrix, $\mathbf{K_{gij}}$ is obtained on integrating $\overline{\mathbf{k}}_{\mathbf{gij}}$ over the computational domain. The integration is carried out analytically by utilizing symbolic computational techniques as discussed in Appendix A.

3.9 THE EIGENVALUE PROBLEM

The critical loading is determined on the basis of the principle that during buckling the elastic strain energy stored in the structure is equal to the work done by the applied loading and that adjacent equilibrium configuration exists at the same loading level [51, 52]. Having thus obtain the linear elastic strain energy and the work done by the applied in-plane loadings in terms of unknown Rayleigh-Ritz coefficient, the potential energy can be written as

$$\pi = \frac{1}{2} \sum_{i=1}^{N} \sum_{j=1}^{N} \mathbf{q_i}^T \left(\overline{\mathbf{K}}_{\mathbf{ij}} - \lambda \, \overline{\mathbf{K}}_{\mathbf{gij}} \right) \mathbf{q_j} \tag{3.42}$$

where λ is a load factor used to identify the critical in-plane loadings. Minimizing the potential energy with respect to $\mathbf{q_j}$ leads to

$$\sum_{i=1}^{N} \sum_{j=1}^{N} \left(\mathbf{K_{ij}} - \lambda \, \mathbf{K_{gij}} \right) \mathbf{q_j} = 0 \tag{3.43}$$

which is an eigenvalue problem. The eigenvalues and the eigenvectors of this system of equations can be obtained using an eigensolver. In this case, the minimum eigenvalue is the critical load factor (λ_{cr}), and the eigenvector corresponding to the minimum eigenvalue is the mode shape ($\mathbf{q_j}$).

3.10 BUCKLING OF QUADRILATERAL PLATES

Numerical results are presented for the buckling analyses of quadrilateral plates. Isotropic, orthotropic and anisotropic plates with different boundary conditions are considered. The present formulation is based on the principle of minimum total potential energy which slightly overpredicts buckling load results compared to values obtained from exact solutions. Also the present formulation does not introduce

any geometric distortion for the skewed plates considered since the mapping between the physical and computational domains does not introduce any errors. For simply supported conditions, only geometric boundary conditions are prescribed for the transverse deflection, and since transverse shear deformations are included, the bending rotations are independent of the out-of-plane deflection. Results from the present analysis were obtained using a larger number of terms than necessary for obtaining converged solutions. These results are compared with existing solutions and with results generated from finite element analyses.

Finite element results were obtained using STAGS [29]. The STAGS finite element analyses were carried out using a 30×30 mesh of C^1 4-node shell elements (element denoted as 410). More refined finite element meshes were considered and gave the same solutions as the 30×30 mesh. In these studies, the prebuckling stress state was prescribed to be uniform, and hence the linear static solution is avoided and a precisely defined prestress state is achieved. In the STAGS models, the simply supported boundary conditions along the skewed edges are only established approximately; that is, only the out-of-plane deflection is constrained to zero while the moment is not prescribed. An additional consideration for the finite element solutions for plate geometries with a non-zero skew angle is the susceptibility of the results to the effects of mesh or element distortion. Mesh distortion is known to affect the linear stress solution (e.g., Ref. [54]), and this behavior may also affect the buckling solution.

The finite element solutions may become increasingly susceptible to mesh distortion effects as the skew angle, ψ, increases.

Simulations are also made using VICON [55] wherein a semi-infinite plate is analyzed using complex Fourier series with constraints imposed at points along user-defined lines across the plate width at regular intervals to simulate a finite length plate. In the VICON models, the simply supported boundary condition is only

approximately satisfied along skewed edges, while along horizontal edges the simply supported boundary condition is exactly satisfied. As such, the VICON models for skewed plates with simply supported boundary conditions represent a plate which is continuous over the supports as is the case for an array of skewed panels rather than for a plate with moment free edges. Hence, the VICON models do not exactly represent a finite plate but approximate it depending on the number and type of constraint points and modes. Ten modes and ten constraint points were used in all VICON analyses. The VICON results converged from above for an increasing number of constraint modes and from below for an increasing number of constraint points.

Analytical results are now presented for four categories of problems. The first set of problems involves skewed isotropic plates with simply supported and clamped boundary conditions subjected to axial compression which was originally solved by Wittrick [56]. The second set of problems involves skewed orthotropic plates subjected to combined loading with simply supported boundary conditions. The third set of problems involves skewed anisotropic plates subjected to combined loading with various boundary conditions. Finally, the effect of transverse-shear deformation is studied for isotropic and anisotropic skewed plates. Results from the present analyses include those obtained using "regular" and "Legendre" polynomials in order to assess the performance of orthogonal polynomials.

3.10.1 Isotropic Plates Subjected to Uniaxial Compression

The buckling of clamped and simply supported isotropic skewed plate under uniaxial loading $\overline{N}_x$ has been studied by many researchers (e.g., see Refs. [31], [56]-[62]). Of these references, only Kitipornchai, et al. [58] included transverse-shear deformations using a first-order, shear-deformation theory (FSDT). Results from the present analysis are presented and compared with existing results in Tables 3.1 and 3.2. Results obtained using the STAGS finite element code and VICON are also presented.

Results are non-dimensionalized and presented as a buckling coefficient defined as

$$K = \frac{N_{cr} b^2 cos^4 \psi}{\pi^2 D_{22}} \tag{3.44}$$

where N_{cr} is the critical load, b is width of the plate, ψ is the skew angle (see Figure 3.3), and D_{22} is the transverse bending stiffness from classical laminated plate theory.

The convergence of the buckling coefficient versus the order of polynomial for a simply supported isotropic plate with skew angle (ψ) of 45 degrees and subjected to axial compression is given in Figure 3.5. It can be seen that the solutions obtained using Legendre polynomial converge faster than solutions obtained using regular polynomial. Results from the present analysis were obtained using a 66-term series solution (complete 10^{th} order polynomial per degree of freedom). Results obtained using Legendre polynomials are also obtained using up to 10^{th}-order polynomials. Results given in Tables 3.1 and 3.2 are for cases with all edges simply supported and all edges clamped, respectively, with an aspect ratio $(a/b) = 1$ and a thickness-to-width ratio $(t/b) = 0.001$.

Results shown in Table 3.1 for simply supported plates indicate that all solution methods are in excellent agreement for the rectangular plate geometry case (zero-skew-angle case). In all cases, the buckling mode shape has one half-wave in each direction. The analyses of Wang, et al. [31] and Kitipornchai, et al. [58] are essentially identical except that the latter study accounted for transverse-shear deformation effects. As such, the results from Ref. [58] are slightly lower in value (more flexible) than those of Ref. [31]. However, these plates are very thin and transverse-shear-deformation effects should be negligible. The results from the present formulation correlate very well with the results presented by Wang, et al. [31] and Kitipornchai, et al. [58]. Those presented by Mizusawa, et al. [61] are below that of the present analysis results and any other results shown. The STAGS finite element results follow the results of the present formulation, but mesh distortion appears to

influence the results as the skew angle increases. The VICON results are much higher in value than any other results except for the zero-skew-angle case. The differences for non-zero skew angle cases is due to the fact that the constraints on the skewed edges satisfy only the geometric boundary conditions.

The results obtained using Legendre polynomials are closer to those of Kitipornchai, et al. [58] and those of STAGS than the results obtained using regular polynomials. For skew angle of $\psi = 45°$, converged results are obtained with the use of Legendre polynomials up to 10^{th} order, while a 12^{th} order regular polynomial with 91-term series is needed to obtained converged results. Hence, the Ritz functions consisting of Legendre polynomials provide a more robust formulation for buckling analysis.

Results shown in Table 3.2 for the clamped plates indicate that the present approach gives buckling coefficients that are in good agreement with existing results. The results obtained using Legendre polynomials are in better agreement with the other results than those obtained using regular polynomials. For a skew angle of $\psi = 45°$, the formulation using Legendre polynomials is more robust. In all cases, the buckling mode has one half-wave in each direction. The VICON results for these cases are very close to the other results since clamped boundary conditions can be approximated easily along the skewed edges. The STAGS analysis results seem to be affected less by mesh distortion for clamped boundary conditions than for simply supported boundary conditions.

3.10.2 Orthotropic Plates under Combined Loading

Results are presented for orthotropic skewed plates with ratios $(a/b) = 1$ and $(t/b) = 0.001$. The boundary conditions considered are all edges simply supported. Four load cases are also considered for each set of boundary conditions:

- Load Case A: $\overline{N}_x = 1$, $\overline{N}_y = \overline{N}_{xy} = 0$

- Load Case B: $\overline{N}_x = \overline{N}_y = 1$, $\overline{N}_{xy}$ = -0.5
- Load Case C: $\overline{N}_x = \overline{N}_y = 1$, $\overline{N}_{xy} = 0$
- Load Case D: $\overline{N}_x = \overline{N}_y = 1$, $\overline{N}_{xy} = 0.5$

Load Case A corresponds to uniaxial compression; Load Case C corresponds to biaxial compression; and Load Cases B and D correspond to combined loading with negative and positive in-plane shear, respectively. These analysis results are presented in subsequent tables as a non-dimensional buckling coefficient K given by:

$$K = \frac{N_{cr} b^2}{\pi^2 D_{22}} \tag{3.45}$$

Results from the present analyses were obtained using a 78-term series (complete 11^{th} order polynomials). Results generated using STAGS and VICON are also presented and compared.

Orthotropic skewed plates with all edges simply supported and subjected to combined loading were also treated by Kennedy and Prabhakara [62] using the Galerkin method with Fourier series as approximation functions to solve the linearized stability equations for thin plates. The series solution satisfies natural boundary conditions, while the remaining boundary conditions are satisfied indirectly by a procedure given by Green [63]. A similar formulation used by Phillips and Gurdal [7] for buckling of orthotropic rhombic plates concluded that the solution from such a formulation converged from below. Kennedy and Prabhakara [62] used a 9-term series in their solution, while Phillips and Gurdal [7] used a 20-term series which they showed to represent a converged solution. However, Phillips and Gurdal [7] did not consider the variety of cases considered by Kennedy and Prabhakara [62]. Herein, results obtained from the present analysis are compared with those of Ref. [62] for cases with $D_{11}/D_{22} = 1$ and $D_{11}/D_{22} = 5$ in Tables 3.3 and 3.4, respectively. For both cases, $D_{66}/D_{22} = 0.5$ and the major Poisson's ratio $\nu_{12} = 0.25$.

Comparison between results from Kennedy and Prabhakara [62] and those from the present formulation is very good for the case of $\psi = 15°$ and deviate as the skew angle increases. However, based on similar results in Ref. [7], the results from Ref. [62] converged from below and results from Ref. [62] may not represent completely converged solutions. Comparison between finite element results and those of the present formulation is also good with small differences occurring as the skew angle increases. A contributing factor to these differences is believed to be related to the increasing mesh distortion in the finite element models which in linear static analyses is known to cause a reduction in stiffness for the STAGS 410 element. The buckling coefficients predicted by VICON are all higher than any other results because of the manner in which the simply supported boundary conditions are imposed on the skewed edges.

Finally, the sign of the in-plane shear prestress has a significant effect on the buckling coefficient for skewed plates. The buckling coefficient for the load case with negative shear (Load Case B) is less than that for the load case with positive shear (Load Case D). Considering the buckling coefficients for simply supported plates with $D_{11}/D_{22} = 1$ in Table 3.3, the percentage decrease of buckling coefficient of Load Case B from Load Case D for skew angle $\psi = 15°$ is 13.7 percent. The decrease in buckling coefficient is 23.4 and 28.3 for $\psi = 30°$ and $\psi = 45°$, respectively. For simply supported plates with $D_{11}/D_{22} = 5$ the decrease in buckling coefficient of Load Case B from Load Case D is 18.3 percent for $\psi = 15°$, 29.9 percent for $\psi = 30°$, and 34.2 percent for $\psi = 45°$. Hence, decrease in buckling coefficient due to the sign of the in-plane shear prestress increases with increase in skew angle and also as the degree of material orthotropy increases.

Finally, differences between the present formulation results obtained using regular polynomials, and those of STAGS for $D_{11}/D_{22} = 1$ are approximately 8 percent for $\psi = 45°$, while those for $D_{11}/D_{22} = 5$ are approximately 3 percent for $\psi = 45°$.

This suggests that errors due to mesh distortion are compensated, in some way, by material orthotropy. The results obtained using Legendre polynomials are closer to those from STAGS than the results obtained using regular polynomials.

3.10.3 Anisotropic Plates under Combined Loading

Anisotropic skewed plates with an aspect ratio $(a/b) = 1$, a thickness-width-ratio $(t/b) = 0.001$, and two laminate stacking sequences are considered here. Laminates 1 and 2 have ply stacking sequences of $[\pm 45/90/0]_s$ and $[45/90/-45]_s$, respectively. The nominal mechanical properties are $E_{11} = 24.5$ Msi, $E_{22} = 1.64$ Msi, $G_{12} = G_{13} = G_{23} = 0.87$ Msi and $\nu_{12} = 0.3$. The flexural orthotropy parameter, β, and the flexural anisotropy parameters γ_b and δ_b defined by Nemeth [64] are given by

$$\begin{aligned} \beta &= \frac{(D_{12} + 2D_{66})}{(D_{11}D_{22})^{1/2}} \\ \gamma_b &= \frac{D_{16}}{(D_{11}^3 D_{22})^{1/4}} \\ \delta_b &= \frac{D_{26}}{(D_{22}^3 D_{11})^{1/4}} \end{aligned} \tag{3.46}$$

and used to identify the degrees of orthotropy and anisotropy. For an isotropic plate, only β is non-zero and has a value of one. For an orthotropic plate, again only β is nonzero and increases in value as the degree of orthotropy increases. Laminate 1 has flexural anisotropy parameters of 0.208 and 0.182 for γ_b and δ_b, respectively, and a flexural orthotropy parameter, β, of 1.99. Laminate 2 has flexural anisotropy parameters of 0.528 and 0.376 for γ_b and δ_b, respectively, and a flexural orthotropy parameter, β, of 1.66. The flexural orthotropy parameter of Laminate 1 is of the same order as Laminate 2. However, Laminate 2 has higher flexural anisotropy parameters than Laminate 1 by at least a factor of two. Hence, Laminate 2 has a higher degree of anisotropy than Laminate 1. The buckling results are presented in terms of a non-dimensional buckling coefficient, given by Equation (3.45).

Results for anisotropic skewed plates are obtained using a 78-term series (11^{th} order) for regular polynomials and Legendre polynomials up to 11^{th} order. Results are given in Tables 3.5 and 3.6 for all edges simply supported, in Tables 3.7 and 3.8 for the horizontal edges simply supported and skewed edges clamped, and in Tables 3.9 and 3.10 for all edges clamped. The results in Tables 3.5, 3.7 and 3.9 are for Laminate 1 and those in Tables 3.6, 3.8 and 3.10 are for Laminate 2. For simply supported boundary conditions, the VICON results are above any other results since only out-of-plane displacement boundary conditions are imposed along the skewed boundary lines of the semi-infinite plate. For simply supported-clamped and clamped-clamped boundary conditions, the results from the present formulation are in good agreement with VICON since the clamped boundary conditions on the skewed edges can be approximated easily. The STAGS results compare very well with those of the present formulation especially for simply supported-clamped and clamped-clamped boundary conditions.

The sign of the in-plane shear prestress has considerable effect on the buckling coefficient of anisotropic skewed plates. Considering Laminate 1, the percentage decrease of the buckling coefficient for Load Case B from Load Case D is 26.4 percent for $\psi = 30^{\circ}$ and 30.1 percent for $\psi = 45^{\circ}$ for simply supported plates. For simply supported plate made of Laminate 2, the decrease in buckling coefficient for Load Case B from Load Case D is 30.56 and 31.9 percent for $\psi = 30^{\circ}$ and $\psi = 45^{\circ}$, respectively. It is seen that for Laminate 2 the percentage decrease in buckling coefficient for Load Case B from Load Case D for $\psi = 30^{\circ}$ and $\psi = 45^{\circ}$ are close to each other whereas for Laminate 1 the percentage decrease in buckling coefficient of Load Case B from Load case D for $\psi = 30^{\circ}$ and $\psi = 45^{\circ}$ are not close to each other. The buckling coefficients for anisotropic plates with other boundary conditions reflect the same observation. Hence, increasing degree of anisotropy has more effect on the buckling coefficients for positive shear loading conditions.

3.10.4 Effect of Transverse-Shear Deformation

The effect of transverse-shear deformation is studied by considering isotropic and anisotropic skewed plates with different thickness-to-width ratios, t/b, and a fixed plate aspect ratio (a/b) of 1. Clamped and simply supported boundary conditions are considered, and the plates are subjected to Load Case D only. Regular polynomials are used for clamped plates, while Legendre polynomials are used for simply supported plates, since results obtained using Legendre polynomials are in better agreement with STAGS results for simply supported plates.

The present analysis results obtained using up to 11^{th} order polynomial series solution are shown in Table 3.11 for clamped plates and Table 3.12 for simply supported plates. Considering the isotropic clamped plate, the buckling coefficients for $t/b = 0.001$ and 0.01 differ by less than one percent for both skew angles considered. As the plate thickness increases ($t/b = 0.1$), a significant decrease in the value of the buckling coefficients occurs due to shear flexibility. The buckling coefficients for the $t/b = 0.1$ case are reduced by 16 percent and 36 percent compared to the $t/b = 0.01$ case for skew angles of 30° and 45°, respectively. Considering the simply supported plate, the buckling coefficients for $t/b = 0.001$ and 0.01 differ by less than four percent for skew angle of 30° and 45°, respectively. The buckling coefficients for the $t/b = 0.1$ case are reduced by 22 and 27 percent compared to the $t/b = 0.01$ case for skew angles of 30° and 45°, respectively. These results indicate that transverse-shear effects become more important as the plate thickness increases, as the skew angle increases and, as the boundary fixity is relaxed.

For clamped anisotropic plates, the buckling coefficients for plate thickness to width ratio (t/b) = 0.001 and 0.01 differ by less than two percent for both skew angles and both laminates as shown in Table 3.11. As the plate thickness increases further ($t/b = 0.1$), a significant decrease in the value of buckling coefficient occurs.

For both laminates, this decrease is 49 percent and 59 percent compared to the values obtained for the $t/b = 0.01$ case for skew angles of 30° and 45°, respectively. For simply supported anisotropic plates, the buckling coefficients for $t/b = 0.001$ and 0.01 differs by less than 3 percent for skew angle of 30°. However, for skew angle of 45°, the buckling coefficients for $t/b = 0.001$ and 0.01 differ by over twice the difference noted for the 30° skew angle case. The buckling coefficients for $t/b = 0.1$ are reduced by 50 to 54 percent when compared to values for $t/b = 0.01$ and a skew angle of 30° whereas the decrease is 59 percent for skew angle of 45°. These results indicate that for laminated anisotropic plates the buckling coefficient is significantly reduced as the thickness increases. For the 30° case, the change in buckling coefficient for anisotropic plates with $t/b = 0.01$ to $t/b = 0.1$ is nearly three times that for the isotropic plates with the same t/b ratios. As the skew angle increases, the difference in buckling coefficients between the isotropic and the anisotropic plates decreases.

Therefore, the size of the skew angle significantly affects the buckling response of thick skewed plates. The percentage decrease for Laminate 1 and Laminate 2 is more than that for isotropic plate since laminated composites have a lower shear modulus compared to isotropic material.

3.11 BUCKLING OF TRIANGULAR PLATES

Numerical results are presented for buckling of triangular plates with isotropic and anisotropic material properties. Various geometries, combined in-plane loading conditions, and boundary conditions are considered. Some results obtained using the present method are compared with results from existing series solutions. The effect of transverse-shear deformation on the buckling coefficients of triangular plates is also studied.

3.11.1 Isotropic Triangular Plates

The results for isotropic triangular plates are expressed in terms of a non-dimensional buckling coefficient defined as

$$K = \frac{\lambda_{cr} b^2}{\pi^2 D_{22}} \tag{3.47}$$

where λ_{cr} is the critical eigenvalue, b is the height of the triangle, and D_{22} is the transverse plate bending stiffness. The types of triangular plates (see Figure 3.4) and boundary conditions considered are:

1. Simply supported equilateral triangle [34].
2. Right-angled isosceles triangle with simply supported edges [36].
3. Right-angled isosceles triangle with simply supported perpendicular edges and clamped hypotenuse [36].
4. Right-angled isosceles triangle with clamped perpendicular edges and simply supported hypotenuse [36].
5. Simply supported $30^o - 60^o - 90^o$ triangle [38].

The results obtained using the present analysis are shown in Tables 3.13 and Table 3.14 for different in-plane loading conditions. The number of terms used in the polynomials for all these cases is 45 since as shown in Figure 3.6 for the different types of simply supported triangular plates subjected to uniform compression ($\overline{N}_x = \overline{N}_y = 1$), the buckling coefficients converged well before 45 terms. These triangular plates have a thickness-to-height ratio (t/b) of 0.0003, and transverse-shear effects are negligible for these thin isotropic plates. Agreement between results obtained using the present method and existing results is very good.

3.11.2 Simply Supported Anisotropic Triangular Plates

Buckling loads for simply supported anisotropic equilateral triangular plates, right-angled isosceles triangular plates, and $30^o - 60^o - 90^o$ triangular plates are considered in this study. The height of each triangle is 10.0 inches (see Figure 3.4). The load cases considered are:

1. Load Case A: $\overline{N}_x = \overline{N}_y = 1, \overline{N}_{xy} = -0.5$
2. Load Case B: $\overline{N}_x = \overline{N}_y = 1, \overline{N}_{xy} = 0.0$
3. Load Case C: $\overline{N}_x = \overline{N}_y = 1, \overline{N}_{xy} = 0.5$

The laminate stacking sequences considered herein are the same as the two considered for the anisotropic quadrilateral plates described in Section 3.10.3. Laminates 1 and 2 have ply stacking sequences of $[\pm 45/90/0]_s$ and $[45/90/-45]_s$ with 0.005-inch-thick and 0.007-inch-thick plies, respectively. The nominal ply mechanical properties used are: $E_{11} = 24.5$ Msi; $E_{22} = 1.64$ Msi; $G_{12} = G_{13} = G_{23} = 0.87$ Msi and $\nu_{12} = 0.3$ and Laminate 2 being more anisotropic than Laminate 1 as discussed in the Section 3.10.3. Converged results are obtained using 36 terms (complete eighth-order polynomials in two variables) for each displacement component are shown in Table 3.15.

For the right-angled isosceles triangular plate and the $30^o - 60^o - 90^o$ triangular plate, made of Laminate 1, the buckling loads for Load Case C are approximately 1.4 times the buckling loads for Load Case A. For the equilateral triangular plate, the buckling load for Load Case C is approximately 1.1 times the buckling load for Load Case A. For the right-angled isosceles triangular plate and the $30^o - 60^o - 90^o$ triangular plate made of Laminate 2, the buckling loads for Load Case C are approximately 1.6 times the buckling loads for Load Case A. For the equilateral triangular plate, the buckling load for Load Case C is approximately 1.3 times the buckling load for Load Case A. These results indicate that the buckling load is significantly influenced by the symmetry of the triangular plate geometry and material anisotropy when the

shear load direction is reversed. The equilateral triangle has three lines of symmetry, the right-angled isosceles triangle has one line of symmetry and the $30° - 60° - 90°$ triangle has no lines of symmetry. The differences between buckling loads obtained using FSDT from those obtained using CLPT are small.

3.11.3 Effect of Transverse-Shear Deformation

The effect of transverse-shear deformation is studied by considering simply supported triangular plates with isot ratio, t/b. The triangular plates are subjected to uniform compression ($N_x = N_y = 1$). The results for right-angled isosceles and equilateral triangular plates are shown in Table 3.16 and are expressed in terms of a non-dimensional buckling coefficient as defined by equation (3.47). The number of terms used for each displacement component is 45, which corresponds to a complete ninth-order polynomial in two variables.

For both the isotropic triangular plates and anisotropic triangular plates made of Laminates 1 and 2, the effect of transverse-shear deformation had no significant effect on the buckling coefficient results when the t/b ratio is increased from 0.001 to 0.01. When the t/b ratio is increased from 0.01 to 0.1 for the isotropic triangular plates, the buckling coefficient reduces by 18 percent for the right-angled isosceles triangle and 15 percent for the equilateral triangle. The corresponding reduction in buckling coefficients for Laminate 1 are 42 percent for the right-angled isosceles triangle and 38 percent for the equilateral triangle. For right-angled triangular and equilateral triangular plates made of Laminate 2, the reduction is approximately the same at 35 percent. For typical grid-stiffened composite fuselage structure designs, the t/b ratio for triangular plates is greater than 0.025 and, hence transverse-shear effects need to be included in the analysis.

3.12 NUMERICAL RESULTS FOR CURVED PANELS

Numerical results are presented for anisotropic curved panels with length of 60.0 in., arc length of 18.85 in., and a radius of 6.0 in., subjected to axial compression as shown in Figure 3.7. The panel is simply supported on all edges since the bending rotations are not constrained on any edge. The other geometric boundary conditions are shown in Figure 3.7. The nominal mechanical properties are $E_{11} = 13.75$ Msi, $E_{22} = 1.03$ Msi, $G_{12} = G_{13} = G_{23} = 0.42$ Msi and $\nu_{12} = 0.25$. The thickness of the 10-ply panel is 0.12 in. The laminate stacking sequence is $[\pm\theta/\pm\theta/\theta]_s$ with $0° \leq \theta \leq 90°$ which is the winding angle. Each ply is of the same thickness.

The critical buckling load for this curved panel is computed using Sanders-Koiter shell theory, Love's shell theory, and Donnell's shell theory through the "tracer" coefficients discussed in Section 3.2. This problem ([65]) displays significant difference in critical load between Sanders-Koiter shell theory and Donnell's shell theory, depending on the winding angle θ. This problem was proposed by Professor Isaac Elishakoff and communicated by Dr. David Bushnell. The buckling loads for the curved panel using Sanders-Koiter shell theory, Love's shell theory, and Donnell's shell theory are shown in Figure 3.8 for various values of θ. The buckling loads were obtained using Ritz function consisting of Legendre polynomials up to 11^{th} order. For the case $\theta = 90°$, Legendre polynomials up to 19^{th} order was used. These buckling loads are also compared with results obtained using the STAGS finite element code ([29]), where a mesh of 30×30 elements (480 Element) is used. The 480 Element accounts for transverse shear flexibilities. The curved panel is modeled as an assembly of flat elements in STAGS and hence the results obtained using STAGS are independent of any shell theory.

The results obtained using Love's shell theory are very close to that obtained using Sanders-Koiter shell theory. The STAGS finite element results are also in

good agreement with those obtained using Love's and Sanders-Koiter shell theory. The results obtained using the Donnell's shell theory are close to results obtained by Love's and Sanders-Koiter shell theory for θ between 0^o and about 15^o. For $\theta > 15^o$, Donnell's shell theory overestimates the buckling loads when compared to Sanders-Koiter or Love's shell theory. The difference in buckling loads between those obtained by Sanders-Koiter and Donnell's theory is largest for $50^o \leq \theta \leq 70^o$. After $\theta = 70^o$, the difference between the buckling loads obtained by Sanders-Koiter and Donnell decreases, and at $\theta = 90^o$ the loads obtained using Donnell's and Sanders-Koiter shell theory are close to each other. According to Ref. [12], Donnell's theory give accurate results for cylindrical panels that are relatively flat before deformation and for complete cylindrical shells whose displacement components in the deformed configuration are rapidly varying functions of the circumferential coordinate. Such shells are sometimes termed quasi-shallow. Figure 3.9 shows the buckling mode shapes obtained from STAGS for various values of θ. For $\theta = 0^o$ and and 90^o, there are more than two half-waves in the curved direction. Hence, the buckling loads obtained by Donnell's theory is in good agreement with the other results. For $\theta = 10^o$, there are still more than two half-waves on part of the panel and therefore, the result from Donnell's theory is still in agreement with the other results. For $\theta = 20^o$ and 30^o, there is only one half-wave in the curved direction, and for $\theta = 40^o$, 50^o, 60^o and 70^o, there are no half-wave in the curved direction on part of the panel, therefore for these values of θ, the results obtained by Donnell's theory are not in good agreement with the other results. For $\theta = 80^o$, the deformation pattern is more in a skewed direction rather than along the curved direction, therefore the result obtained by Donnell's theory is not in agreement with the other results.

Buckling loads for $\theta = 70^o$ for different radius to thickness ratio R/t are shown in Table 3.17. Buckling loads for an isotropic case with nominal mechanical properties of $E_{11} = 10.0$ Msi and $\nu_{12} = 0.30$ for different R/t are also shown.

For $R/t = 25$, the percentage difference between the result of Donnell's theory and Sanders-Koiter theory is approximately 23 % for both cases. For the $[\pm 70/\pm 70/70]_s$ laminate, the difference between the result of Sanders-Koiter theory and Donnell's theory is approximately 20 % for $R/t = 50$ and 100. For $R/t = 200$ and 600, the difference is 8.3 % and 4.8 %, respectively. For the isotropic curved panel, the difference between the result of Sanders-Koiter theory and Donnell's theory approximately 11 % for $R/t = 50$ and less than 5 % for the other R/t ratios. Since, the results of the isotropic case also show differences between results of different shell theories moderate R/t ratios, it is concluded that such discrepancy between various shell theories is not mainly due to anisotropy, but rather to the geometry of the problem. Figure 3.10 shows the contour plots of the mode shape of the radial displacement (w) obtained from the Rayleigh-Ritz buckling analysis using Sanders-Koiter theory. for the $[\pm 70/\pm 70/70]_s$ laminate for different R/t ratio. It is seen that only the mode shape for $R/t = 600$ has more than two half-waves in the curved directions, hence, the results of Donnell's theory and Sanders-Koiter are close to each other.

3.13 SUMMARY

A Rayleigh-Ritz method combined with a variational formulation and a first-order, transverse-shear-deformation theory and various shell theories has been presented for buckling of arbitrary quadrilateral panels and general triangular panels with various boundary conditions and subjected to combined inplane loading. The Ritz functions consist of polynomials which include "circulation" functions to impose various boundary conditions. Numerical results are obtained for isotropic, orthotropic and anisotropic plates with skewed geometries, triangular geometries, and curved panels. The present analysis method does not exhibit any mesh distortion sensitivity, accurately models parallelogram-shaped geometries, and general triangular geometries, accounts for material anisotropy, and can accommodate combined loading conditions. It also accounts for different shell theories.

For the skew plates, the sensitivity of the buckling coefficient to the direction of the in-plane shear prestress application is studied for increasing skew angles. The influence of the skew angle on the buckling coefficient is more pronounced as the skew angle increases for thin plates as well as thick plates. The results also suggest that material anisotropy accentuates this effect. For the analysis cases studied here, the present formulation provides accurate buckling results for skewed isotropic and anisotropic plates which will be useful in the preliminary design of stiffened structures.

The direction of the in-plane shear load is studied for different triangular geometries and degrees of material anisotropies. The symmetry of the triangular plate geometry seems to influence the buckling load more than the degree of material anisotropy for the cases considered in this study. The effect of transverse-shear deformation is studied for different triangular geometries which confirms the importance of including these effects in the buckling analysis of composite plates.

Accurate buckling load results for isotropic and anisotropic triangular plates and will be useful in the preliminary design of grid-stiffened structures.

Buckling loads for curved panels subjected to axial compression are obtained using Sanders-Koiter, Love's, and Donnell's shell theory. There are significant difference between buckling loads obtained using Sanders-Koiter or Love's shell theory and Donnell's shell theory for the curved panel and material considered. Results show that Donnell' theory is in close agreement with other theories for large radius to thickness ratio or for very thin shell and also when displacements in the deformed configuration vary rapidly with the circumferential coordinate.

Table 3.1 Buckling coefficient, K, for simply supported isotropic plates, $a/b = 1$.

	$\psi = 0°$	$\psi = 15°$	$\psi = 30°$	$\psi = 45°$
Mizuswa, et al. [61]	4.000	3.778	3.160	2.160
Wang et al. [31]	4.000	3.860	3.480	2.650
Kitipornchai, et al. [58]	4.000	3.825	3.331	2.526
VICON	4.000	4.126	4.250	3.387
STAGS	4.003	3.825	3.288	2.426
Present analysis:				
Regular polynomial	3.999	3.832	3.380	2.709*
Legendre polynomial	3.999	3.825	3.320	2.536

*Using 91 terms, Present analysis gives 2.630

Table 3.2 Buckling coefficient, K, for clamped isotropic plates, $a/b = 1$.

	$\psi = 0°$	$\psi = 15°$	$\psi = 30°$	$\psi = 45°$
Wittrick [56]	10.080	-	7.670	5.410
Durvasula [57]	10.080	9.462	7.639	5.110
Wang et al. [31]	10.080	9.479	7.734	5.170
Kitipornchai, et al. [58]	10.080	9.431	7.615	5.028
VICON	10.081	9.445	7.639	5.025
STAGS	10.081	9.416	7.579	4.980
Present analysis:				
Regular polynomial	10.073	9.432	7.621	5.154*
Legendre polynomial	10.073	9.431	7.615	5.026

*Using 91 terms, Present analysis gives 5.051

Table 3.3 Buckling coefficient, K, for simply supported skewed plates, $a/b = 1$, $D_{11}/D_{22} = 1$.

	Kennedy et al. [62]	VICON	STAGS	Present Analysis	
				Regular polynomial	Legendre polynomial
Load Case			$\psi = 15°$		
A	-	4.739	4.770	4.773	4.768
B	2.150	2.186	2.114	2.116	2.114
C	2.340	2.435	2.296	2.298	2.296
D	2.490	2.707	2.452	2.454	2.451
			$\psi = 30°$		
A	-	7.555	6.217	6.356	6.282
B	2.300	2.775	2.340	2.383	2.363
C	2.640	3.333	2.677	2.730	2.704
D	3.020	4.009	3.054	3.121	3.086
			$\psi = 45°$		
A	-	13.548	10.108	11.043	10.582
B	2.900	4.412	3.119	3.342	3.239
C	3.380	5.368	3.656	3.938	3.805
D	4.000	6.732	4.334	4.697	4.519

Table 3.4 Buckling coefficient, K, for simply supported skewed plates, $a/b = 1$, $D_{11}/D_{22} = 5$.

	Kennedy et al. [62]	VICON	STAGS	Present Analysis	
				Regular polynomial	Legendre polynomial
Load Case			$\psi = 15°$		
A	-	9.295	9.122	9.131	9.129
B	3.869	3.875	3.883	3.888	3.887
C	4.290	4.353	4.319	4.324	4.323
D	4.730	4.922	4.759	4.763	4.762
			$\psi = 30°$		
A	-	13.750	11.601	11.700	11.669
B	3.810	4.317	3.930	3.962	3.955
C	4.480	5.220	4.654	4.693	4.684
D	5.440	6.550	5.613	5.661	5.647
			$\psi = 45°$		
A	-	25.170	18.606	19.269	18.986
B	4.350	5.440	4.649	4.787	4.739
C	5.260	6.740	5.626	5.802	5.738
D	6.500	8.800	7.060	7.296	7.204

Table 3.5 Buckling coefficient, K, for simply supported anisotropic skewed plates, $[\pm 45/90/0]_s$ laminate.

Load Case	VICON	STAGS	Present Analysis	
			Regular polynomial	Legendre polynomial
		$\psi = 30°$		
B	2.725	2.373	2.396	2.382
C	3.269	2.758	2.787	2.767
D	4.017	3.227	3.264	3.237
		$\psi = 45°$		
B	4.153	3.001	3.155	3.068
C	5.070	3.553	3.749	3.635
D	6.415	4.286	4.545	4.390

Table 3.6 Buckling coefficient, K, for simply supported anisotropic skewed plates, $[45/90/-45]_s$ laminate.

Load Case	VICON	STAGS	Present Analysis	
			Regular polynomial	Legendre polynomial
		$\psi = 30°$		
B	1.552	1.484	1.488	1.486
C	1.870	1.764	1.769	1.766
D	2.321	2.139	2.144	2.140
		$\psi = 45°$		
B	2.510	2.023	2.106	2.061
C	3.040	2.419	2.523	2.465
D	3.800	2.969	3.105	3.027

Table 3.7 Buckling coefficient, K, for simply supported-clamped anisotropic skewed plates, $[\pm 45/90/0]_s$ laminate.

Load Case	VICON	STAGS	Present Analysis	
			Regular polynomial	Legendre polynomial
		$\psi = 30°$		
B	4.170	4.130	4.158	4.155
C	4.901	4.850	4.884	4.878
D	5.718	5.644	5.685	5.675
		$\psi = 45°$		
B	5.791	5.722	5.849	5.812
C	6.990	6.917	7.085	7.025
D	8.512	8.455	8.688	8.588

Table 3.8 Buckling coefficient, K, for simply supported-clamped anisotropic skewed plates, $[45/90/-45]_s$ laminate.

Load Case	VICON	STAGS	Present Analysis	
			Regular polynomial	Legendre polynomial
		$\psi = 30°$		
B	1.976	1.967	1.973	1.972
C	2.388	2.374	2.381	2.380
D	2.942	2.915	2.923	2.921
		$\psi = 45°$		
B	2.857	2.832	2.872	2.855
C	3.480	3.450	3.505	3.477
D	4.360	4.327	4.407	4.359

Table 3.9 Buckling coefficient, K, for clamped anisotropic skewed plates, $[\pm 45/90/0]_s$ laminate.

Load Case	VICON	STAGS	Present Analysis	
			Regular polynomial	Legendre polynomial
		$\psi = 30°$		
B	6.134	6.090	6.126	6.125
C	7.043	6.988	7.019	7.019
D	7.717	7.657	7.680	7.677
		$\psi = 45°$		
B	8.743	8.629	8.737	8.731
C	10.154	10.008	10.121	10.102
D	11.273	11.212	11.302	11.243

Table 3.10 Buckling coefficient, K, for clamped anisotropic skewed plates, $[\pm 45/90/0]_s$ laminate.

Load Case	VICON	STAGS	Present Analysis	
			Regular polynomial	Legendre polynomial
		$\psi = 30°$		
B	3.783	3.765	3.784	3.782
C	4.590	4.576	4.589	4.588
D	5.453	5.436	5.440	5.439
		$\psi = 45°$		
B	5.617	5.478	5.602	5.592
C	6.850	6.807	6.850	6.848
D	8.107	8.083	8.106	8.087

Table 3.11 Buckling coefficient, K, for clamped skewed plates with different thickness-to-width ratio.

	Regular polynomial		
	Isotropic	Laminate 1	Laminate 2
t/b		$\psi = 30°$	
0.001	7.138	7.680	5.440
0.010	7.117	7.596	5.382
0.100	5.970	3.868	2.727
		$\psi = 45°$	
0.001	10.601	11.302	8.106
0.010	10.525	11.106	7.972
0.100	6.719	4.636	3.299

Table 3.12 Buckling coefficient, K, for simply supported skewed plates with different thickness-to-width ratio.

	Legendre polynomial		
	Isotropic	Laminate 1	Laminate 2
t/b		$\psi = 30°$	
0.001	2.904	3.245	2.739
0.010	2.872	3.153	2.690
0.100	2.350	2.041	1.793
		$\psi = 45°$	
0.001	4.368	4.436	3.903
0.010	4.209	4.170	3.721
0.100	3.305	2.621	2.333

Table 3.13 Buckling coefficient, K, for simply supported triangular isotropic plates.

Triangle Geometry	Loading	Buckling Coefficient		
		Ref. [34] (CLPT)	Present (CLPT)	Present (FSDT)
Equilateral triangle	$N_x = N_y = 1$, $N_{xy} = 0$	4.0000	4.0038	4.0038
		Buckling Coefficient		
		Ref. [36] (CLPT)	Present (CLPT)	Present (FSDT)
Right-Angled isosceles triangle	$N_x = N_y = 0$, $N_{xy} = -1$	11.5500	11.5580	11.5580
	$N_x = N_y = 1$, $N_{xy} = 0$	5.0000	5.0051	5.0051
	$N_x = N_y = 6.29$, $N_{xy} = 11.57$	1.0000	0.9984	0.9984
		Buckling Coefficient		
		Ref. [38] (CLPT)	Present (CLPT)	Present (FSDT)
$30° - 60° - 90°$ triangle	$N_x = N_y = 1$, $N_{xy} = 0$	9.3300	9.3370	9.3370

Table 3.14 Buckling coefficient, K, for right-angled isosceles triangular plates with different boundary conditions.

Boundary condition	Loading	Buckling Coefficient		
		Ref. [36] (CLPT)	Present (CLPT)	Present (FSDT)
Perpendicular edges simply supported Hypotenuse clamped	$N_x = N_y = 0$ $N_{xy} = -1$	22.0200	21.9500	21.9500
	$N_x = N_y = 1$ $N_{xy} = 0$	7.8200	7.8171	7.8171
	$N_x = N_y = 8.23$ $N_{xy} = 12.34$	1.0000	0.9898	0.9898
Perpendicular edges clamped Hypotenuse simply supported	$N_x = N_y = 0$ $N_{xy} = -1$	17.1200	16.9390	16.9390
	$N_x = N_y = 1$ $N_{xy} = 0$	9.3500	9.3420	9.3420
	$N_x = N_y = 10.9$ $N_{xy} = 12.34$	1.0000	1.0001	1.0001

Table 3.15 Buckling load results for simply supported triangular anisotropic plates.

Triangle Geometry	Load Case	Laminate 1 $N_{cr}(lbs/in)$ (FSDT)	Laminate 1 $N_{cr}(lbs/in)$ (CLPT)	Laminate 2 $N_{cr}(lbs/in)$ (FSDT)	Laminate 2 $N_{cr}(lbs/in)$ (CLPT)
$30° - 60° - 90°$ Triangle	A	39.035	39.135	26.795	26.885
	B	45.850	45.999	33.192	33.306
	C	53.960	54.108	42.3444	42.495
Right-Angled Isosceles Triangle	A	21.464	21.515	15.574	15.597
	B	25.578	25.642	19.547	19.577
	C	30.567	30.635	25.328	25.372
Equilateral Triangle	A	23.702	23.752	20.780	20.789
	B	25.140	25.197	23.626	23.629
	C	25.746	25.804	26.311	26.354

Table 3.16 Buckling coefficient, K, for simply supported triangular plates with different thickness to height ratios (t/b).

	Right-Angled Isosceles Triangle			Equilateral Triangle		
t/b	0.001	0.010	0.100	0.001	0.010	0.100
Isotropic	4.9998	4.9813	4.1014	3.9999	3.9885	3.3864
Laminate 1	5.1528	5.0670	2.9445	4.2697	4.2179	2.6340
Laminate 2	2.6575	2.6311	1.7220	2.6517	2.6263	1.7194

Table 3.17 Buckling loads for curved panel with different R/t ratio.

	t (in.)	R/t	λ_{s-k} (lbs/in.)	λ_{love} (lbs/in.)	λ_{don} (lbs/in.)	$\frac{(\lambda_{s-k}-\lambda_{don})}{\lambda_{don}}$
$[\pm 70/\pm 70/70]_s$	10 × 0.024	25	1.21e4	1.22e4	1.6e4	-23.7%
	10 × 0.012	50	3417.1	3432.0	4303.1	-20.5%
	10 × 0.006	100	920.6	922.2	1163.6	-20.8%
	10 × 0.003	200	264.1	264.2	288.7	-8.3%
	10 × 0.001	600	32.83	32.86	34.50	-4.8%
$\lambda_{stags} = 3349.1$ for $R/t = 50$						
ISOTROPIC	0.24	25	4.24e4	4.27e4	5.51e4	-22.98%
	0.12	50	1.22e4	1.24e4	1.39e4	-11.61%
	0.06	100	3527.9	3533.6	3663.0	-3.70%
	0.03	200	916.5	917.4	964.6	-4.97%
	0.01	600	113.6	113.6	116.9	-2.75%
$\lambda_{stags} = 1.236$e4 for $R/t = 50$						

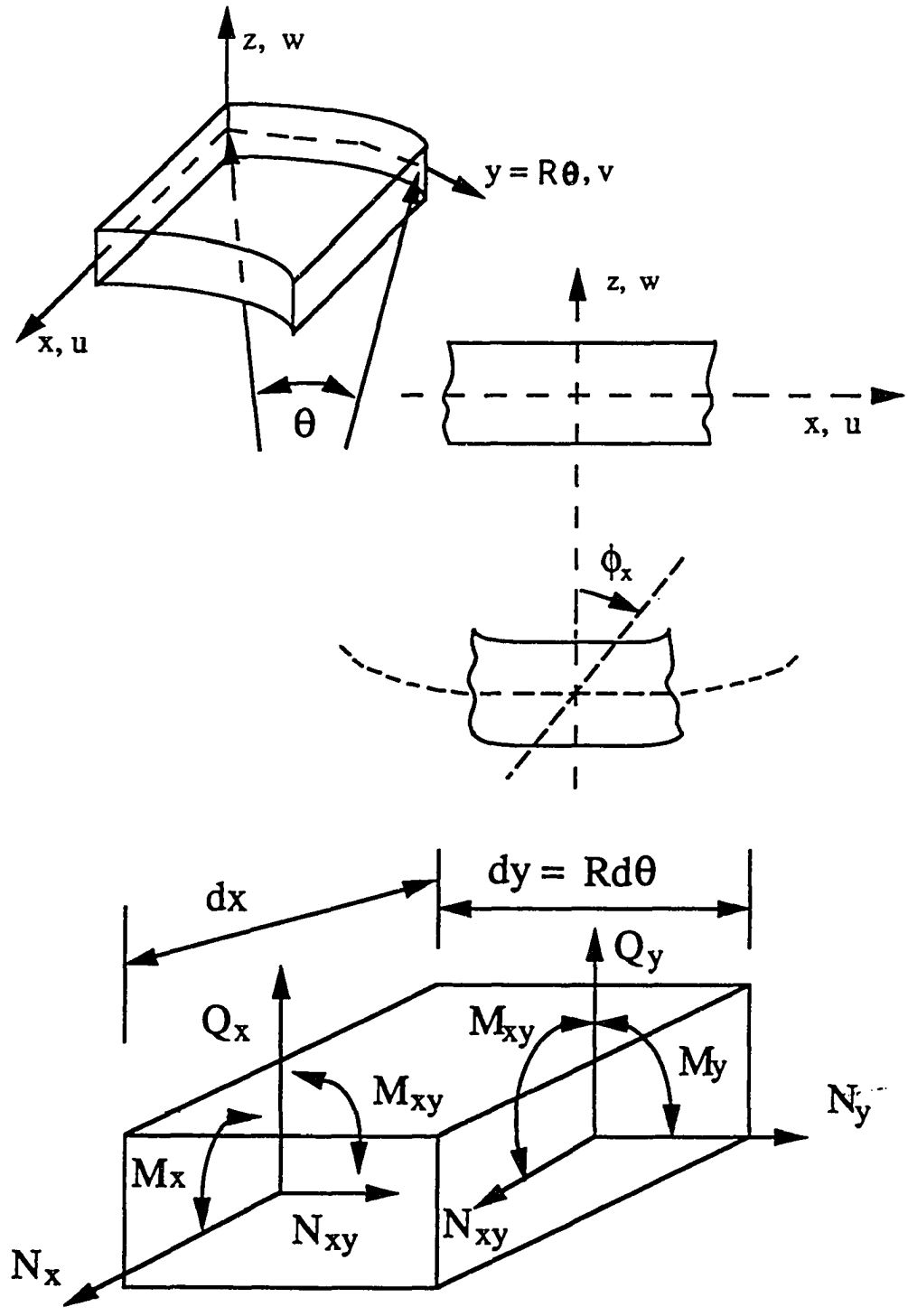

Figure 3.1 Sign convention for cylindrical shell element.

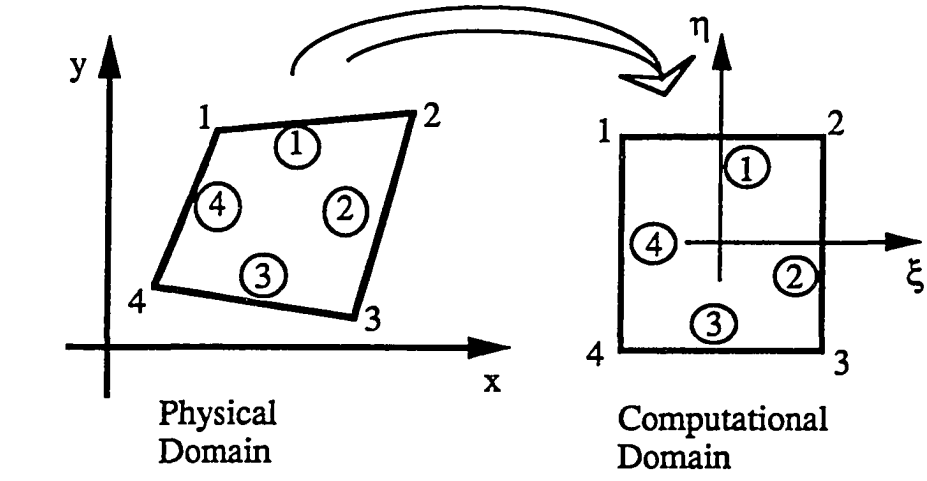

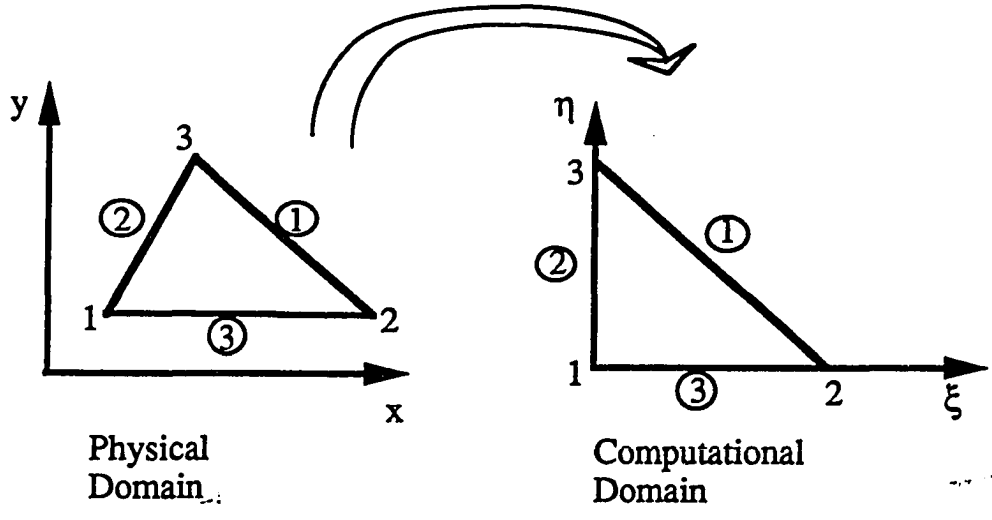

Figure 3.2 Transformation from physical to computational domain.

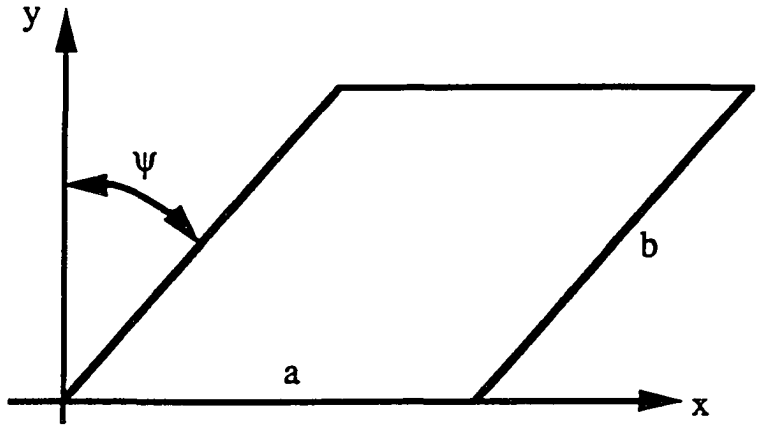

Figure 3.3 Skewed plate geometry.

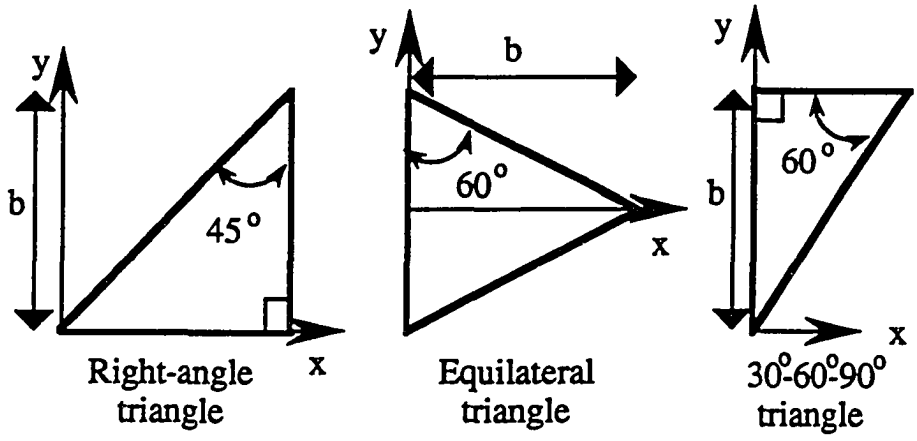

Figure 3.4 Triangular plate geometries.

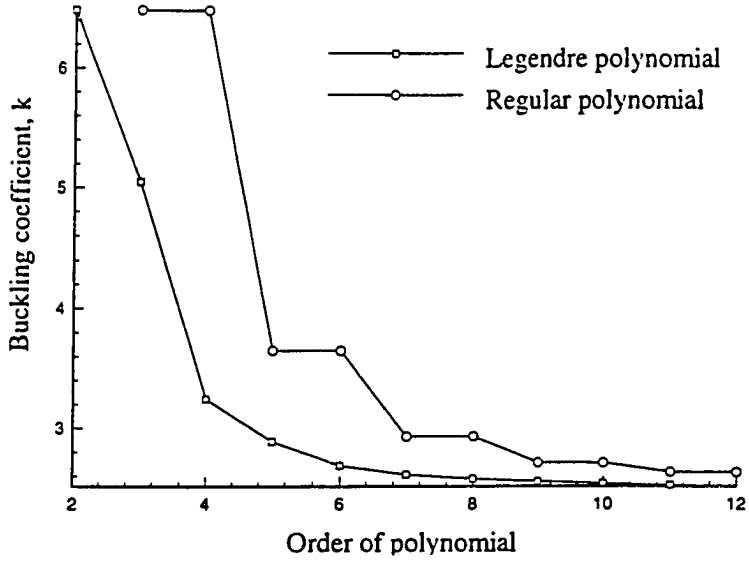

Fig. 3.5 Convergence of buckling coefficient with increasing order of polynomial for simply supported, isotropic, 45° skew plate subjected to axial compression.

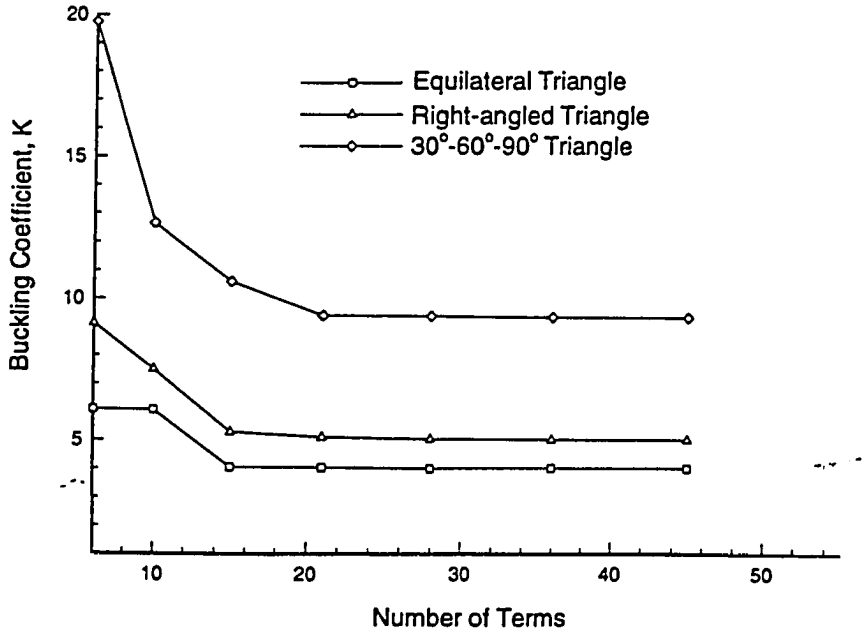

Fig. 3.6 Convergence of buckling coefficient with number of terms used in Ritz function for different simply supported isotropic triangular plates subjected to compression ($N_x = N_y = 1$).

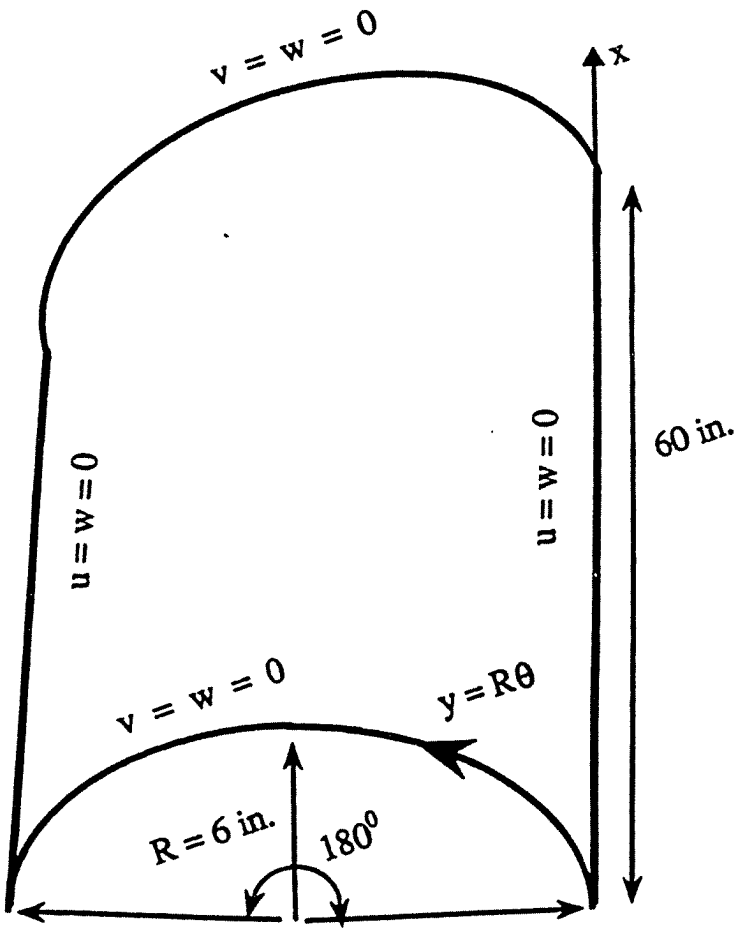

Figure 3.7 Curved panel geometry and boundary conditions.

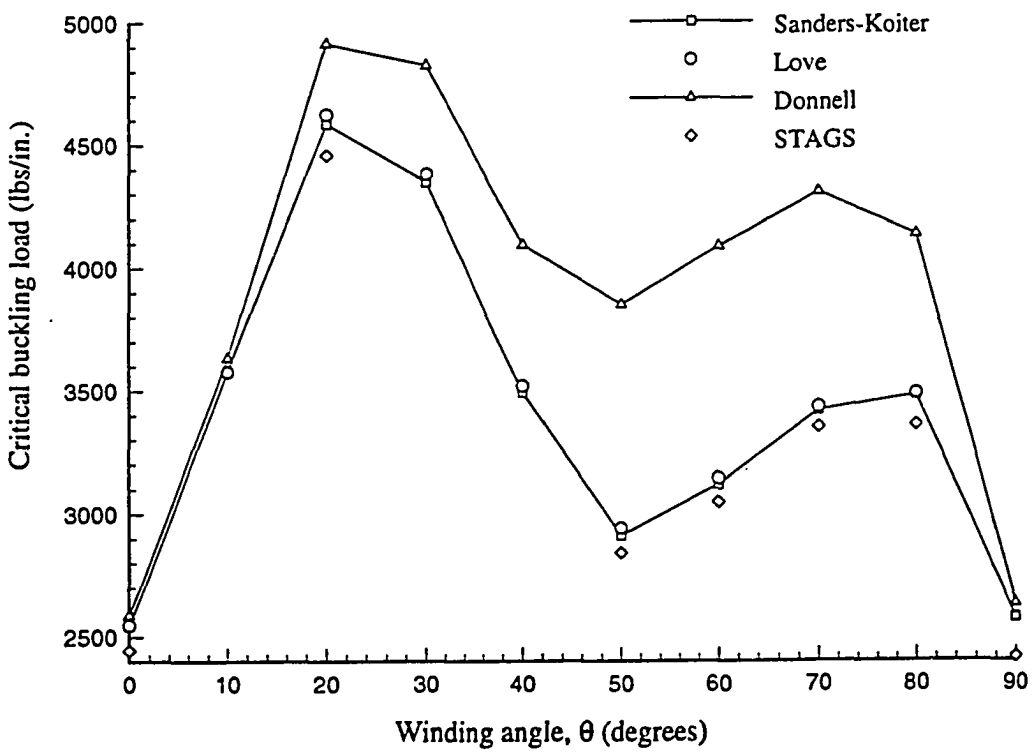

Fig. 3.8 Comparisons of buckling loads for curved panel from different theories.

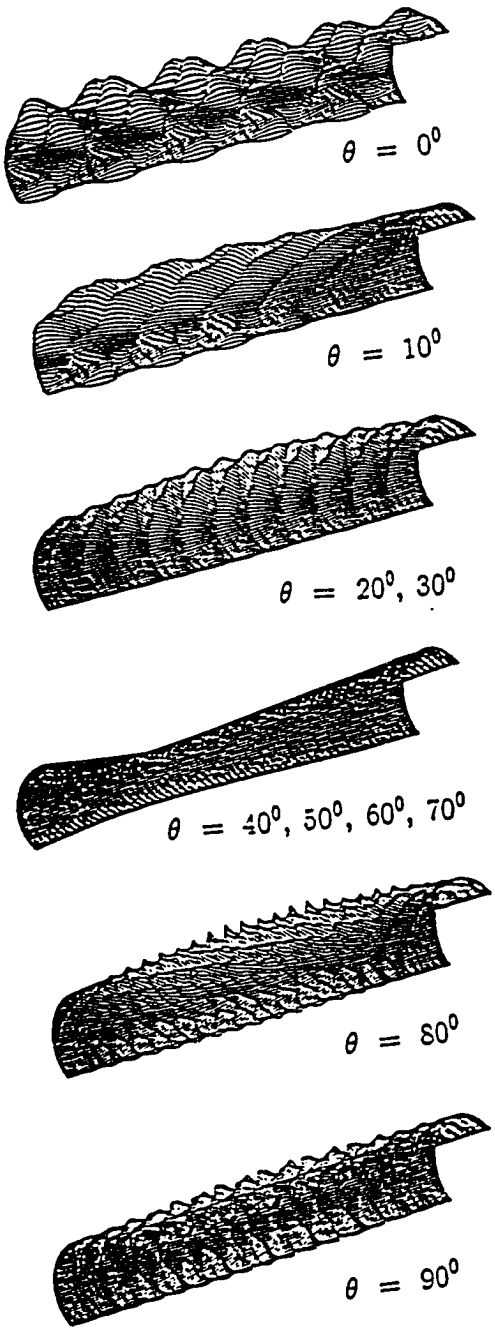

Fig. 3.9 Buckling mode shape of curved panel for different winding angle θ.

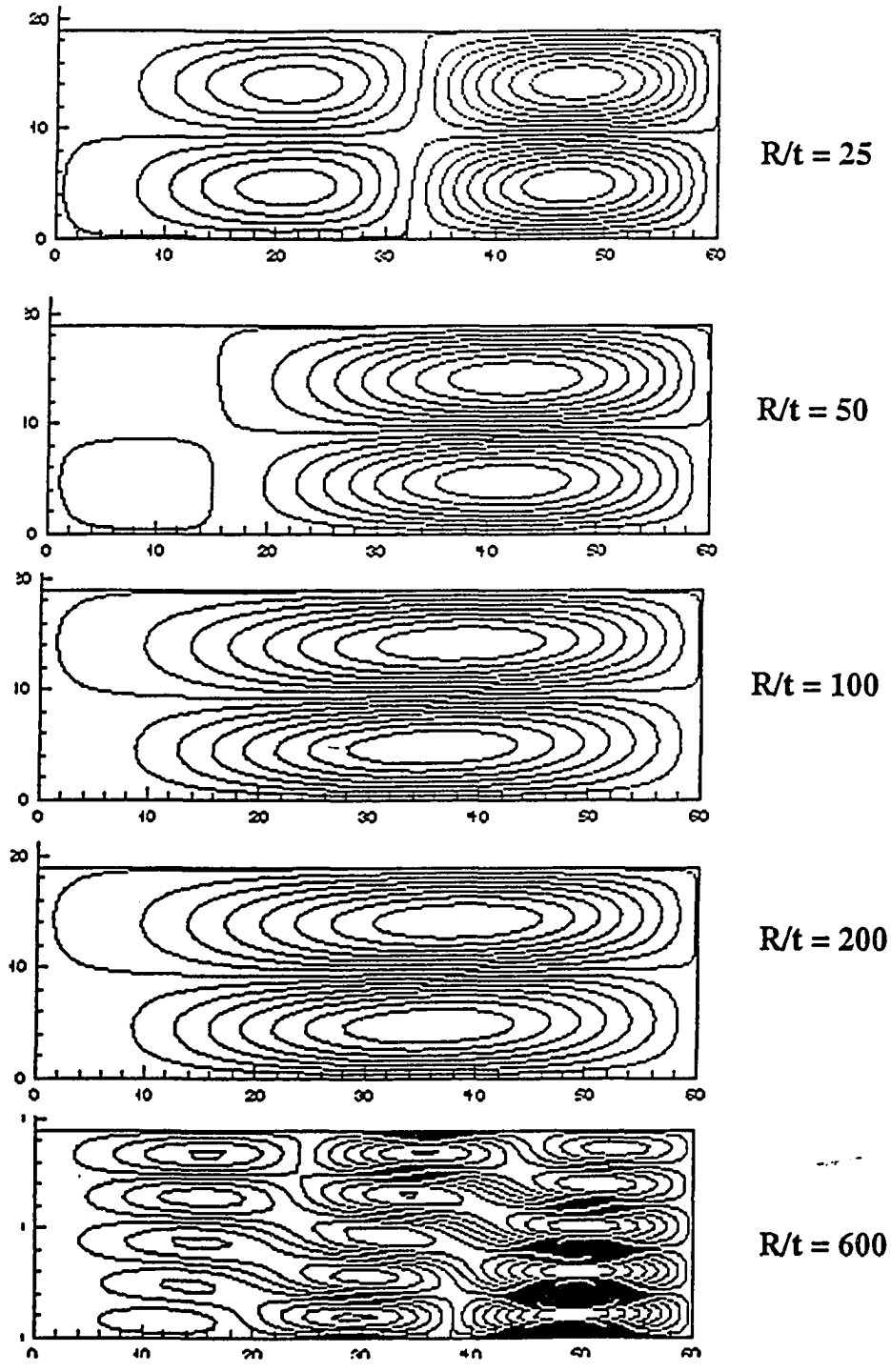

Figure 3.10 Mode shape for $[70/-70/70/-70/70]_s$ laminate with different R/t ratios.

Chapter 4

OPTIMAL DESIGN OF GRID-STIFFENED COMPOSITE PANELS USING GLOBAL AND LOCAL BUCKLING ANALYSES

An aircraft in flight is subjected to air loads which are imposed by maneuver and gust conditions. These external loads are resisted by the structure, and an internal load distribution is established based on the structural layout and given external loads. These internal loads, which depend on the location of the panel in the aircraft structure, may result in either overall panel buckling, buckling of the skin between stiffeners, or stiffener crippling. Hence, an efficient and accurate method for developing a buckle-resistant design of general grid-stiffened panels subjected to combined in-plane loading conditions is needed in order to identify the most effective grid-stiffened geometries for structural panels for different locations in fuselage and wing structures. The identification of effective grid-stiffened geometries also requires optimization techniques in addition to accurate structural analyses. Thus, optimization of composite structures has drawn considerable attention in the recent years. Composite plates have been optimized to maximize buckling loads as presented in the literature survey of Reference [66]. According to Reference [66], the basic design

problem is to determine the stacking sequence of the composite laminate since in many practical applications the ply orientations are limited to either 0^o, 90^o or $\pm 45^o$ and, the laminate thicknesses can only be integer multiples of commercially available ply thicknesses. Thus, the optimization of a laminate stacking sequence involved discrete design variables due to manufacturing constraints and represent an integer programming problem.

Design optimization of stiffened panels for buckling has also drawn attention in recent years (e.g., [7]-[9], [22], [66], [67]). These researchers did not consider the stiffener spacings as design variables even though the skin thickness, stiffener thickness and stiffener height were design variables. For the most part, gradient-based optimizers were used in References [9], [7], [22] and [67]. However in Reference [8], the ranking method was used as the optimizer, while in Reference [66], the genetic algorithm, [25], was used to optimize the laminate stacking sequence in the skin and stiffener. Geodesically stiffened panels were considered in References [22] and [7], while orthogrid panels were considered in Reference [8] and axially stiffened panels were considered in References [67] and [66]. The optimization of grid-stiffened panels with stiffener spacings and stiffener layout as discrete design variables pose the same problems as that of optimizing the laminate stacking sequence discussed in Reference [66]. Since stiffener spacings are discrete variables, the optimum grid-stiffened geometry may contain any combination of axial, transverse and diagonal stiffeners, and the stiffener and skin thicknesses can only be integer multiples of commercially available ply thicknesses. The genetic algorithm has emerged as a viable tool for dealing both with the problem of discrete variables and with the need to find multiple minima. The genetic algorithm evolves the design by randomly searching the design space and maintaining a family of design for each generation (or iteration). This process provides multiple near-optimum designs for evaluation and selection rather than a single-design configuration provided by gradient-based algorithms.

This chapter presents the analysis strategy and design strategy for designing grid-stiffened composite panels subjected to combined loads and a global buckling design constraint. The global buckling constraint of the grid-stiffened panel is important so as to prevent localized skin buckling. This constraint reduces the risk of failure of the panel by stiffener-skin separation (e.g., Reference [68]) and also avoids perturbing the aerodynamic performance caused by skin buckling of the wing or fuselage surfaces.

4.1 PANEL BUCKLING ANALYSIS

The analysis and design of grid-stiffened composite panels subjected to combined loads require several key steps. In the present study, acceptable designs are those which buckle globally and do not exhibit any local skin buckling or stiffener crippling. The first step is to assess the global buckling response of the grid-stiffened panel. Once this global buckling response is determined, the second step is to determine the local skin buckling response for general the quadrilateral and/or triangular skin segments that occur locally between stiffeners. The third step is to determine whether stiffener buckling or stiffener crippling has occurred at this global load level. This sequence of steps is performed repeatedly in a design cycle until an optimum or near-optimum design is obtained.

The global buckling analysis is based on a Rayleigh-Ritz method using a first-order, shear-deformation theory and an improved smeared-stiffener modeling approach as discussed in Chapter 3 and 2, respectively. The buckling analysis of local skin-segments is also based on a Rayleigh-Ritz analysis using a first-order, shear-deformation theory and accounts for material anisotropy. Boundary restraints on the skin segments are provided by the stiffeners, and hence, the analysis must be able to accommodate a variety of boundary conditions and a variety of skin segment shapes. In most cases, the shape of the skin segments for grid-stiffened panels will be either

a general quadrilateral or a triangle. Analysis procedures presented in Chapter 3 are used for the local buckling analyses.

In addition to analyzing the local skin segment for buckling, the local stiffener segments must be analyzed to determine whether stiffener crippling will occur. Reference [9] provides a method for determining the buckling load of a stiffener segment. Accordingly, the stiffener segment at the nodes or intersection point of stiffeners are assumed to be clamped while the stiffener-skin attachment is assumed to be simple support. From Ref. [9], the crippling load of the stiffener is N_{crip} and is given by

$$N_{crip} = \frac{\bar{s}_z}{2}\left[\sqrt{1+\frac{4N_{cl}}{\bar{s}_z}}-1\right]$$

where

$$N_{cl} = t_s^3\left[\frac{4\pi^2 E_{11}}{12L_1^2[1-(\nu_{12}^2 E_{22}/E_{11})]}+\frac{G_{12}}{h^2}\right] \tag{4.1}$$

where $\bar{s}_z = \frac{5}{6}G_{13}t_s$, is a shear correction factor, $L_1 = 2L$ is the length of the stiffener, h is the width of the stiffener, and t_s is the thickness of the stiffener.

These global and local analysis methods have been integrated into a computer code to provide a computationally efficient tool for predicting the buckling load of a grid-stiffened composite panel.

4.2 PANEL DESIGN PROCEDURE

The design of grid-stiffened composite panels requires that many of the design variables, such as stiffener spacing and stiffener thicknesses may only take on certain discrete values rather than vary continuously over the design space, and often a "family" of good designs is needed rather than a single-point design due to manufacturing requirements. Gradient-based methods for structural optimization are not appropriate in this case.

Over the last several years, researchers have investigated the use of genetic algorithm as a method for "evolving" a given design problem to a family of near-optimum designs (e.g., see Reference [25], [66] and [69]). Based on Darwin's theory of survival-of-the-fittest, the genetic algorithm involves the random creation of a design population that "evolves" towards some definition of fitness. The genetic algorithm is attractive due to their simplicity of approach in discrete variable combinatorics. The genetic algorithm can be used directly to solve unconstrained optimization problems, while constrained optimization must first be transformed to an unconstrained optimization problem (e.g., use of an exterior penalty function). Stochastic processes are used to generate an initial population of individual designs and the process then applies principles of natural selection and survival of the fittest to find improved designs. Furthermore, since the discrete design procedure works with a population of designs it can explore a large area of design space and climb different hills. This is a major advantage as the converged solution contains many optima of comparable performance. The cost of having a large number of function evaluations is offset by the fact that a large number of optima solutions are now available. In a gradient-based optimization procedure, only a single-point design, usually the extremum to the starting point, is obtained. However, different starting points can be tried to increase the chance of locating the global optimum as well as other local optima. The genetic algorithm produces a population or family of good designs which may include the global optimal design, rather than a single design. Hence, it is an appropriate tool for designing general grid-stiffened panels.

4.3 DESIGN PROBLEM DEFINITION

The present design problem is to minimize the weight per unit area of a grid-stiffened composite panel given the design loading condition, the length and width of the panel, the material properties for the skin and stiffeners, and the boundary conditions

of the panel. The design variables include stiffener spacings (a, b), the stacking sequence of the skin, stiffener layout, stiffener thickness (t_s), and stiffener height ($h_1 = h_2 = h_3 = h$) as shown in Figure 4.1. All stiffeners are assumed to be of the same height and thickness for manufacturing and assembly reasons. The design sought here is a panel of minimum weight in a certain design space which buckles globally at the design loads. This design problem can be defined by setting up the optimization procedures in the following way. First, the global buckling load is assumed to be a scalar multiple of design loads and has the form

$$N_x = \lambda_G N_1, \quad N_y = \lambda_G N_2, \quad N_{xy} = \lambda_G N_{12} \tag{4.2}$$

where N_1, N_2, N_{12} are the applied in-plane prebuckling loads. These values represent the design loads for the grid-stiffened panel. Second, the design constraints imposed on panel include

1. The critical buckling load should be greater than or equal to the design loads, that is, $\lambda_{cr} \geq 1$.

2. Skin segments should not buckle at the critical buckling load, that is, $\lambda_{sk} \geq 1$.

3. Stiffener segments should not cripple at the critical buckling load, that is, λ_1, λ_2, $\lambda_3 \geq 1$ where λ_1, λ_2, λ_3 is the crippling load factor of the x-direction stiffener, y-direction stiffener and diagonal stiffener, respectively.

The general form of each constraint equation is written as

$$g_j = (\frac{1}{\lambda_j} - 1) \leq 0.0 \quad j = 1, ..., N_c \tag{4.3}$$

Finally, the "Fitness" expression based on exterior penalty function approach is

$$\text{Fitness} = \quad (\frac{Q}{F(\mathbf{X}, r_i)}) = \text{Max} \frac{Q}{W(\mathbf{X}) + r_i \sum_j^{N_c} [|g_j(\mathbf{X})| + g_j(\mathbf{X})]^2} \tag{4.4}$$

where $\mathbf{X}$ = design variable vector

$F(\mathbf{X}, r_i)$ = Modified objective function

$W(\mathbf{X})$ = weight of panel per unit area

$r_i \sum_j^{N_c} [|g_j(\mathbf{X})| + g_j(\mathbf{X})]^2$ = penalty function

Q = normalizing constant

N_c = Number of design constraints

r_i = penalty parameter

i = generation or iteration cycle in the optimization procedure.

Once the global buckling load factor has been determined using the improved smeared stiffener theory, the loads acting on the stiffener and skin segments have to be determined by distributing the loads based on the extensional stiffness of the skin and the stiffener. The procedure for distributing the applied loads for a general grid-stiffened panel involves three steps. First, the extensional stiffness coefficients for grid-stiffened panel are computed as follows (Ref. [17]):

$$\begin{aligned}
(A_{11})_T &= \frac{2(A_{11})_1\, h}{b} + \frac{2(A_{11})_3\, h\, sin^3\theta}{b} + (A_{11})_s \\
(A_{22})_T &= \frac{2(A_{11})_2\, h}{a} + \frac{2(A_{11})_3\, h\, cos^3\theta}{a} + (A_{22})_s \\
(A_{66})_T &= \frac{2(A_{11})_3\, h\, cos\theta\, sin^2\theta}{a} + (A_{66})_s
\end{aligned} \tag{4.5}$$

where $(A_{11})_T$ is total smeared axial extensional stiffness of the grid-stiffened panel, $(A_{22})_T$ is the total smeared transverse extensional stiffness of the grid-stiffened panel, $(A_{66})_T$ is the total smeared in-plane shear stiffness of the grid stiffened panel, $(A_{11})_1$, $(A_{11})_2$, $(A_{11})_3$ are the extensional stiffness of the axial, transverse and diagonal stiffeners, respectively, $(A_{ij})_s$ is the extensional stiffness of the skin, θ is the orientation of the diagonal stiffener, and h is the height of the stiffener. Second, the loads carried by the skin segment which could be either a general parallelogram-shaped geometry or a general triangular-shaped geometry, at the global buckling load are

$$(N_x)_{sk} = \frac{(A_{11})_s}{(A_{11})_T} N_x = \frac{(A_{11})_s}{(A_{11})_T} \lambda_G N_1$$

$$
\begin{aligned}
(N_y)_{sk} &= \frac{(A_{22})_s}{(A_{22})_T} N_y = \frac{(A_{22})_s}{(A_{22})_T} \lambda_G N_2 \\
(N_{xy})_{sk} &= \frac{(A_{66})_s}{(A_{66})_T} N_{xy} = \frac{(A_{66})_s}{(A_{66})_T} \lambda_G N_{12}
\end{aligned} \tag{4.6}
$$

These values then correspond to the design loads used for the in-plane prebuckling load in the skin-segment local buckling computation. If the critical buckling load factor of the skin segment λ_{sk} is greater than or equal to one, then the skin-segment buckling load is greater than or equal the global buckling load of the grid-stiffened panel. Third, the loads carried by each stiffener type are computed. The load carried by the axial stiffener is

$$
(N_x)_1 = \frac{(A_{11})_1}{(A_{11})_T} N_x = \lambda_1 N_{crip} \tag{4.7}
$$

where N_{crip} is determined using Equation (4.1), and the critical buckling load factor, λ_1, of the axial stiffener has to be greater than or equal to one. The load carried by the transverse stiffener is

$$
(N_x)_2 = \frac{(A_{11})_2}{(A_{22})_T} N_y = \lambda_2 N_{crip} \tag{4.8}
$$

and the critical buckling load factor, λ_2, of the transverse stiffener has to be greater than or equal to one. The load in the diagonal stiffeners has components from the axial, transverse, and in-plane shear loadings and is given by

$$
(N_x)_3 = N_{dx} sin\theta + N_{dy} cos\theta + (N_{dxy})_x cos\theta + (N_{dxy})_y sin\theta = \lambda_3 N_{crip}
$$

where

$$
\begin{aligned}
N_{dx} &= \frac{(A_{11})_3 sin^3\theta}{(A_{11})_T} N_x \\
N_{dy} &= \frac{(A_{11})_3 cos^3\theta}{(A_{22})_T} N_y \\
(N_{dxy})_x &= \frac{(A_{11})_3 cos\theta sin^2\theta}{(A_{66})_T} \frac{b}{a} N_{xy} \\
(N_{dxy})_y &= \frac{(A_{11})_3 cos\theta sin^2\theta}{(A_{66})_T} N_{xy}
\end{aligned} \tag{4.9}
$$

N_{dx} is the contribution from the axial in-plane loading, N_{dy} is the contribution from the transverse inplane loading, $(N_{dxy})_x$ is the contribution from the in-plane shear

loading along the edge where x is constant, and $(N_{dxy})_y$ is the contribution from the in-plane shear loading along the edge where y is constant. The critical buckling load factor, λ_3, of the diagonal stiffener has to be greater than or equal to one.

The weight per unit area of the grid-stiffened panel is

$$W = \frac{\rho}{ab}(w_1 + w_2 + w_3 + w_s)$$

where

$$\begin{aligned} w_1 &= 2\,h\,a\,t_s \\ w_2 &= 2\,h\,b\,t_s \\ w_3 &= 2\,h\,t\,\sqrt{a^2+b^2} \\ w_s &= a\,b\,t_{skin} \end{aligned} \tag{4.10}$$

w_1 is the volume of the axial stiffeners in the unit cell, w_2 is the volume of the transverse stiffeners in the unit cell, w_3 is the volume of the diagonal stiffeners in the unit cell, w_s is the volume of the skin in the unit cell, t_{skin} is the thickness of skin, and ρ is the mass density of the material.

4.4 DESIGN PROCESS BASED ON GENETIC ALGORITHM

Implementation of the genetic algorithm is shown schematically in Figure 4.2. The design process begins with a random selection of a specified number of designs which comprise the initial population (i.e., first generation) for the genetic algorithm. Material properties, length and width of panel, boundary conditions of the stiffened panel, and design loadings are input to the analysis processor routine. The buckling analysis is performed which provides the critical eigenvalues for the global buckling response of the grid-stiffened panel and the local buckling response of the skin and stiffener segments, which also computes the weight per unit area of the grid-stiffened panel. This procedure is repeated for each design configuration in the population.

The "fitness" processor then evaluates the "fitness" of each design using Equation (4.4) and assign a rank based on the fitness expression or objective function. The current population of design configurations is then processed by the genetic operators (crossover, mutation, and permutation) to create a new population of design configurations for the next generations which combines the most desirable characteristics of previous generations. Designs from previous generations may be replaced by new ones (i.e., children) except for the "most fit" designs (i.e., parents) which are always included in the next generation. The process is repeated until design convergence is obtained, which is defined herein by specifying a maximum number of generations that may occur without improvement in the best design. The design procedure will now be demonstrated on flat and curved grid stiffened panels.

4.5 NUMERICAL RESULTS FOR FLAT GRID-STIFFENED PANELS

A composite grid-stiffened panel 20.0-in. long and 56.0-in. wide representative of a generic transport helicopter fuselage structural component is used as an example to demonstrate the capabilities of the design optimization tool using the genetic algorithm and global and local analyses. The panel is subjected to load cases shown in Table 4.1. The panel was optimized for a load case of 400.0 lbs/in. in axial compression, which is considered to be the most critical load case for this panel, the stopping criterion is 30 generations, and the population size is eight. The probabilities used for crossover, mutation, and permutation are 1.0, 0.10, and 0.95, respectively. Also, the penalty parameter r_i is kept constant for all iterations. Two skin laminate stacking sequences were chosen. The first stacking sequence is $[60/0/-60]_s$, the second one is $[\pm 45/90/0]_s$, and each ply is 0.006-in. thick. Both of these laminates are quasi-isotropic. The stiffener is made of 0° material only. The nominal ply mechanical properties used are: $E_{11} = 20.2$ Msi; $E_{22} = 1.9$ Msi;

$G_{12} = G_{13} = G_{23} = 0.73$ Msi and $\nu_{12} = 0.3$. The mass density of the material ρ, is 0.0570 lbs/in.^{3} The grid-stiffened panel has simply supported boundary conditions on all edges, and the skin segments are considered to be simply supported also. The grid-stiffened panel is assumed to have only axial and diagonal stiffeners. The axial and transverse stiffener spacings considered were such that all stiffener patterns closely approximate an isogrid configuration. Hence, the axial stiffener spacing a and transverse stiffener spacing b are not independent but are considered as a single design variable, (i.e., (a_s, b_s) is one variable). The stiffener height h and thickness t_s are also design variables. The design space explored is indicated in Table 4.2, where due to manufacturing constraints, the height of the triangle $(b_s/2)$ is kept between 2.9 and 6.0 in., and the stiffener aspect ratio (h/t_s) is kept between 4.5 and 9.0. Each design variable can assume only eight discrete values.

In the buckling analyses, regular polynomials are used for the buckling analyses since it is computationally faster than the analysis using Legendre polynomials. The grid-stiffened panel is simply supported on all edges and so are the local skin segments.

The results obtained by using the present design optimization tool are shown in Table 4.3 for the skin with a laminate stacking sequence of $[60/0/-60]_s$ and in Table 4.4 for the skin with a laminate stacking sequence of $[\pm 45/90/0]_s$. Since only three design variables are present, the size of each population of the genetic algorithm is taken as eight. Only the five best designs are given for each of the two grid-stiffened panels with different skin stacking sequences.

For the grid-stiffened panel with the $[60/0/-60]_s$ skin laminate, the first three designs in Table 4.3 correspond to grid-stiffened panels that buckle globally at a load factor of λ_G, since the local buckling load factor of the skin segment λ_{sk}, axial stiffener segment λ_1, and diagonal stiffener segment λ_3, are greater than one. The third design however, has a global buckling load factor (λ_G) of 0.969, which may still

be an acceptable design since λ_G is very close to one. The fourth and fifth designs have local buckling load factors of the skin segment less than one, and therefore the buckling mode of these designs will contain local skin buckling at a load factor equal to $\lambda_G \times \lambda_{sk}$. The buckling load factor for the fourth and fifth designs is 1.244 and 1.089, respectively, however the weight per unit area of these two panels are about 18 percent greater than those of the first three designs. From Table 4.3, only the stiffener height appears to be evolving while the stiffener spacing appears to have locked on to a specific value. Therefore, the best design for the grid-stiffened panel with $[60/0/-60]_s$ skin laminate is the first design given in Table 4.3 within the design space considered. The behavior of the genetic algorithm convergence for the grid-stiffened panel with $[60/0/-60]_s$ skin laminate, is shown in Figure 4.3 and is very rapid.

For the grid-stiffened panel with $[\pm 45/90/0]_s$ skin laminate, the designs shown in Table 4.4 are of grid-stiffened panels that buckle globally at the indicated load factor of λ_G, since the local buckling load factors (λ_{sk}, λ_1, λ_3) are all greater than one. The first and third designs have a global buckling load factor λ_G of 0.995 and 0.991, respectively, and could still acceptable designs. The second and third designs have different stiffener spacing, and yet the global buckling load factor and weight per unit area of these two panels are very close to one another. The fourth and fifth designs show the same behavior also. Hence, the ability of the genetic algorithm to obtain multiple optima of comparable performance is demonstrated. The best design for the grid-stiffened panel with a $[\pm 45/90/0]_s$ skin laminate is the first design given in Table 4.4. The convergence behavior of the genetic algorithm for the grid-stiffened panel with a $[\pm 45/90/0]_s$ skin laminate is also shown in Figure 4.3.

The best designs with the $[60/0/-60]_s$ skin laminate and the $[\pm 45/90/0]_s$ skin laminate are now assessed using the load cases given in Table 4.1. The results are shown in Table 4.5 for the grid-stiffened panel with $[60/0/-60]_s$ skin laminate and in Table 4.6 for the grid-stiffened panel with $[\pm 45/90/0]_s$ skin laminate. Additional load cases are also considered in order to obtain a profile for the critical loads of these panels. They are 400.0 lbs/in. axial compression and 10.0 lbs/in. axial compression with 100.0 lbs/in. in-plane shear. Both panels buckle globally for most of the load cases considered. Both grid-stiffened panels exhibit crippling of the diagonal stiffener for load case of $N_{xy} = 100$ lbs.in., $N_x = 10$ lbs/in. In addition, the grid-stiffened panel with the $[\pm 45/90/0]_s$ skin laminate exhibits local skin buckling for load case of $N_x = 174.0$ lbs/in. and $N_{xy} = 154.0$ lbs/in. The global buckling load factor λ_G for this load case is 2.2382 and the skin local buckling load factor λ_{sk} is 0.9855, and hence the buckling load factor is 2.2057 for this load case of $N_x = 174.0$ lbs/in. and $N_{xy} = 154.0$ lbs/in. As shown in Figure 4.4, the designed load cases are within the critical loading profile or envelope for the grid-stiffened panels with $[60/0/-60]_s$ skin laminate and $[\pm 45/90/0]_s$ skin laminate. The grid-stiffened panel with $[60/0/-60]_s$ skin laminate is a better design than the one with $[\pm 45/90/0]_s$ skin laminate, since it has a weight of 0.549 lbs/ft^2 compared to 0.578 lbs/ft^2 for the latter panel. Also the former design has a larger critical load envelope compared to the grid-stiffened panel with $[\pm 45/90/0]_s$ skin laminate (see Figure 4.4).

4.6 NUMERICAL RESULTS FOR CURVED GRID-STIFFENED PANELS

The fuselage design of a generic wide-body transport aircraft is typically divided into three different quadrants as shown in Figure 4.5. These quadrants include a crown panel, two side panels and a keel panel. A side quadrant panel of a fuselage structure representative of a generic transport aircraft fuselage section is considered herein and

designed for buckling. The side quadrant panel is shown in Figure 4.6 and longerons and frames divide the side quadrant panel into four curved panels. Each panel is 22.0-in. long and 22.0-in. wide with a radius of 120.0-in. in the width direction. Panel 1 is the forward top panel of the side quadrant panel and is subjected to a load case of N_x = 1250 lbs/in., N_{xy} = 250 lbs/in., and N_y = 2200 lbs/in. hoop tension. Panel 2 is the aft top panel of the side quadrant panel and is subjected to a load case of N_x = 300 lbs/in., N_{xy} = 1350 lbs/in., and N_y = 2200 lbs/in. hoop tension. Panel 3 is the bottom top panel of the side quadrant panel and is subjected to a load case of N_x = 2250 lbs/in., N_{xy} = 250 lbs/in., and N_y = 2200 lbs/in. hoop tension. The panel hoop tension is due to internal pressurization of the fuselage. The nominal ply mechanical properties used are: E_{11} = 20.2 Msi; E_{22} = 1.9 Msi; $G_{12} = G_{13} = G_{23}$ = 0.73 Msi and ν_{12} = 0.3. The mass density of the material ρ is 0.0570 lbs/in.^{3} The grid-stiffened panel has simply supported boundary conditions on all edges, and the individual skin segments are considered to be simply supported also. The stiffeners are made of unidirectional material. The stopping criteria for the design evolution is 25 generations with no improvement in the "best " design, and the population size is twelve. The probabilities used for crossover, mutation, and permutation are 1.0, 0.10, and 0.95, respectively. Also, the penalty parameter r_i is kept constant for all iterations.

The design variables are the axial stiffener spacing (a), the transverse stiffener spacing (b), the stiffener height (h), stiffener thickness (t_s), the stacking sequence of the skin laminate ($LAMI$), and the geometry of the stiffening configuration ($IGEO$). The design variables are shown in Table 4.7, and the design space explored is shown in Table 4.8 for Panels 1 and 3, and in Table 4.9 for Panel 2. In either design space, the minimum stiffener spacing is restricted to two inches, and the aspect ratio of the stiffener (h/t_s) was kept between 3.5 and 10.5 due to manufacturing constraints. Each design variable can assume eight discrete values.

In the buckling analyses, regular polynomials are used for the buckling analyses since it is computationally faster than the analysis using Legendre polynomials. The grid-stiffened panel is simply supported on all edges and so are the local skin segments. Sanders-Koiter shell theory is used.

The results obtained for Panel 1 using the present design optimization tool are shown in Table 4.10. Eight best designs are presented here. All panel designs presented in Table 4.10 buckle globally at the corresponding global load factor of λ_G. The buckling load factor of some stiffener segments are negative, which means that these stiffener segments are in tension and do not buckle due to the in-plane loads considered. Hence, the magnitude of negative buckling load factors for rib segments are assumed to be one in computing the objective function (Equation 4.4). The optimum value of the stiffening geometry variable ($IGEO$) for all the panels is six (i.e., the grid-stiffened panel has only transverse and diagonal stiffeners). The first six best designs have the same stiffener spacings of $a = 4.889$ in., and $b = 6.2857$ in., while the stiffener height (h), the stiffener thickness (t_s), and the skin-laminate stacking sequence ($LAMI$) are evolving. However, the stiffener height is evolving more than the stiffener thickness (t_s), and the skin laminate stacking sequence ($LAMI$). The first four designs have a stiffener thickness of 0.06 in., while the fifth and sixth design have stiffener thickness of 0.09 in. and 0.102 in., respectively. The fourth design has a skin laminate stacking sequence of $[\pm 45/0]_{2s}$ ($LAMI = 1$), while the other five designs have a skin laminate stacking sequence of $[\pm 45/90]_{2s}$ ($LAMI = 2$). The seventh and eighth designs have the same stiffener spacings ($a = 4.0$ in., and $b = 5.5$ in.), and stiffener thickness ($t_s = 0.09$ in.), but the stiffener height and skin laminate stacking sequence are different from the first six designs. The best design for Panel 1 is the first design in Table 4.10. The convergence behavior of the genetic algorithm for Panel 1 is shown in Figure 4.7, and convergence is achieved after 75 iterations (i.e, 75 generations).

The results obtained for Panel 2 using the present optimization tool are shown in Table 4.11. The panel designs presented in Table 4.11 buckle globally at the corresponding global load factor of λ_G. The genetic algorithm produces a large pool of good designs in this case. Most of the good designs are panels with only axial stiffeners. These axially stiffened panels have stiffener spacings such as those of the first three designs presented in Table 4.10, but with different stiffener height and thickness. The fourth design in Table 4.10 has transverse and diagonal stiffeners ($IGEO = 6$); however, this design is 14 percent heavier than the first design. Panels stiffened in only one direction do not typically have good damage tolerance characteristics, since multiple or redundant load paths for load redistribution are absent. Therefore, the design process was performed with a modified design space for the stiffening geometry wherein values of $IGEO = 1$ and 2 are replaced by $IGEO = 5$ and 6 respectively. That is, all designs will include stiffeners in multiple directions. The results for this optimization are shown in Table 4.12. The panels presented in Table 4.12 buckle globally at the corresponding global load factor of λ_G. Here again, the genetic algorithm produces a large pool of good designs with axial and transverse stiffeners ($IGEO = 3$). These panels have stiffener spacing such as the first six designs of Table 4.12, with variation in stiffener height and thickness and with a skin laminate stacking sequence of $[\pm 45/0]_{2s}$ ($LAMI = 1$) or $[\pm 45/90]_{2s}$ ($LAMI = 2$). The weight of each panel is comparable to the weight of the axially stiffened panels presented in Table 4.11. The seventh design has both axial and diagonal stiffeners ($IGEO = 5$), while the eighth design is the same as the fourth design presented in Table 4.11. The best design for Panel 2 is the design with transverse and diagonal stiffeners, which is the fourth design in Table 4.11 and eighth design in Table 4.12. This design is preferred over the lighter weight axially stiffened panel and the axially and transversely stiffened panel since panel with diagonal stiffening is more damage tolerant. It is also preferred over the seventh design in Table 4.12, since it has more

stiffeners than the axially and diagonally stiffened and its weight is close to that of the latter. The convergence behavior of the genetic algorithm for Panel 2 is shown in Figure 4.7. The convergence is faster when there is no restriction on the stiffening geometry variable ($IGEO$).

The results obtained for Panel 3 using the present optimization tool is shown in Table 4.13. The panel designs presented in Table 4.13 buckle globally at the corresponding global load factor of λ_G. The best design is obtained with stiffener spacings of $a = 5.5$ in. and $b = 4.4$ in. The panel has transverse and diagonal stiffeners ($IGEO = 6$) and a skin laminate stacking sequence of $[\pm 45/90]_{2s}$ ($LAMI = 2$). The second design is essentially same as the first design with the stiffener height being different. The other good designs are panels with axial and transverse stiffeners, which are about 36 percent heavier than the first two design. The best design for Panel 3 is the first design in Table 4.13 and the convergence is achieved after 29 iterations as shown in Figure 4.7.

The best design obtained for Panel 3 is now assessed for the design load cases used for Panel 1 and Panel 2. The results are shown in Table 4.14. For the load case corresponding to Panel 1, the panel buckles globally at a buckling load factor of 2.114, and hence, this design represents a conservative design for these loads. However, for the load case corresponding to Panel 2, the buckling load factor of the diagonal stiffener is 0.255, and hence, the buckling deformation contains local buckling of the diagonal stiffener at a load factor of $\lambda_3 \times \lambda_G = 1.172$. Therefore, this design also represents a conservative design for these loads. of Panel 3. The best design for Panel 3 can also be used for Panel 1 and Panel 2 with a weight penalty of 6.7 and 22.9 percent, respectively, when compared to their respective best design. For a fuselage structure, it is desirable that all the panels have the same stiffening pattern. This is not only due to manufacturing consideration, but also due to structural consideration. The region where stiffeners from two different panel meet will have to be joined and

is a critical area if the stiffening patterns of the two panels are not the same. To alleviate that problem, these nodes have to be reinforced, and could result in a higher weight penalty than using Panel 3 configuration also for Panels 1 and 2.

4.6.1 Curved Panels without Hoop Tension

Since the hoop tension of $N_y = 2200$ lbs/in. due to fuselage internal pressurization is a stabilizing in-plane load, the design optimization is performed for the three panels without any hoop tension (i.e., $N_y = 0$). The results are shown in Table 4.15, Table 4.16, and Table 4.17 for Panel 1, Panel 2, and Panel 3, respectively. The seven best designs obtained by the genetic algorithm for Panel 1 are shown in Table 4.15. All the designs presented in Table 4.15 buckle globally at the corresponding global buckling load factor λ_G. The top two best designs have diagonal stiffeners only ($IGEO$=4). These two designs are essentially the same, except for the stiffener height. The next three best designs have diagonal and transverse stiffeners ($IGEO$=6), and have the same stiffener spacing and skin-laminate stacking sequence, but with different stiffener height and thickness. The sixth design has axial and transverse stiffeners, whereas the seventh design has transverse and diagonal stiffeners. The first four designs presented in Table 4.15 are lighter than the best design for Panel 1 with the hoop tension by 1.7 to 4.1 percent. These designs have skin-laminate stacking sequence of $[\pm 45/0_2]_{2s}$ and an axial stiffener spacing of 11.0 in. compared to a skin-laminate stacking sequence of $[\pm 45/90]_{2s}$ and an axial stiffener spacing of 4.889 in. for the best design of Panel 1 with the hoop tension.

For Panel 2, the eight best designs are shown in Table 4.16. All designs presented in Table 4.16 buckle globally at the corresponding global buckling load factor λ_G. The first five designs have diagonal stiffeners only, and the last three designs have axial and diagonal stiffeners only. Here all the design variables are evolving without being locked on any particular value. Only the first two designs

have a weight per unit area comparable to the best design for Panel 2 with the hoop tension load included (fourth design in Table 4.11). These two panels are about 7 percent heavier. Optimization results for Panel 3 are shown in Table 4.17 where only the five best design are shown. These designs buckle globally at their corresponding global buckling load factor λ_G. The first four designs have transverse and diagonal stiffeners only, while the fifth design have axial and diagonal stiffeners only. The first four designs have a small variation in value for the axial and transverse spacings, and stiffener height and thickness, and the weight per unit area of these designs are comparable to each other. The best design in Table 4.17 is heavier than the best design for Panel 3 with the hoop tension by 11.6 percent.

The best design for Panel 3 without the hoop tension load is now assessed for the load case of Panel 1 and Panel 2 without the hoop tension load. The results are shown in Table 4.18. For the load case corresponding to Panel 1 without the hoop tension, the panel buckles globally at a global buckling load factor of 1.797. Therefore, the panel does not buckle for the load case corresponding to that of Panel 1 without the hoop tension. However, for the load case corresponding to Panel 2 without the hoop tension, the buckling load factor of the diagonal stiffener is 0.697, and hence the buckling deformation contains local buckling of the diagonal stiffener at a load factor of $\lambda_3 \times \lambda_G = 1.719$. Therefore, the panel does not buckle at a load case corresponding to that of Panel 3 without the hoop tension. The best design for Panel 3 can be used for Panel 1 and Panel 2 with a weight penalty of 24.3 and 28.5 percent respectively, when compared to their respective best design.

4.7 SUMMARY

A minimum-weight design optimization tool for grid-stiffened panels with a global buckling constraint using global and local analyses and the genetic algorithm has been developed. Design variables used are the axial and transverse stiffener spacing,

stiffener height and thickness, the skin-laminate stacking sequence, and the stiffening geometry. Results for flat and curved grid-stiffened panels indicate that the best designs obtained by the genetic algorithm depend mostly on the applied load cases. In most combined applied load cases, the best designs have diagonal stiffeners. However in certain cases, the best design obtained by using the genetic algorithm solely based on buckling considerations may not be suitable for structural application due to considerations related to manufacturing, joining, and damage tolerance. In this case, the pool of good designs obtained by the genetic algorithm is useful in providing alternative design options for a given structural application.

Table 4.1 Service load cases for flat composite grid-stiffened panel.

Load case	N_1 (lbs/in.)	N_{12} (lbs/in.)
1	396.0	130.0
2	326.0	178.0
3	271.0	139.0
4	174.0	154.0

Table 4.2 Design space.

Design Variable 1		Design Variable 2	Design Variable 3
Stiffener spacing axial, in. (a_s)	transverse, in. (b_s)	stiffener height, in. (h)	stiffener thickness, in. (t_s)
6.667	11.200	0.49375	0.060
5.714	10.182	0.50000	0.066
5.000	8.615	0.50625	0.072
4.444	8.000	0.51250	0.078
4.444	7.467	0.51875	0.084
4.000	7.000	0.52500	0.090
3.636	6.222	0.53125	0.096
3.333	5.894	0.53750	0.102

Table 4.3 Best designs obtained by genetic algorithm for grid-stiffened panel with skin of $[60/0/-60]_s$ stacking sequence.

a (in.)	b (in.)	h (in.)	t_s (in.)	λ_G	λ_{sk}	λ_1	λ_3	weight lbs/ft^2
3.333	5.894	0.50000	0.060	1.002	1.044	2.072	34.594	0.549
3.333	5.894	0.50625	0.060	1.034	1.016	2.002	33.421	0.552
3.333	5.894	0.49375	0.060	0.969	1.073	2.147	35.856	0.545
3.333	5.894	0.51875	0.084	1.403	0.887	3.241	54.130	0.663
3.636	6.222	0.53750	0.084	1.487	0.733	2.669	41.656	0.651

Table 4.4 Best designs obtained by genetic algorithm for grid-stiffened panel with skin of $[\pm 45/0/90]_s$ stacking sequence.

a (in.)	b (in.)	h (in.)	t_s (in.)	λ_G	λ_{sk}	λ_1	λ_3	weight lbs/ft^2
5.000	8.615	0.53750	0.060	0.995	1.024	1.341	21.208	0.578
4.444	8.000	0.53750	0.060	1.047	1.179	1.470	25.608	0.596
4.444	7.467	0.51250	0.060	0.991	1.392	1.637	24.507	0.594
4.444	7.467	0.51250	0.072	1.139	1.285	2.146	32.120	0.634
4.444	8.000	0.53750	0.072	1.207	1.084	1.920	33.458	0.636

Table 4.5 Buckling loads for grid-stiffened panel with skin of $[60/0/-60]_s$ stacking sequence.

N_x (lbs/in.)	N_{xy} (lbs/in.)	Buckling load factor (λ)	Buckling mode
400.0	0.000	1.002	global buckling
396.0*	130.0*	1.015	global buckling
326.0*	178.0*	1.226	global buckling
271.0*	139.0*	1.477	global buckling
174.0*	154.0*	2.268	global buckling
10.00	100.0	6.407	diagonal stiffener buckling

* refers to service load cases from Table 4.1

Table 4.6 Buckling loads for grid-stiffened panel with skin of $[\pm 45/0/90]_s$ stacking sequence.

N_x (lbs/in.)	N_{xy} (lbs/in.)	Buckling load factor (λ)	Buckling mode
400.0	0.000	0.995	global buckling
396.0*	130.0*	1.002	global buckling
326.0*	178.0*	1.211	global buckling
271.0*	139.0*	1.458	global buckling
174.0*	154.0*	2.206	skin buckling, $\lambda_G = 2.238$, $\lambda_{sk} = 0.985$
10.00	100.0	4.145	diagonal stiffener buckling

* refers to service load cases from Table 4.1

Table 4.7 Design variables.

Design variable	
1	axial stiffener spacing, a
2	transverse stiffener spacing, b
3	stiffener height, h
4	stiffener thickness, t_s
5	stacking sequence of skin laminate, $LAMI$
6	stiffening geometry, $IGEO$

Table 4.8 Design space for curved Panel 1 and 3.

	Design Variable					
	1	2	3	4	5	6
	a, in.	b, in.	h, in.	t_s, in.	*LAMI*	*IGEO*
1	11.000	11.000	0.49375	0.060	$[\pm 45/0]_{2s}$	axial stiffening
2	8.800	8.800	0.50000	0.066	$[\pm 45/90]_{2s}$	transverse stiffening
3	7.333	7.333	0.50625	0.072	$[\pm 45/0/90]_{2s}$	orthogrid stiffening
4	6.286	6.286	0.51250	0.078	$[\pm 45/0_2]_{2s}$	diagonal stiffening
5	5.500	5.500	0.51875	0.084	$[\pm 45/90_2]_{2s}$	axial and diagonal stiffening
6	4.889	4.889	0.52500	0.090	$[\pm 45/0_2/90]_{2s}$	transverse and diagonal stiffening
7	4.400	4.400	0.53125	0.096	$[\pm 45/0/90_2]_{2s}$	axial, transverse and diagonal stiffening
8	4.000	4.000	0.53750	0.102	$[\pm 45/0_2/90_2]_{2s}$	no stiffening

Table 4.9 Design space for curved Panel 2.

	Design Variable					
	1	2	3	4	5	6
	a, in.	b, in.	h, in.	t_s, in.	*LAMI*	*IGEO*
1	11.000	11.000	0.30	0.042	$[\pm 45/0]_{2s}$	axial stiffening
2	8.800	8.800	0.32	0.048	$[\pm 45/90]_{2s}$	transverse stiffening
3	7.333	7.333	0.34	0.054	$[\pm 45/0/90]_{2s}$	orthogrid stiffening
4	6.286	6.286	0.36	0.060	$[\pm 45/0_2]_{2s}$	diagonal stiffening
5	5.500	5.500	0.38	0.066	$[\pm 45/90_2]_{2s}$	axial and diagonal stiffening
6	4.889	4.889	0.40	0.072	$[\pm 45/0_2/90]_{2s}$	transverse and diagonal stiffening
7	4.400	4.400	0.42	0.078	$[\pm 45/0/90_2]_{2s}$	axial, transverse and diagonal stiffening
8	4.000	4.000	0.44	0.084	$[\pm 45/0_2/90_2]_{2s}$	no stiffening

Table 4.10 Best designs obtained by genetic algorithm for grid-stiffened curved Panel 1.

Design variables	Weight lbs/ft^2	Buckling load factors
a = 4.8890 in., b = 6.2857 in., h = 0.500 in., t_s = 0.060 in., $LAMI$:= $[\pm 45/90]_{2s}$, $IGEO$:= 6	0.819	λ_G = 1.080, λ_{sk} = 1.290 λ_2 = -0.394, λ_3 = 18.189
a = 4.8890 in., b = 6.2857 in., h = 0.5125 in., t_s = 0.060 in., $LAMI$:= $[\pm 45/90]_{2s}$, $IGEO$:= 6	0.825	λ_G = 1.132, λ_{sk} = 1.232 λ_2 = -0.368, λ_3 = 16.343
a = 4.8890 in., b = 6.2857 in., h = 0.525 in., t_s = 0.060 in., $LAMI$:= $[\pm 45/90]_{2s}$, $IGEO$:= 6	0.831	λ_G = 1.121, λ_{sk} = 1.246 λ_2 = -0.363, λ_3 = 15.588
a = 4.8890 in., b = 6.2857 in., h = 0.53125 in., t_s = 0.060 in., $LAMI$:= $[\pm 45/0]_{2s}$, $IGEO$:= 6	0.833	λ_G = 1.018, λ_{sk} = 1.512 λ_2 = -0.250, λ_3 = -1.990
a = 4.8890 in., b = 6.2857 in., h = 0.49375 in., t_s = 0.090 in., $LAMI$:= $[\pm 45/90]_{2s}$, $IGEO$:= 6	0.929	λ_G = 1.292, λ_{sk} = 1.102 λ_2 = -0.841, λ_3 = -19.891
a = 4.8890 in., b = 6.2857 in., h = 0.49375 in., t_s = 0.102 in., $LAMI$:= $[\pm 45/90]_{2s}$, $IGEO$:= 6	0.974	λ_G = 1.398, λ_{sk} = 1.027 λ_2 = -1.034, λ_3 = 20.672
a = 4.000 in., b = 5.500 in., h = 0.49375 in., t_s = 0.090 in., $LAMI$:= $[\pm 45/90]_{2s}$, $IGEO$:= 6	0.999	λ_G = 1.338, λ_{sk} = 1.387 λ_2 = -0.989, λ_3 = 125.174
a = 4.000 in., b = 5.500 in., h = 0.500 in., t_s = 0.090 in., $LAMI$:= $[\pm 45/0]_{2s}$, $IGEO$:= 6	1.004	λ_G = 1.253, λ_{sk} = 1.577 λ_2 = -0.740, λ_3 = -6.016

Table 4.11 Best designs obtained by genetic algorithm for grid-stiffened curved Panel 2.

Design variables	Weight lbs/ft^2	Buckling load factors
b = 11.0 in., h = 0.360 in., t_s = 0.060 in., $LAMI$:= $[\pm 45/0]_{2s}$, $IGEO$:= 1	0.6232	λ_G = 1.061, λ_{sk} = 16.494 λ_1 = 2.745
b = 7.333 in., h = 0.340 in., t_s = 0.042 in., $LAMI$:= $[\pm 45/0]_{2s}$, $IGEO$:= 1	0.6229	λ_G = 0.998, λ_{sk} = 221.17 λ_1 = 1.62
b = 6.2857 in., h = 0.340 in., t_s = 0.042 in., $LAMI$:= $[\pm 45/0]_{2s}$, $IGEO$:= 1	0.6283	λ_G = 1.129, λ_{sk} = 206.79 λ_1 = 1.45
a = 5.5 in., b = 6.2857 in., h = 0.320 in., t_s = 0.054 in., $LAMI$:= $[\pm 45/0]_{2s}$, $IGEO$:= 6	0.711	λ_G = 0.996, λ_{sk} = 5.01 λ_2 = -.30, λ_3 = 1.650

Table 4.12 Best designs obtained by genetic algorithm for grid-stiffened curved Panel 2, with $IGEO$ = 1,2 not being a design variable.

Design variables	Weight lbs/ft^2	Buckling load factors
a = 11.0 in., b = 8.8 in., h = 0.340 in., t_s = 0.042 in., $LAMI$:= $[\pm 45/0]_{2s}$, $IGEO$:= 3	0.6389	λ_G = 1.038, λ_{sk} = 3.05 λ_1 = 2.01, λ_2 = -0.149
a = 11.0 in., b = 11.0 in., h = 0.340 in., t_s = 0.048 in., $LAMI$:= $[\pm 45/90]_{2s}$, $IGEO$:= 3	0.6396	λ_G = 1.022, λ_{sk} = 2.07 λ_1 = 1.28, λ_2 = -0.360
a = 11.0 in., b = 7.333 in., h = 0.320 in., t_s = 0.042 in., $LAMI$:= $[\pm 45/90]_{2s}$, $IGEO$:= 3	0.6411	λ_G = 1.076, λ_{sk} = 4.141 λ_1 = 1.07, λ_2 = -0.366
a = 11.0 in., b = 7.333 in., h = 0.320 in., t_s = 0.042 in., $LAMI$:= $[\pm 45/0]_{2s}$, $IGEO$:= 3	0.6411	λ_G = 1.061, λ_{sk} = 4.162 λ_1 = 2.17, λ_2 = -0.178
a = 8.8 in., b = 8.8 in., h = 0.340 in., t_s = 0.042 in., $LAMI$:= $[\pm 45/90]_{2s}$, $IGEO$:= 3	0.6442	λ_G = 1.083, λ_{sk} = 2.979 λ_1 = 1.08, λ_2 = -0.300
a = 8.8 in., b = 8.8 in., h = 0.340 in., t_s = 0.042 in., $LAMI$:= $[\pm 45/0]_{2s}$, $IGEO$:= 3	0.6442	λ_G = 1.055, λ_{sk} = 3.169 λ_1 = 2.26, λ_2 = -0.151
a = 11.0 in., b = 11.0 in., h = 0.340 in., t_s = 0.084 in., $LAMI$:= $[\pm 45/0]_{2s}$, $IGEO$:= 5	0.6938	λ_G = 2.160, λ_{sk} = 2.442 λ_1 = 3.23, λ_3 = 1.234
a = 5.5 in., b = 6.2857 in., h = 0.320 in., t_s = 0.054 in., $LAMI$:= $[\pm 45/0]_{2s}$, $IGEO$:= 6	0.711	λ_G = 0.999, λ_{sk} = 5.01 λ_2 = -.30, λ_3 = 1.650

Table 4.13 Best designs obtained by genetic algorithm for grid-stiffened curved Panel 3.

Design variables	Weight lbs/ft^2	Buckling load factors
a = 5.500 in., b = 4.400 in., h = 0.50625 in., t_s = 0.072 in., $LAMI$:= $[\pm 45/90]_{2s}$, $IGEO$:= 6	0.874	λ_G = 1.014, λ_{sk} = 1.369 λ_2 = -0.781, λ_3 = 1.191
a = 5.500 in., b = 4.400 in., h = 0.51875 in., t_s = 0.072 in., $LAMI$:= $[\pm 45/90]_{2s}$, $IGEO$:= 6	0.881	λ_G = 1.055, λ_{sk} = 1.325 λ_2 = -0.741, λ_3 = 1.134
a = 5.500 in., b = 7.333 in., h = 0.525 in., t_s = 0.072 in., $LAMI$:= $[\pm 45/0/90_2]_{2s}$, $IGEO$:= 3	1.182	λ_G = 1.139, λ_{sk} = 4.142 λ_1 = 1.161, λ_2 = -1.183
a = 4.889 in., b = 7.333 in., h = 0.51875 in., t_s = 0.072 in., $LAMI$:= $[\pm 45/0/90_2]_{2s}$, $IGEO$:= 3	1.194	λ_G = 1.121, λ_{sk} = 3.477 λ_1 = 1.401, λ_2 = -1.234
a = 6.2857 in., b = 8.8 in., h = 0.50625 in., t_s = 0.096 in., $LAMI$:= $[\pm 45/0/90_2]_{2s}$, $IGEO$:= 3	1.202	λ_G = 1.146, λ_{sk} = 2.707 λ_1 = 1.679, λ_2 = -1.722
a = 6.2857 in., b = 8.8 in., h = 0.5125 in., t_s = 0.096 in., $LAMI$:= $[\pm 45/0/90_2]_{2s}$, $IGEO$:= 3	1.205	λ_G = 1.168, λ_{sk} = 2.662 λ_1 = 1.641, λ_2 = -1.676

Table 4.14 Buckling loads for Panel 3 best design subjected to the load case of Panels 1 and 2.

	Load Case (lbs/in.)	Buckling load factors
(Panel 1)	N_x = 1250, N_y = -2200, N_{xy} = 250.	λ_G = 2.114, λ_{sk} = 1.488, λ_2 = -0.374, λ_3 = 1.0113 (Global buckling at λ_G = 2.114)
(Panel 2)	N_x = 300, N_y = -2200, N_{xy} = 1350.	λ_G = 4.595, λ_{sk} = 2.409, λ_2 = -0.172, λ_3 = 0.255 (Local buckling at $\lambda_3 \times \lambda_G$) = 1.172

Table 4.15 Best designs obtained by genetic algorithm for grid-stiffened curved Panel 1, with $N_y = 0$.

Design variables	Weight lbs/ft^2	Buckling load factors
$a = 11.0$ in., $b = 4.0$ in., $h = 0.49375$ in., $t_s = 0.090$ in., $LAMI$:= $[\pm 45/0_2]_{2s}$, $IGEO$:= 4	0.785	$\lambda_G = 1.027$, $\lambda_{sk} = 1.193$ $\lambda_3 = 1.676$
$a = 11.0$ in., $b = 4.0$ in., $h = 0.5$ in., $t_s = 0.090$ in., $LAMI$:= $[\pm 45/0_2]_{2s}$, $IGEO$:= 4	0.787	$\lambda_G = 1.045$, $\lambda_{sk} = 1.178$ $\lambda_3 = 1.630$
$a = 11.0$ in., $b = 4.4$ in., $h = 0.49375$ in., $t_s = 0.078$ in., $LAMI$:= $[\pm 45/0_2]_{2s}$, $IGEO$:= 6	0.803	$\lambda_G = 1.065$, $\lambda_{sk} = 1.185$ $\lambda_3 = 1.168$
$a = 11.0$ in., $b = 4.4$ in., $h = 0.5$ in., $t_s = 0.078$ in., $LAMI$:= $[\pm 45/0_2]_{2s}$, $IGEO$:= 6	0.805	$\lambda_G = 1.085$, $\lambda_{sk} = 1.167$ $\lambda_3 = 1.167$
$a = 11.0$ in., $b = 4.4$ in., $h = 0.49375$ in., $t_s = 0.096$ in., $LAMI$:= $[\pm 45/0_2]_{2s}$, $IGEO$:= 6	0.852	$\lambda_G = 1.179$, $\lambda_{sk} = 1.135$ $\lambda_3 = 1.648$
$a = 6.2857$ in., $b = 4.4$ in., $h = 0.50625$ in., $t_s = 0.096$ in., $LAMI$:= $[\pm 45/0_2]_{2s}$, $IGEO$:= 3	0.899	$\lambda_G = 1.059$, $\lambda_{sk} = 2.896$ $\lambda_1 = 3.657$
$a = 7.33$ in., $b = 4.4$ in., $h = 0.49375$ in., $t_s = 0.096$ in., $LAMI$:= $[\pm 45/0_2]_{2s}$, $IGEO$:= 6	0.903	$\lambda_G = 1.313$, $\lambda_{sk} = 1.156$ $\lambda_3 = 2.278$

Table 4.16 Best designs obtained by genetic algorithm for grid-stiffened curved Panel 2, with $N_y = 0$.

Design variables	Weight lbs/ft^2	Buckling load factors
$a = 4.4$ in., $b = 6.2857$ in., $h = 0.440$ in., $t_s = 0.084$ in., $LAMI$:= $[\pm 45/90]_{2s}$, $IGEO$:= 4	0.759	$\lambda_G = 1.017$, $\lambda_{sk} = 1.329$ $\lambda_3 = 1.425$
$a = 7.33$ in., $b = 4.0$ in., $h = 0.440$ in., $t_s = 0.084$ in., $LAMI$:= $[\pm 45/90]_{2s}$, $IGEO$:= 4	0.764	$\lambda_G = 1.003$, $\lambda_{sk} = 1.681$ $\lambda_3 = 1.262$
$a = 4.0$ in., $b = 4.0$ in., $h = 0.360$ in., $t_s = 0.060$ in., $LAMI$:= $[\pm 45/0/90]_{2s}$, $IGEO$:= 4	0.913	$\lambda_G = 1.020$, $\lambda_{sk} = 4.885$ $\lambda_3 = 1.171$
$a = 4.4$ in., $b = 6.2857$ in., $h = 0.360$ in., $t_s = 0.084$ in., $LAMI$:= $[\pm 45/0/90]_{2s}$, $IGEO$:= 4	0.925	$\lambda_G = 1.005$, $\lambda_{sk} = 3.038$ $\lambda_3 = 1.783$
$a = 5.5$ in., $b = 6.2857$ in., $h = 0.360$ in., $t_s = 0.084$ in., $LAMI$:= $[\pm 45/0/90]_{2s}$, $IGEO$:= 4	0.908	$\lambda_G = 0.992$, $\lambda_{sk} = 2.406$ $\lambda_3 = 1.572$
$a = 6.2857$ in., $b = 7.33$ in., $h = 0.360$ in., $t_s = 0.084$ in., $LAMI$:= $[\pm 45/0_2]_{2s}$, $IGEO$:= 5	0.959	$\lambda_G = 1.025$, $\lambda_{sk} = 3.148$ $\lambda_1 = 11.539$, $\lambda_3 = 1.364$,
$a = 4.4$ in., $b = 7.33$ in., $h = 0.320$ in., $t_s = 0.084$ in., $LAMI$:= $[\pm 45/0/90]_{2s}$, $IGEO$:= 5	0.965	$\lambda_G = 1.007$, $\lambda_{sk} = 4.494$ $\lambda_1 = 11.152$, $\lambda_3 = 1.909$,
$a = 4.889$ in., $b = 6.2857$ in., $h = 0.360$ in., $t_s = 0.084$ in., $LAMI$:= $[\pm 45/90_2]_{2s}$, $IGEO$:= 5	0.995	$\lambda_G = 1.071$, $\lambda_{sk} = 4.656$ $\lambda_1 = 5.420$, $\lambda_3 = 1.549$,

Table 4.17 Best designs obtained by genetic algorithm for grid-stiffened curved Panel 3, with $N_y = 0$.

Design variables	Weight lbs/ft^2	Buckling load factors
$a = 6.2857$ in., $b = 4.0$ in., $h = 0.5375$ in., $t_s = 0.096$ in., $LAMI$:= $[\pm 45/90]_{2s}$, $IGEO$:= 6	0.976	$\lambda_G = 1.005$, $\lambda_{sk} = 1.271$ $\lambda_3 = 1.529$
$a = 6.2857$ in., $b = 4.4$ in., $h = 0.5375$ in., $t_s = 0.102$ in., $LAMI$:= $[\pm 45/90]_{2s}$, $IGEO$:= 6	0.983	$\lambda_G = 1.014$, $\lambda_{sk} = 1.045$ $\lambda_3 = 1.721$
$a = 6.2857$ in., $b = 4.0$ in., $h = 0.51875$ in., $t_s = 0.102$ in., $LAMI$:= $[\pm 45/90]_{2s}$, $IGEO$:= 6	0.986	$\lambda_G = 0.979$, $\lambda_{sk} = 1.320$ $\lambda_3 = 1.813$
$a = 6.2857$ in., $b = 4.4$ in., $h = 0.0.51875$ in., $t_s = 0.102$ in., $LAMI$:= $[\pm 45/90]_{2s}$, $IGEO$:= 6	0.970	$\lambda_G = 0.954$, $\lambda_{sk} = 1.094$ $\lambda_3 = 1.845$
$a = 4.4$ in., $b = 4.889$ in., $h = 0.0.5$ in., $t_s = 0.102$ in., $LAMI$:= $[\pm 45/90_2]_{2s}$, $IGEO$:= 5	1.215	$\lambda_G = 0.980$, $\lambda_{sk} = 5.899$ $\lambda_1 = 1.215$, $\lambda_3 = 5.583$

Table 4.18 Buckling loads of best design for Panel 3 subjected to load case of Panel 1 and 2 (no hoop tension).

	Load Case (lbs/in.)	Buckling load factors
(Panel 1)	$N_x = 1250$, $N_y = 0$, $N_{xy} = 250$.	$\lambda_G = 1.797$, $\lambda_{sk} = 1.279$, $\lambda_3 = 1.380$ (Global buckling at $\lambda_G = 1.797$)
(Panel 2)	$N_x = 300$, $N_y = 0$, $N_{xy} = 1350$.	$\lambda_G = 2.467$, $\lambda_{sk} = 1.393$, $\lambda_3 = 0.697$ (Local buckling at $\lambda_3 \times \lambda_G$) = 1.719

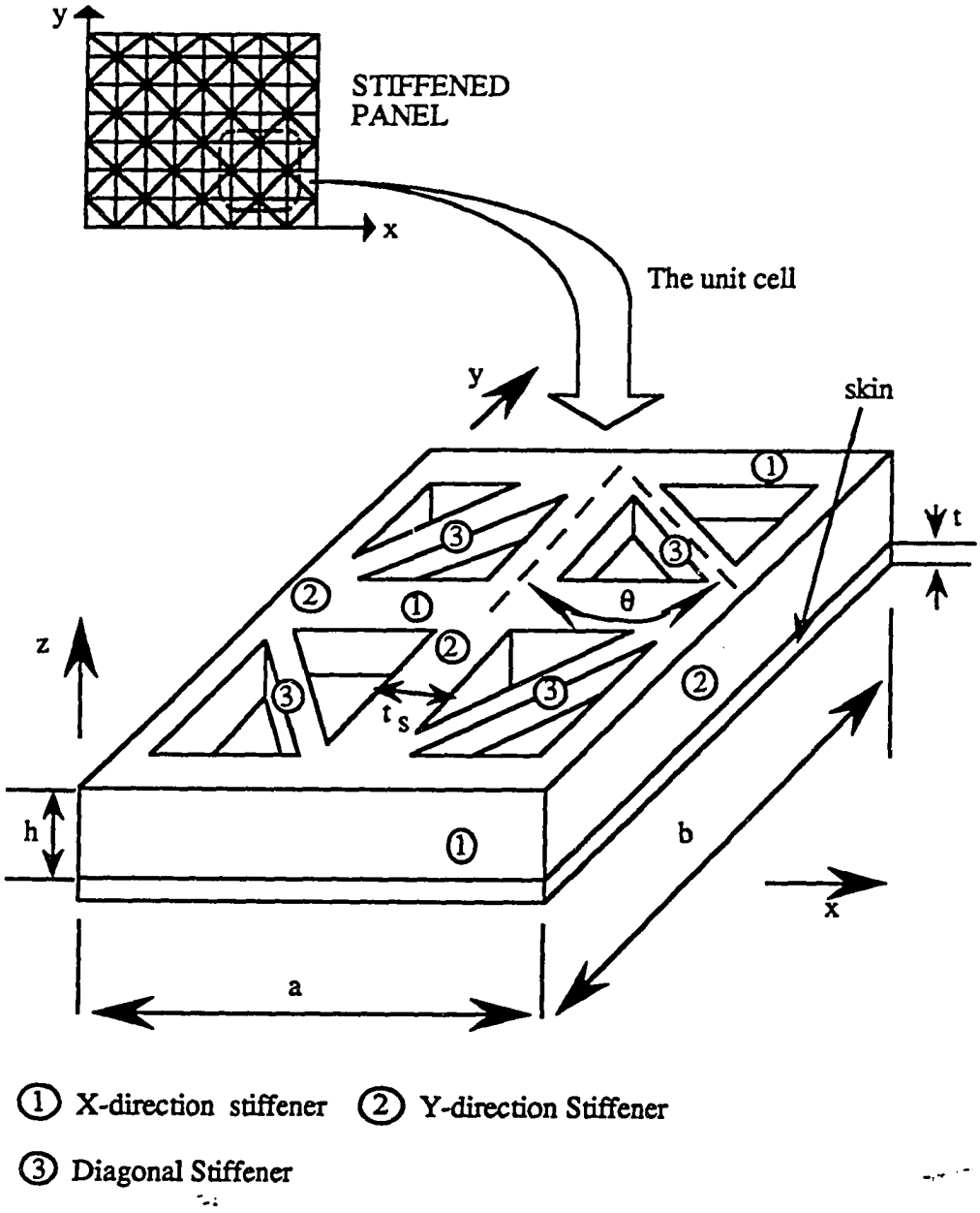

Figure 4.1 Unit cell of grid-stiffened panel showing design variables.

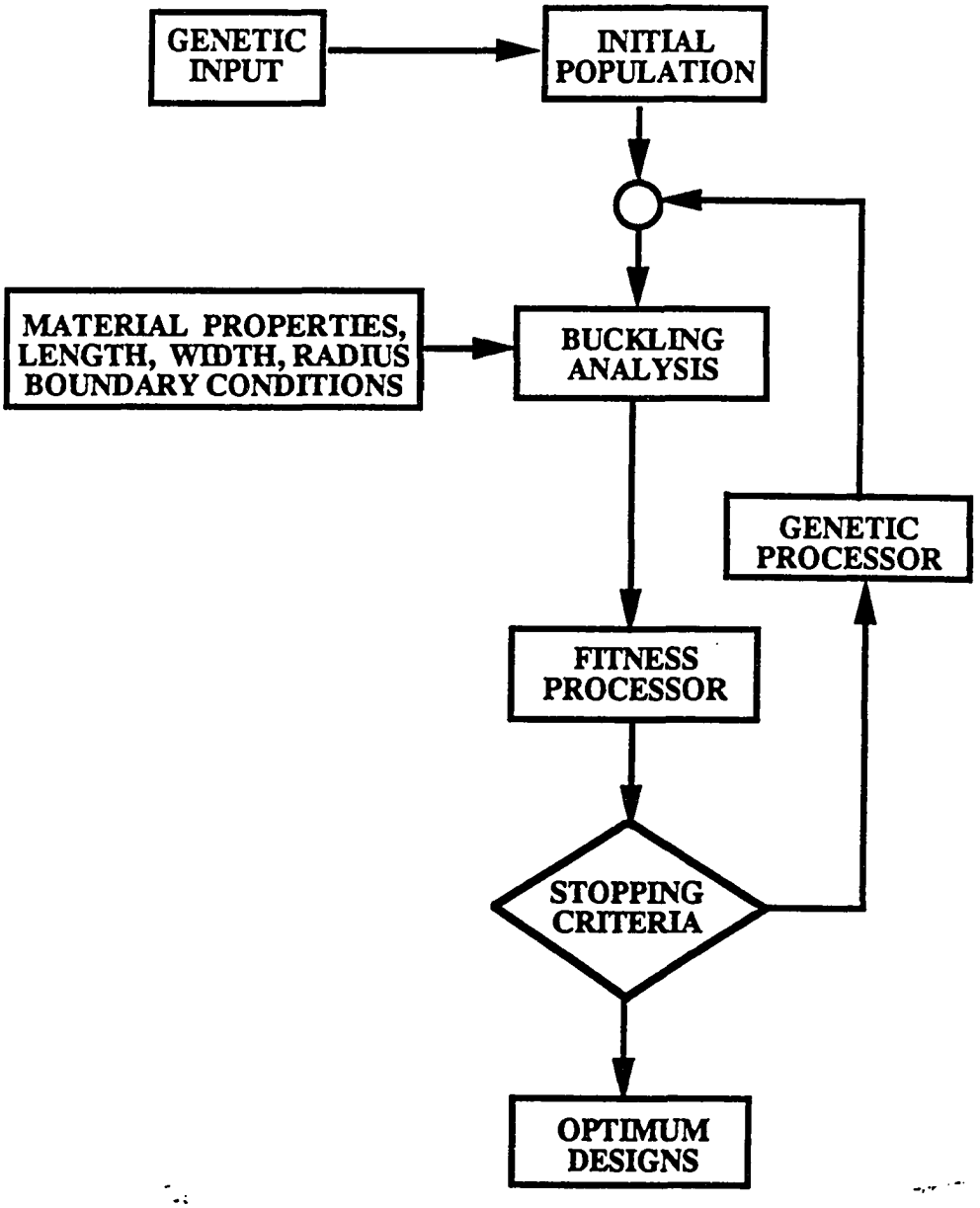

Figure 4.2 Flow chart for the optimization using the genetic algorithm.

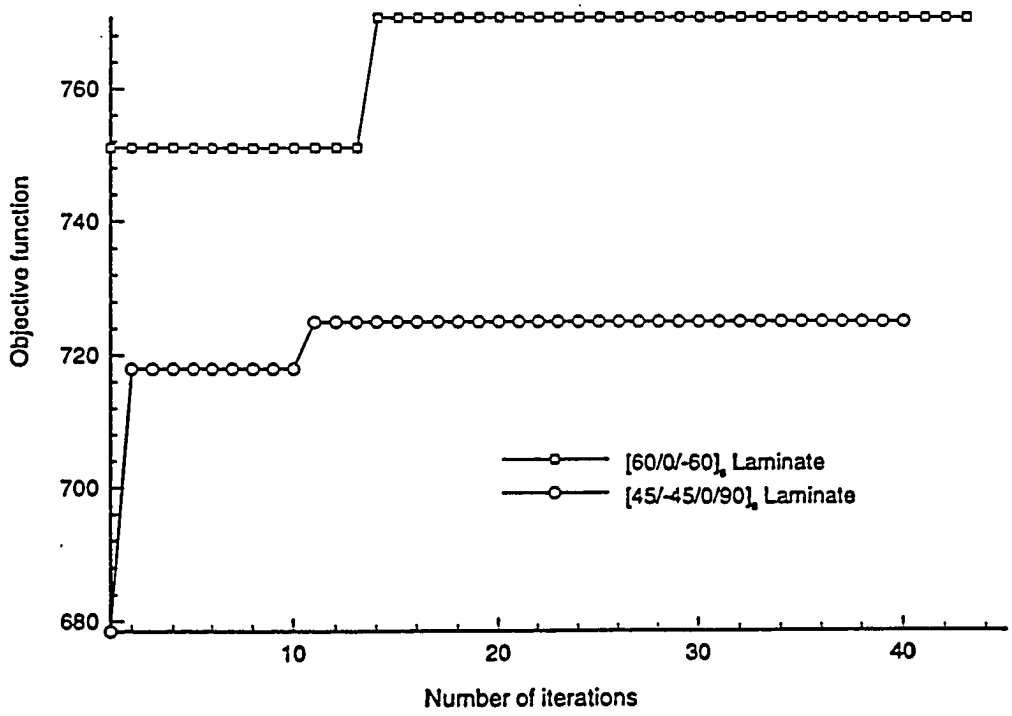

Fig. 4.3 Design convergence for composite grid-stiffened flat panels.

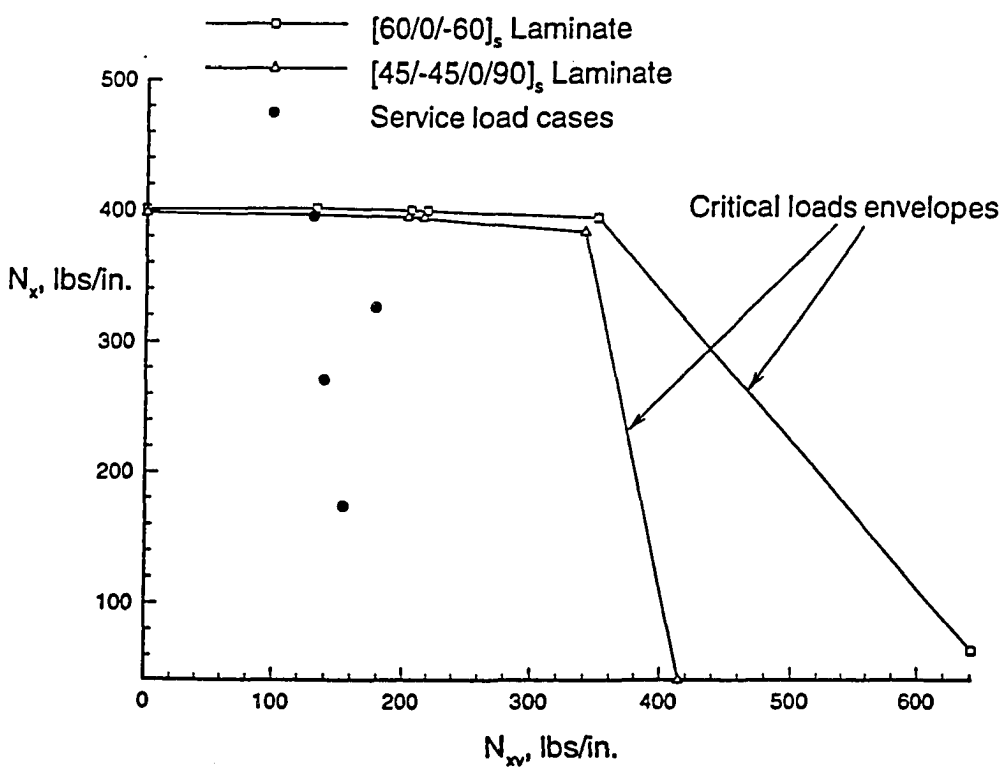

Fig. 4.4 Buckling loads for grid-stiffened panels.

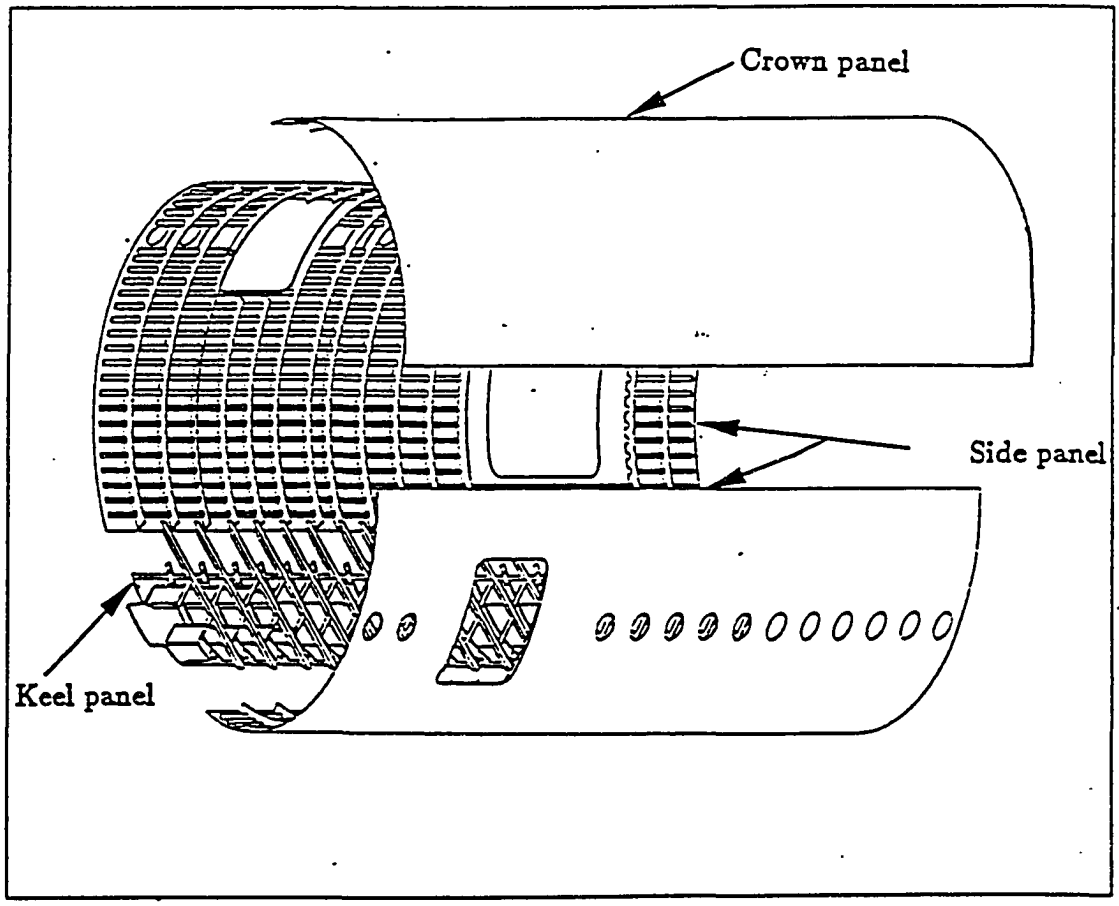

Fig. 4.5 Quadrant approach to fuselage design.

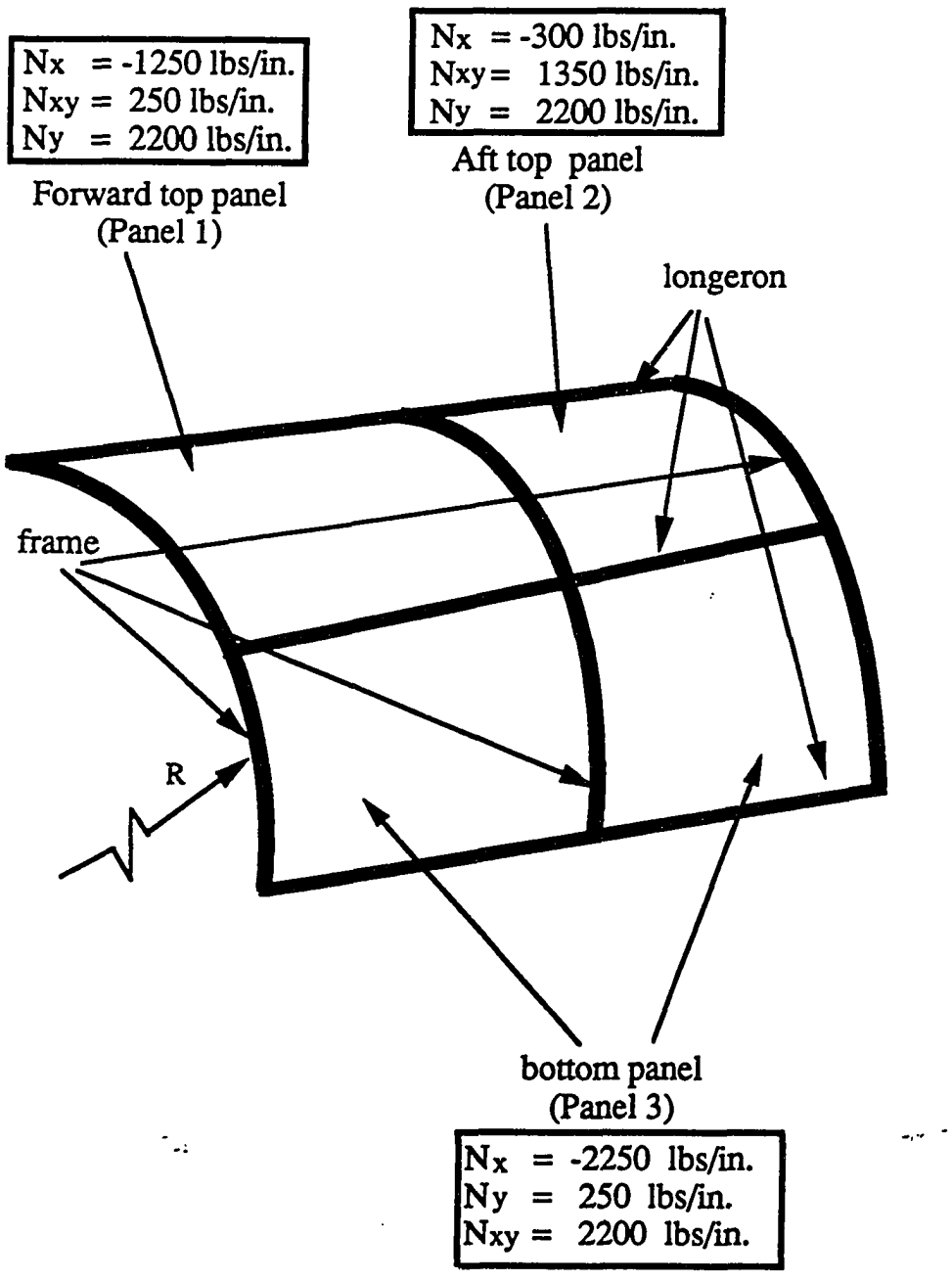

Figure 4.6 Side quadrant panel of fuselage.

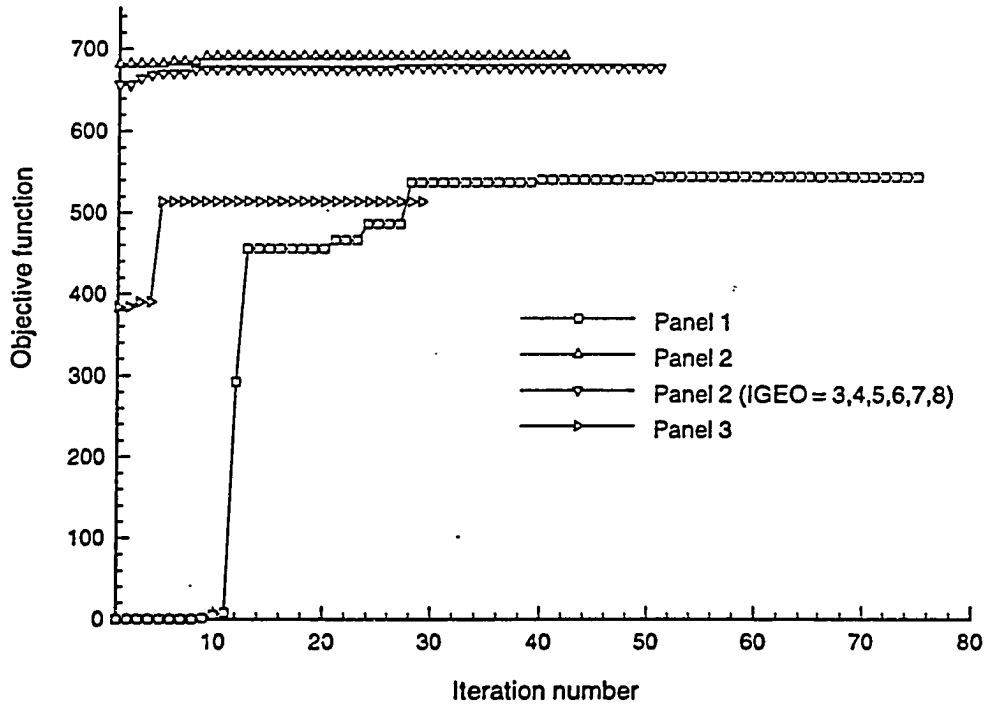

Fig. 4.7 Design convergence for composite grid-stiffened curved panels.

Chapter 5

CONCLUDING REMARKS

5.1 SUMMARY

The aim of the present work was to develop and validate a set of analytical tools for design and analysis of composite grid-stiffened panels exhibiting global buckling for aircraft primary structures. Global and local analyses were developed and used in order to assess grid-stiffened panels for global buckling subjected to combined in-plane loadings. The analysis tools were incorporated in an optimization procedure based on the genetic algorithm to provide a discrete design variable optimizer design code, capable of preliminary design of composite grid-stiffened panel for aerospace structural applications.

The global analysis adopted was an improved smeared stiffener theory, which accounts for the local skin-stiffener interactions for blade stiffeners. Including the local skin-stiffener interactions is important, since the traditional smeared stiffener theory may overestimate buckling loads within a range of geometric parameters. The skin-stiffener interaction is accounted for by computing the stiffness due to the stiffener and the skin in the skin-stiffener region about a shift in the neutral axis at the stiffener. The location of the neutral surface is obtained from a theoretical study of the skin-stiffener interface of a semi-infinite stiffened panel. A stress function approach, with the principle of minimum potential energy, is used in the theoretical study wherein

the axial strain in the stiffener is assumed to equal the strain in the skin at the edge of the stiffener. Numerical results are presented for simply supported grid-stiffened panels of different stiffening geometry, and are compared with those obtained from detailed finite element analysis as well as with those from the traditional smeared stiffener theory.

The local analyses required for assessing the global buckling of grid-stiffened panel are that of determining the buckling response of anisotropic panels with general parallelogram-shaped and general-triangular shaped planforms, and that of determining the buckling response of stiffener segments. Buckling response of stiffener segments is assessed using the stiffener crippling analysis presented in Reference [9]. Analysis method for buckling of anisotropic panels with general parallelogram-shaped and general triangular-shaped planforms are developed using a Rayleigh-Ritz technique and a minimum energy principle. The buckling analysis of these quadrilaterals and triangular planforms is enhanced by mapping their physical domain into a computational domain. Bilinear finite element shape functions in natural coordinates are used in the case of quadrilateral planforms and linear finite element shape functions in area coordinates are used in the case of triangular planforms. The transformation from physical domain to computational domain facilitates the computation of linear stiffness matrices and geometric stiffness matrices and also the imposition of boundary conditions. The Rayleigh-Ritz functions are formulated in natural coordinates for each planform geometry.

The Rayleigh-Ritz functions consists of the product of distribution functions (regular polynomials or Legendre polynomial) and circulation functions which are used to impose different boundary conditions along each edge of the panel. Each circulation function is the product of the equation of each edge raise to an independent exponent for each displacement component of the computational domain of the triangular or quadrilateral geometry.

Regular polynomials and Legendre Polynomials are used for quadrilateral geometry, and for triangular geometry only regular polynomials are used. The strain-displacement relations used account for a first-order, shear-deformation theory to be used with the minimum energy principle and also allow different shell theories to be used through tracers coefficients. The Ritz function accounts for material anisotropy. Numerical results were obtained for isotropic, orthotropic, and anisotropic skewed plates and are compared with existing solutions and finite element solutions. The effect of transverse shear deformations is also studied for isotropic and anisotropic skewed plates. Results for triangular plates were presented for equilateral triangle, right-angled isosceles triangles, and $30° - 60° - 90°$ triangle with isotropic and anisotropic material properties, and with different boundary conditions. Results are compared with existing solutions, and the effect of transverse shear deformation for isotropic and anisotropic triangular plates are studied. Finally, numerical results for anisotropic curved panels subjected to axial compression are obtained using Sanders-Koiter, Love's, and Donnell's shell theory and are compared with those obtained using the STAGS finite element code ([29]).

The global and local buckling analyses were incorporated in a genetic algorithm optimizer to provide a design code involving discrete optimization for optimal design of grid-stiffened panel with a global buckling constraint. The design variables include the axial and transverse stiffener spacing, the stiffener height and thickness, the skin-laminate stacking sequence, and the stiffening geometry. The design problem was to minimize the weight per unit area of a composite grid-stiffened panel given the loading condition, the length, width and radius of the panel, the material properties of the skin and stiffener, and the boundary conditions of the panel. The design constraints on the panel include a global buckling constraint which does not allow localized buckling of skin or stiffener segments. Also constraints on the stiffener spacings, stiffener aspect ratio, and skin thicknesses, which may be due to manufacturing

requirements are imposed through proper selection of the design space explored by the genetic algorithm. Results are presented for simply supported flat and curved composite grid-stiffened panels.

5.2 CONCLUSIONS

- The improved smeared stiffener theory provides better correlation with detailed finite element analyses than the traditional smeared stiffener theory. Buckling loads obtained using the improved smeared stiffener theory are within eight percent or less compared to detailed finite element results. Hence, the design approach based on the improved smeared stiffener theory is a useful preliminary design tool.

- The analysis method developed for panels with general parallelogram-shaped quadrilateral and general triangular shaped planform provides accurate buckling solutions for isotropic and anisotropic skewed plates and also for the different triangular plates considered. The method does not exhibit any mesh distortion.

- The change in buckling coefficient is more pronounced as the skew angle increases for thin plates as well as thick plates.

- The buckling response of skewed plates is also affected considerably by material anisotropy. Results of the buckling coefficients for simply supported plates made of Laminate 1 and Laminate 2 shows that the buckling coefficients of Laminate 2 for the 45° skew angle case is about 30 percent less than those of Laminate 1 and Laminate 2 is about twice more anisotropic than Laminate 1.

- The buckling coefficient for skewed plates subjected to load cases with positive in-plane shear is higher than those with negative shear this effect increases with increasing material anisotropy even for moderate skew angle. For simply supported plate with 30° skew angle, the buckling coefficient with positive shear

load is 30 percent higher than the buckling coefficient with negative shear load. The corresponding percentage increase for Laminates 1 and 2 is 36 and 44 percent respectively.

- The buckling response of triangular plates with in-plane shear loads depends on the symmetry of the triangular geometry and the degree of material anisotropy. For the equilateral triangular plate, the buckling load with positive in-plane shear load is 1.1 times the buckling load with negative in-plane shear load for Laminate 1 where as for Laminate 2, the buckling load with positive in-plane shear is 1.3 times the buckling load with negative in-plane shear load. For the right-angled isosceles triangles, the buckling load with in-plane shear load is 1.4 and 1.6 times the buckling load with negative in-plane shear for Laminates 1 and 2, respectively.

- Results indicate the importance of including transverse-shear deformation in the design of skin laminate for grid-stiffened panels, since the thickness-to-width ratio for skin segments of grid-stiffened panel is about 0.025.

- Results obtained for anisotropic curved panels subjected to axial compression using Sanders-Koiter, Love's, and Donnell's shell theory show that Sanders-Koiter or Love's shell theories gives results that are in good agreement with finite element analysis results. Results from Donnell's theory are in agreement with results from other theories when the displacement components in the deformed configuration are rapidly varying function of the circumferential coordinate. Such a variation of displacement occurs for panels with large R/t ratio ($R/t >$ 200). When a panel deforms with more than two half-waves occurs in the curved direction, the displacement can be considered as rapidly varying. Results for isotropic panels also shows that the difference in buckling loads obtained from Donnell's theory and other theories is not due to material anisotropy.

- The results obtained from the optimization using the global and local analyses and the genetic algorithm indicate that the stiffening configuration depends mostly on the load case to which the panel is subjected to.

- For most combined load cases, the best design have diagonal stiffeners. In certain cases, the best design may not be suitable for structural application due to other considerations. In such a case, the pool of good designs obtained by the genetic algorithm may be considered.

5.3 RECOMMENDATIONS FOR FUTURE WORK

- Other considerations for the design of grid-stiffened panel such as damage tolerance capability can be included as additional objective functions or constraints in the genetic optimization.

- The buckling analysis method developed should be extended in order to analyze buckling of variable-radius cylindrical shells which consist of two or more curved segments, each with a constant, but different, radius. These types of panels are more representative of fuselage structures. Such an analysis can be achieved by imposing continuity of displacements and rotations at the intersection of the segments. Alternatively, Ritz functions, that cover the whole of the variable-radius panel can be employed, and the linear and geometric stiffness matrices can be computed from integration over each segment at a time.

- A discrete analysis using Lagrange multipliers ([22]) to impose compatibility between skin and stiffeners can be developed using Ritz functions with circulation functions, to account for material anisotropy and different boundary conditions. The three-dimensional deformation of the stiffener can be accounted to some extent to provide more accurate modeling of the stiffener response.

- The effect of pressure loading on grid-stiffened panel should be investigated by developing an appropriate analysis tool.
- The stress at the skin-stiffener interface due to combined loads can be studied by using a semi-infinite skin-stiffener model similar to the model used in developing the improved smeared stiffener theory.

REFERENCES

[1] Rehfield, L. W, and Reddy, A. D., "Design Information for Continuous Advanced Composite Isogrid Structure," Proceedings of Fifth DoD/NASA Conference on Fibrous Composites in Structural Design, NADC-81096-60, Naval Air Development Center, 1981, Vol 1.11, pp. 113-143.

[2] Rehfield, L. W., Deo, R. B., and Renieri, G., "Continuous Filament Advanced Composite Isogrid: A Promising Structural Concept," Fibrous Composites in Structural Design, Plenum Publishing Corporation, 1980, pp. 215-239.

[3] Rouse M., and Ambur D. R., "Damage Tolerance of a Geodesically Stiffened Advanced Composite Structural Concept for Aircraft Structural Applications," Presented at the Ninth DoD/NASA/FAA Conference on Fibrous Composite in Structural Design, Lake Tahoe, Nevada, November 4-7, 1991.

[4] Rehfield, L. W., Chang, S., Zischka, P. J., Prickings, R. D., and Holl M. W., "Tailoring of Composite Wing Structure for Elastically produced Camber Deformation," Proceedings of 32nd AIAA/ASME/ASCE/AHS/ASC Structures, Structural Dynamics and Materials Conference, AIAA Paper No, 91-1186, April 8-10 1991, Baltimore, MD, Part 3, pp. 2123-2127.

[5] Ambur, D., and Rehfield, L. W., "Effect of Stiffness Characteristics on the Response of Composite grid-stiffened Structures," AIAA Paper No. AIAA-91-1087-CP., 1991.

[6] Stroud, W. J., Greene, W. H., and Anderson, M. S., "Buckling Results of Stiffened Panels Subjected to Combined Longitudinal Compression and Shear: Results Obtained with PASCO, EAL and STAGS Computer Programs," NASA TP 2215, 1984.

[7] Gendron, G., and Gurdal, Z., Optimal Design of Geodesically Stiffened Composite Cylindrical Shell. AIAA Paper No. 92-2306-CP, 1992.

[8] Rao, K. P., and Tripathy, B., "Stiffened Composite Cylindrical Panels-Optimum Lay-up for Buckling by Ranking," *Computers and Structures,* Vol. 42, No. 4, 1992, pp. 481-488.

[9] Reddy, A. D., Valisetty, Rao R., and Rehfield, L. W., "Continuous Filament Wound Composites Concepts for Aircraft Fuselage Structures," *AIAA Journal of Aircraft*, Vol. 22, No. 3, March 1985, pp. 249-255.

[10] Troitsky, M. S., Stiffened Plates, Bending, Stability and Vibrations, Elsvier Scientific Publishing Company, 1976.

[11] Timoshenko, S. P. and Gere, J. W., Theory of Elastic Stability, Second Edition, McGraw-Hill Inc., 1961.

[12] Brush, D. O., and Almroth, B. O., Buckling of Bars, Plates and Shells, McGraw-Hill, Inc., 1975.

[13] Dow, N. F., Libove, C., and Hubka, R. E, "Formulas for Elastic Constants of Plates with Integral Waffle-like Stiffening," NACA RM LS3E1 3a, August 1953.

[14] Hoppmann, W. H., Huffington, N. J., and Magness, L. S., "A Study of Orthogonally Stiffened Plates," *ASME Journal of Applied Mechanics*, Vol. 23, No. 3, Sept. 1956, pp. 343-350.

[15] Huffington, N. J., "Theoretical Determination of Rigidity Properties of Orthogonally Stiffened Plates," *ASME Journal of Applied Mechanics*, Vol. 23, No. 1, March 1956, pp. 15-20.

[16] Baruch, M., and Singer, J., "Effect of Eccentricity of Stiffeners on the General Stability of Stiffened Cylindrical Shells Under Hydrostatic Pressure," *Journal of Mechanical Engineering Science*, Vol. 5, No. 1, 1963, pp. 23-27.

[17] Jaunky, N., "Elastic Buckling of Stiffened Composite Curved Panel," Old Dominion University, Norfolk, Virginia, Master's Thesis, August 1991.

[18] Shames, I. H., and Dym, C. L., Energy and Finite Element Methods in Structural Mechanics, Hemisphere Publishing Company, 1985.

[19] Tulk, J. D., and Walker, A. C., "Model Studies of the Elastic Buckling of a Stiffened Plate," *Journal of Strain Analysis*, Vol. 11, No. 3, 1976, pp. 137-144.

[20] Eivind, S., "Elastic Buckling and Postbuckling of Eccentrically Stiffened Plates," *International Journal of Solids and Structures*, Vol. 25, No. 7, 1989, pp. 751-768.

[21] Wang, J. T. S., and Hsu, T. M., "Discrete Analysis of Stiffened Composite Cylindrical Shells", *AIAA Journal*, Vol. 23, No 11, Nov. 1985, pp. 1753-1761.

[22] Phillips, J. L. and Gurdal, Z., "Structural Analysis and Optimum Design of Geodesically Stiffened Composite Panels," Report CCMS-90-05, Center for Composite Materials and Structures, Virginia Polytechnic Institute and State University, Blacksburg, Virginia, July 1990.

[23] Marguerre, K., "Stability of Cylindrical Shell of Variable Curvature," NACA TM 1302, 1946.

[24] Sheinman, I. and Frier, M., "Buckling Analysis of Laminated Cylindrical Shells with Arbitrary Noncircular Cross Section," *AIAA Journal*, Vol. 32, No. 3, March 1994, pp. 648-661.

[25] Leriche, R., and Haftka, R. T., "Optimization of Laminate Stacking Sequence for Buckling Load Maximization by Genetic Algorithm," *AIAA Journal*, Vol. 31, No. 5, May 1993, pp. 951-956.

[26] Smith, C. B., Heebink, T. B., and Norris, C. B., "The Effective Stiffness of a Stiffener Attached to a Flat Plywood Plate," United States Department of Agriculture, Forest Products Laboratory, Report No. 1557, Sept. 1946

[27] Jones, M. R., Mechanics of Composite Materials, McGraw-Hill Book Company, 1975.

[28] Anon., Mathematical and Statistical Software at Langley, Central Scientific Computing Complex, Document N-3, NASA Langley Research Center, April 1984.

[29] Brogan, F. A., Rankin, C. C., and Cabiness, H. D., "STAGS User Manual," Lockheed Palo Alto Research Laboratory, Report LMSC P032594, 1994.

[30] Anon., "DIAL Finite Element Analysis System - Version L3D2," Lockheed Missiles and Space Company, July 1987.

[31] Wang, C. M., Liew, K. M., and Alwis, W. A. M., "Buckling of Skew Plates and Corner Condition for Simply Supported Edges," *ASCE Journal of Engineering Mechanics Division,* Vol. 118, No. 4, April 1992, pp. 651-662.

[32] Smith, J. P., "General Plate Stability using High Order Techniques," AIAA Paper No. 92-2283-CP, 1992.

[33] Smith, J. P., "BUCKY - A Finite Element Program for Plate Program for Analysis," AIAA Paper No. 94-1391, 1994.

[34] Taylor, J. L., "Buckling and Vibration of Triangular Flat Plates," *Journal of the Royal Aeronautical Society,* Vol. 71, October 1967, pp. 727-728.

[35] Klitcheiff, J. M., "Buckling of Triangular Plates by Shearing Forces," *Quarterly Journal of Mechanics and Applied Mathematics*, Vol. 4, Part 3, 1951, pp. 257-259.

[36] Wittrick, W. H., "Symmetrical Buckling of Right-Angled Isosceles Triangular Plates," *The Aeronautical Quarterly*, Vol. 5, August 1953, pp. 131-143.

[37] Pan, Li-Chow, "Equilibrium Buckling and Vibration of $30^o - 60^o - 90^o$ Triangular Plate Simply Supported at the Edges," *Acta Phys. Sin.*, Vol. 3, No. 12, 1956, pp. 215-245.

[38] Reipert, Z. "Application of Simple Functional Series to the Solution of Problems Concerning Statics, Stability and Vibration of Plates having Non-typical Forms," *Archiwum Mechaniki Stosowanej*, Vol. 6, No. 15, Warszawa, 1963, pp. 791-814.

[39] Valisetty, R. R. and Reddy, A. D., "Design Data and Buckling of Laminated Composite Triangular Plates," SAE Technical Paper Series, SP-623, April 1985, pp. 25-29.

[40] Bucco, D. Mazumdar, J., and Sved, G., "Vibration Analysis of Plates of Arbitrary Shape - A New Approach,"*Journal of Sound and Vibration*, Vol. 67, No. 2, 1979, pp.-253-262.

[41] Kim, C. S. and Dickinson, S. M., "The Free Flexural Vibration of Right Triangular Isotropic and Orthotropic Plates," *Journal of Sound and Vibration*, Vol. 141, No. 2, 1990, pp. 291-311.

[42] Singh, B. and Chakraverty, S., "Transverse Vibration of Plates using Characteristic Orthogonal Polynomials in Two Variables," *International Journal of Mechanical Sciences,* Vol. 34, No. 12, 1992, pp. 947-955.

[43] Xiang, Y., Liew, K. M., Kitipornchai, S., and Wang, C. M., "Vibration of Triangular Mindlin Plates Subjected to Isotropic In-Plane Stresses," *Journal of Vibration and Acoustics*, Vol. 116, 1994, pp. 61-66.

[44] Liew, K. M., Lam, K. Y., and Chow, S. T., "Study on Flexural Vibration of Triangular Composite Plates Influenced by Fibre Orientation," *Composite Structures,* Vol. 13, 1989, pp. 123-132.

[45] Bert, C. W., and Birman, V., "Parametric Instability of Thick, Orthotrpic, Circular Cylindrical Shells," *Acta Mechanica*, Vol. 71, 1988, pp. 61-76.

[46] Sanders, J. L. Jr., "An Improved First Approximation Theory for Thin Shells," NASA Report R-24, 1959.

[47] Koiter, W. T., "A Consistent First Approximation in General Theory of Thin Elastic Shells," The Theory of Thin Elastic Shells, Proceedings IUTAM Symposium, Delft, 1959, pp. 12-33, 1960, Amsterdam, the Netherlands, North-Holland Publishing Company.

[48] Love, A. E. H., A Treatise on the Mathematical Theory of Elasticity, 4th edition, New York, Dover Publication, 1927.

[49] Loo, T. T., "An Extension of Donnell's Equation for Circular Cylindrical Shell," *Journal of Aeronautical Sciences*, Vol. 24, 1957, pp. 390-391.

[50] Stein, M., "Nonlinear Theory for Plates and Shells Including the Effects of Transverse Shearing," *AIAA Journal*, Vol. 24, No. 9, September 1986, pp. 1538-1544.

[51] Stein, M., and Neff, J., "Buckling Stresses of Simply Supported Rectangular Flat Plates in Shear," NACA TN 1222, March 1947.

[52] Stein, M., and Batdorf, S. B., "Critical Combinations of Shear and Direct Stresses for Simply Supported Rectangular Flat Plates," NACA TN 1223, March 1947

[53] Andrews, C. L., Special Functions for Engineers and Applied Mathematicians, Macmillan Publishing Company, 1985, pp. 116-165.

[54] Aminpour, M. A., "An Assumed-Stress Hybrid 4-Node Shell Element with Drilling Degrees of Freedom," *International Journal for Numerical Methods in Engineering,* Vol. 33, 1992, pp. 19-38.

[55] Williams, F. W., Anderson, M. S., Kennedy, D., Butler, R., Aston, G., and Hoh., S., M., "An Exact Analysis and Optimum Design Program Covering the Buckling and Vibration of Prismatic Assemblies of Flat In-Plane Loaded, Anisotropic Plates, with Approximations for Curved and Tapered Plates, Discrete Supports and Transverse Stiffeners - User Manual for VICONOPT," NASA CR - 181966, Release 1.2, January 1993.

[56] Wittrick, W. H., "Buckling of Oblique Plates with Clamped Edges under Uniform Compression," *The Aeronautical Quarterly,* Vol. 4, February 1953, pp. 151-163.

[57] Durvasula, S., "Buckling of Clamped Skew Plates," *AIAA Journal,* Vol. 8, No. 1, 1970, pp. 178-181.

[58] Kitipornchai, S., Xiang L., Wang, C. M., and Liew, K. M., "Buckling of Thick Skew Plates," *International Journal for Numerical Method in Engineering,* Vol. 36, 1993, pp. 1299-1310.

[59] Fried, I. and Schmitt, K. H., "Numerical Results from the Application of Gradient Iterative Techniques to the Finite Element Vibration and Stability Analysis of Skew Plates," *Aeronautical Journal,* March 1972, Vol. 76, pp. 166-169.

[60] Edwardes, R. J. and Kabaila, A. P., "Buckling of Simply Supported Skew Plates," *International Journal for Numerical Methods in Engineering,* Vol. 12, 1978, pp. 779-785.

[61] Mizusawa, T., Kajita, T., and Naruko, M., "Analysis of Skew Plate Problems with Various Constraints," *Journal of Sound and Vibrations,* Vol. 73, No. 4, 1980, pp. 575-584.

[62] Kennedy, J. B. and Prabhakara, M. K., "Combined-Load Buckling of Orthotropic Skew Plates," *ASCE Journal of the Engineering Mechanics Division,* Vol. 105, No. EM1, February, 1979, pp. 71-79.

[63] Green, A. E., "Double Fourier Series and Boundary Value Problems," *Proceedings of the Cambridge Philosophical Society,* Vol. 40, 1944, pp. 222-228.

[64] Nemeth, M. P., "Nondimensional Parameters and Equations for Buckling of Anisotropic Shallow Shells," *ASME Journal of Applied Mechanics,* Vol. 61, September 1994, pp. 664-669

[65] Problem proposed by Professor Issac Elishakoff of Florida Atlantic University and communicated by Dr. David Bushnell of Lockheed Martin. Private communication, Nov. 1995.

[66] Nagendra, S., Haftka, R. T., and Gurdal, Z., " Design of a Blade Stiffened Composite Panel by Genetic Algorithm," Proceedings of 34th AIAA/ASME/ASCE/AHS/ASC Structures, Structural Dynamics and Materials Conference, Paper No. 93-1584-CP, April 1993, La Jolla, CA, pp. 2418-2436.

[67] Anderson, M. S., Stroud, W. J., Durling, B. J., and Hennessy, K. W., "PASCO: Structural Panel Analysis and Sizing Code. User's Manual," NASA TM 80182, November 1981.

[68] Rouse, M., and Ambur, D. R., "Damage Tolerance and Failure Analysis of a Geodesically Stiffened Structure Loaded in Axial Compression," AIAA Paper No. 94-1534, Proceedings of the 35th AIAA/ASME/ASCE/AHS/ASC Structures, Structural Dynamics, and Materials Conference, Hilton Head, South Carolina, April 18-21, 1994.

[69] Whitney A. S., "Formulation of Genetic Algorithm for the Evolution of Engineering Designs," Composite Curved Panel," Old Dominion University, Norfolk, Virginia, Master's Thesis, May 1995.

[70] Wolfram, S., Mathematica, A system for doing mathematics by computer, Second edition, Addison-Wesley Publishing Company, Inc. 1991.

APPENDIX A

INTEGRATION SCHEMES FOR STIFFNESS MATRICES

The integration schemes for computing the linear and geometric stiffness matrices are presented and discussed here. The schemes make use of symbolic and numerical computations to achieve computational efficiency. This approach is necessary since cumbersome integrations result in the use of polynomials as Ritz functions. Integration schemes are presented for the use of regular polynomials, which are used in the buckling analyses of panels with parallelogram-shaped quadrilateral and general triangular-shaped planforms. Also, integration schemes are presented for Ritz functions involving Legendre polynomials which are also used for in the buckling analysis of panels with parallelogram-shaped quadrilateral planform.

A.1 TYPES OF INTEGRALS

The buckling analyses presented in Chapter 3, involve a Rayleigh-Ritz formulation with the minimum potential energy principle, and hence, the linear and geometric stiffness matrices are developed from the strain energy as shown in Chapter 3. Furthermore, since a first-order, shear-deformation theory is used, the integrals involve only first derivatives of the Ritz functions as shown in Equation (3.31) and (3.41).

The types of integrals encountered are

$$\int_A R_i R_j \, d\xi d\eta \tag{A.1}$$

$$\int_A R_{i,\xi} R_j \, d\xi d\eta \tag{A.2}$$

$$\int_A R_{i,\eta} R_j \, d\xi d\eta \tag{A.3}$$

$$\int_A R_{i,\xi} R_{j,\xi} \, d\xi d\eta \tag{A.4}$$

$$\int_A R_{i,\xi} R_{j,\eta} \, d\xi d\eta \tag{A.5}$$

$$\int_A R_{i,\eta} R_{j,\eta} \, d\xi d\eta \tag{A.6}$$

where R_i and R_j can be any of U_i, V_i, W_i, Φ_{xi}, Φ_{yi}, and U_j, V_j, W_j, Φ_{xj}, Φ_{yj}, respectively, in Equation (3.31) and (3.41). These integrals correspond to the integration over the computational domain. Only the integration scheme for the integral of Equation (A.4) will discussed, since others are similar.

A.2 SCHEME FOR QUADRILATERALS

The Ritz functions for quadrilaterals are written in natural coordinates (ξ, η), and consists of circulation function and regular polynomials or Legendre polynomials. Therefore Equation (A.4) can be written as

$$\int_A R_{i,\xi} R_{j,\xi} \, d\xi d\eta = \left(\int_{-1}^{1} f(\xi) d\xi \right) \left(\int_{-1}^{1} g(\eta) d\eta \right) = I_\xi \, I_\eta$$

where

$$I_\xi = \int_{-1}^{1} \left[(1-\xi)^{p_i} (1+\xi)^{r_i} X_i(\xi) \right]_{,\xi} \left[(1-\xi)^{p_i} (1+\xi)^{r_i} X_j(\xi) \right]_{,\xi} d\xi$$

$$I_\eta = \int_{-1}^{1} (1-\eta)^{q_i} (1+\eta)^{s_i} Y_i(\eta) \, (1-\eta)^{q_i} (1+\eta)^{s_i} Y_j(\eta) \, d\eta \tag{A.7}$$

and

$$X_i, \, X_j = \xi^{m_i}, \, \xi^{m_j} \text{ or } P_{m_i}(\xi), \, P_{m_j}(\xi)$$

$$Y_i, \, Y_j = \eta^{n_i}, \, \eta^{n_j} \text{ or } P_{n_i}(\eta), \, P_{n_j}(\eta) \tag{A.8}$$

The limits of the integration are from -1 to $+1$ since ξ and η are natural coordinates.

A.2.1 Regular Polynomials

In the case of regular polynomials, the integral I_ξ of Equation (A.7) can be expanded as

$$\begin{aligned} I_\xi = \int_{-1}^{1} \{ & r_l(1-\xi)^{p_l}(1+\xi)^{r_l-1}\xi^{m_i} + m_i(1-\xi)^{p_l}(1+\xi)^{r_l}\xi^{m_i-1} \\ & + p_l(1-\xi)^{p_l-1}(1+\xi)^{r_l}\xi^{m_i}\} \times \\ & \{r_t(1-\xi)^{p_t}(1+\xi)^{r_t-1}\xi^{m_j} + m_j(1-\xi)^{p_t}(1+\xi)^{r_t}\xi^{m_j-1} \\ & + p_t(1-\xi)^{p_t-1}(1+\xi)^{r_t}\xi^{m_j}\}\, d\xi \end{aligned} \tag{A.9}$$

which can be written as

$$\begin{aligned} I_\xi = \int_{-1}^{1} & \Big(\sum_{h=1}^{3} a_{ih}\,(1-\xi)^{e1_{ih}}\,(1+\xi)^{e2_{ih}}\,\xi^{e3_{ih}} \Big) \\ & \times \Big(\sum_{s=1}^{3} a_{js}\,(1-\xi)^{e1_{js}}\,(1+\xi)^{e2_{js}}\,\xi^{e3_{js}} \Big) d\xi \end{aligned} \tag{A.10}$$

The coefficients a_{ih} and a_{js}, and exponents $e1_{ih}$, $e2_{ih}$, $e3_{ih}$, $e1_{js}$, $e2_{js}$, $e3_{js}$ in Equation (A.10) are obtained by comparing terms with Equation (A.9).

The next step is to determine the integral of the form

$$I_1 = \int_{-1}^{1} (1-\nu)^{k1}(1+\nu)^{k2}\nu^{k3}\, d\nu \tag{A.11}$$

which can be used in two computational loops to evaluate the integral of Equation (A.10). Symbolic computations using Mathematica ([70]) are obtained here to evaluate integral of the type of Equation (A.11). For any $k1$, $k2$ and $k3$, Mathematica evaluate integral I_1 as

$$\begin{aligned} I_1 = (-1)^{k3} & \frac{H_{2F1}[-k1,(1+k3),(2+k2+k3),-1]\;\Gamma(1+k2)\;\Gamma(1+k3)}{\Gamma(2+k2+k3)} \\ & + \frac{H_{2F1}[-k2,(1+k3),(2+k1+k3),-1]\;\Gamma(1+k1)\;\Gamma(1+k3)}{\Gamma(2+k1+k3)} \end{aligned} \tag{A.12}$$

where H_{2F1} is the $Hypergeometric2F1[a,b,c,z]$ function ([53]) with $z=-1$, and

$$Hypergeometric2F1[a,b,c,z] = \sum_{n=0}^{\infty} \frac{(a)_n\,(b)_n}{(c)_n}\frac{z^k}{k!} \tag{A.13}$$

where the symbol $()_n$ is the Pochhammer symbol ([53]) and

$$(a)_0 = 1, \quad (a)_n = a\,(a+1)...\,(a+n-1), \quad n = 1,2,3,... \tag{A.14}$$

$\Gamma(m)$ is the Euler gamma function ([53]), and $\Gamma(m) = (m-1)!$ for m being a positive integer. However, the H_{2F1} function and $\Gamma(m)$ tend to be computationally expensive for large values of $k3$. Since the value of the exponent of $(1 \pm \xi)$ and $(1 \pm \eta)$ is either zero or one, $k1$ and $k2$ can assume values of 0, 1, or 2 only. The maximum value of $k3$ depends on the order of polynomial being used in the buckling analysis. Therefore, the integral of Equation (A.11) is evaluated for all nine possible combinations of $k1$ and $k2$, in terms of $k3$, using Mathematica. The results of the symbolic computations using Mathematica is shown below;

$$\begin{aligned}
k1 = 0,\ k2 = 0; \quad & I_1 = \frac{1}{(1+k3)} + \frac{(-1)^{1+k3}}{(1+k3)} \\
k1 = 1,\ k2 = 0; \quad & I_1 = \frac{1}{(1+k3)(2+k3)} + \frac{(-1)^{k3}(3+2\,k3)}{(1+k3)(2+k3)} \\
k1 = 2,\ k2 = 0; \quad & I_1 = \frac{2}{(1+k3)(2+k3)(3+k3)} - \frac{(-1)^{k3}(-14-16\,k3-4\,k3^2)}{(1+k3)(2+k3)(3+k3)} \\
k1 = 0,\ k2 = 1; \quad & I_1 = \frac{(-1)^{k3}}{(1+k3)(2+k3)} + \frac{(3+2\,k3)}{(1+k3)(2+k3)} \\
k1 = 0,\ k2 = 2; \quad & I_1 = \frac{2(-1)^{k3}}{(1+k3)(2+k3)(3+k3)} + \frac{(14+16\,k3+4\,k3^2)}{(1+k3)(2+k3)(3+k3)} \\
k1 = 1,\ k2 = 1; \quad & I_1 = \frac{2}{(1+k3)(3+k3)} + \frac{2\,(-1)^{k3}}{(1+k3)(3+k3)} \\
k1 = 2,\ k2 = 1; \quad & I_1 = \frac{1}{(1+k3)} - \frac{1}{(2+k3)} - \frac{1}{(3+k3)} + \frac{1}{(4+k3)} - \\
& \qquad (-1)^{k3}\left(\frac{-1}{(1+k3)} - \frac{1}{(2+k3)} + \frac{1}{(3+k3)} + \frac{1}{(4+k3)}\right) \\
k1 = 1,\ k2 = 2; \quad & I_1 = \frac{1}{(1+k3)} + \frac{1}{(2+k3)} - \frac{1}{(3+k3)} - \frac{1}{(4+k3)} - \\
& \qquad (-1)^{k3}\left(\frac{-1}{(1+k3)} + \frac{1}{(2+k3)} + \frac{1}{(3+k3)} - \frac{1}{(4+k3)}\right) \\
k1 = 2,\ k2 = 2; \quad & I_1 = \frac{8}{(15+23\,k3+9\,k3^2+k3^3)} + \frac{8(-1)^{k3}}{(15+23\,k3+9\,k3^2+k3^3)}
\end{aligned} \tag{A.15}$$

Using these symbolic computations, the integral of Equation (A.11) can be evaluated based on the values of $k1$ and $k2$.

An outline of the algorithm for computing the integral of Equation (A.7) is then

- Computation of I_ξ
  1. compute a_{ih}, $e1_{ih}$, $e2_{ih}$, $e3_{ih}$ from p_l, r_l, m_i.
  2. compute a_{js}, $e1_{js}$, $e2_{js}$, $e3_{js}$ from p_t, r_t, m_j.
  3. using two computational loops with indices h and s, compute

$$I_\xi = \int_{-1}^{1} \sum_{h=1}^{3} \sum_{s=1}^{3} a_{ih} a_{js} (1-\xi)^{e1_{ih}+e1_{js}} (1+\xi)^{e2_{ih}+e2_{js}} \xi^{e3_{ih}+e3_{js}} d\xi \quad \text{(A.16)}$$

  using the symbolic computations of Equation (A.15).

- Computation of I_η
  1. compute I_η using Equation (A.15)

$$I_\eta = \int_{-1}^{1} (1-\eta)^{q_l+q_t} (1+\eta)^{s_l+s_t} \eta^{n_i+n_j} d\eta \quad \text{(A.17)}$$

- Compute $I_\xi \times I_\eta$

The value of the integral of Equation (A.7) is $I_\xi I_\eta$. Other integrals (Equations (A.1) - (A.6)) are computed in a similar way.

A.2.2 Legendre Polynomials

When using Legendre polynomials, the integral of Equation (A.7) can be written as

$$\int_{-1}^{1} [\, (c_{\xi l}\xi^2 + d_{\xi l}\xi + e_{\xi l}) P_{m_i}(\xi) \,]_{,\xi} [\, (c_{\xi t}\xi^2 + d_{\xi t}\xi + e_{\xi t}) P_{m_j}(\xi) \,]_{,\xi} \, d\xi \times$$
$$\int_{-1}^{1} (c_{\eta l}\eta^2 + d_{\eta l}\eta + e_{\eta l}) P_{n_i}(\eta) (c_{\eta t}\eta^2 + d_{\eta t}\eta + e_{\eta t}) P_{n_j}(\eta) \, d\eta$$
$$= I_{p\xi} \, I_{p\eta} \quad \text{(A.18)}$$

since the exponent of $(1 \pm \xi)$ and $(1 \pm \eta)$ can be either zero or one. The coefficients $c_{\eta l}$, $d_{\eta l}$, $e_{\eta l}$, $c_{\eta t}$, $d_{\eta t}$, $e_{\eta t}$, $c_{\xi l}$, $d_{\xi l}$, $e_{\xi l}$, $c_{\xi t}$, $d_{\xi t}$, and $e_{\xi t}$, depend on the exponents of $(1 \pm \xi)$ and $(1 \pm \eta)$. After expansion, $I_{p\xi}$ can be written as

$$\begin{aligned} I_{p\xi} &= \int_{-1}^{1} [\, (a_{\xi l}\xi + b_{\xi l})P_{m_i}(\xi) + (c_{\xi l}\xi^2 + d_{\xi l}\xi + e_{\xi l})P'_{m_i}(\xi) \,] \times \\ &\quad [\, (a_{\xi t}\xi + b_{\xi t})P_{m_j}(\xi) + (c_{\xi t}\xi^2 + d_{\xi t}\xi + e_{\xi t})P'_{m_j}(\xi) \,]\, d\xi \end{aligned} \tag{A.19}$$

Next the properties of Legendre polynomials ([53]) are used to write Equation (A.18) and (A.(19) in a more appropriate form for analytical integration. The properties of Legendre polynomial ($P_n(\nu) = P_n$) are

$$P_{-n} = P_{(|n|-1)} \tag{A.20}$$

$$\nu P'_n = nP_n + P'_{n-1} \tag{A.21}$$

$$\nu P_n = \frac{(n+1)}{(2n+1)}P_{n+1} + \frac{n}{(2n+1)}P_{n-1} \tag{A.22}$$

$$\nu^2 P'_n = \frac{n(n+1)}{(2n+1)}P_{n+1} + \frac{n^2}{(2n+1)}P_{n-1} + (n-1)P_{n-1} + P'_{n-2} \tag{A.23}$$

$$\nu^2 P_n = \frac{(n+1)}{(2n+1)} \{ \frac{(n+2)}{(2n+3)}P_{n+2} + \frac{(n+1)}{(2n+3)}P_n \} \tag{A.24}$$

$$+ \frac{n}{(2n+1)} \{ \frac{n}{(2n-1)}P_n + \frac{(n-1)}{(2n-1)}P_{n-2} \} \tag{A.25}$$

$$P_n = \frac{P'_{n+1} - P'_{n-1}}{(2n+1)} \tag{A.26}$$

Two other useful properties are

$$\int_{-1}^{1} P_n P_m \, d\nu = \begin{cases} 0 \text{ for } n \neq m \\ \frac{2}{2n+1} \text{ for } n = m \end{cases} \tag{A.27}$$

$$\int_{-1}^{1} P'_n P'_m \, d\nu = \begin{cases} 0 \text{ for } (n+m) \text{ odd} \\ n(n+1) \text{ for } (n+m) \text{ even} \end{cases} \quad n \leq m \tag{A.28}$$

Hence, using Equation (A.21) - (A.26), the following relations can be established;

$$
\begin{aligned}
[\,(c\,\nu^2 + d\,\nu + e)\,P_n\,]_{,\nu} \;=\; & \\
& \frac{a(n+1)}{(2n+1)(2n+3)}P'_{n+2} \;+ \\
& \frac{(b+nd)}{(2n+1)}P'_{n+1} \;+ \\
& \Big(\frac{a\,n}{(2n+1)(2n-1)} - \frac{a(n+1)}{(2n+1)(2n+3)} + e\Big)P'_n \;+ \\
& \Big(d - \frac{(b+nd)}{(2n+1)}\Big)P'_{n-1} \;+ \\
& \Big(c - \frac{a\,n}{(2n+1)(2n-1)}\Big)P'_{n-2} \\
= \;& \sum_{k=1}^{5} \alpha_{dk} P'_{n_{\alpha dk}} \qquad \text{(A.29)}
\end{aligned}
$$

$$
\begin{aligned}
[\,(c\,\nu^2 + d\,\nu + e)\,P_n\,] \;=\; & \\
& \frac{c(n+1)(n+2)}{(2n+1)(2n+3)}P_{n+2} \;+ \\
& \frac{d(n+1)}{(2n+1)}P_{n+1} \;+ \\
& \Big(\frac{c(n+1)(n+2)}{(2n+1)(2n+3)} + \frac{c\,n^2}{(2n+1)(2n-1)} + e\Big)P_n \;+ \\
& \frac{dn}{(2n+1)}P_{n-1} \;+ \\
& \frac{c(n-1)n}{(2n+1)(2n-1)}P_{n-2} \\
= \;& \sum_{k=1}^{5} \alpha_k P_{n_{\alpha k}} \qquad \text{(A.30)} \\
= \;& \frac{\alpha_1}{(2n+5)}P'_{n+3} + \frac{\alpha_2}{(2n+3)}P'_{n+2} \;+ \\
& \Big(\frac{\alpha_3}{(2n+1)} - \frac{\alpha_1}{(2n+5)}\Big)P'_{n+1} \;+ \\
& \Big(\frac{\alpha_4}{(2n-1)} - \frac{\alpha_2}{(2n+3)}\Big)P'_n \;+ \\
& \Big(\frac{\alpha_5}{(2n-3)} - \frac{\alpha_3}{(2n+1)}\Big)P'_{n-1} \;- \\
& \frac{\alpha_4}{(2n-1)}P'_{n-2} - \frac{\alpha_5}{(2n-3)}P'_{n-3} \\
= \;& \sum_{k=1}^{7} \beta_{dk} P'_{n_{\beta dk}} \qquad \text{(A.31)}
\end{aligned}
$$

Therefore, $I_{p\xi}$ from Equation (A.18) is

$$I_{p\xi} = \int_{-1}^{1} \sum_{h=1}^{5} \sum_{s=1}^{5} \alpha_{idh}\ \alpha_{jdh} P'_{m_{\alpha idk}} P'_{m_{\alpha jdk}}\ d\xi \tag{A.32}$$

and Equation (A.28) is used to evaluate each integral in the summation and Equation (A.20) is used when Legendre polynomials with negative indices occur. $I_{p\eta}$ is

$$I_{p\xi} = \int_{-1}^{1} \sum_{h=1}^{5} \sum_{s=1}^{5} \alpha_{ih}\ \alpha_{jh} P_{m_{\alpha ik}} P_{m_{\alpha jk}}\ d\eta \tag{A.33}$$

and Equation (A.27) is used to evaluate each in integral in the summation. If $I_{p\eta}$ is simplified using Equation (A.31), then Equation (A.28) is used to evaluate each integral in the summation. Finally, $I_{p\eta} \times I_{p\xi}$ evaluates integral of the type of Equation (A.4). Equation (A.31) is necessary when evaluating integrals of the type of Equation (A.2), (A.3), and (A.5).

A.3 SCHEME FOR TRIANGLES

The integration schemes used in the buckling analysis of panel with triangular geometry is similar to that of the buckling analysis of panel with quadrilateral geometry. Equation (A.4) for triangular geometries is

$$\begin{aligned} I_{T\xi\xi} \;=\; & \int_0^1 \int_0^1 [\ \xi^{p_i}\eta^{q_i}(1-\xi-\eta)^{r_i}\xi^{m_i}\eta^{n_i}\ ]_{,\xi} \times \\ & [\ \xi^{p_i}\eta^{q_i}(1-\xi-\eta)^{r_i}\xi^{m_j}\eta^{n_j}\ ]_{,\xi}\ d\xi d\eta \end{aligned} \tag{A.34}$$

The limits of the integration is from 0 to 1 since ξ and η are area coordinates. The expression in the square bracket in Equation (A.34) can be written in a general form as

$$\begin{aligned} [\ \xi^a\eta^b(1-\xi-\eta)^c\ ]_{,\xi} \;&=\; a\ \xi^{a-1}\eta^b(1-\xi-\eta)^c \;-\; c\ \xi^a\eta^b(1-\xi-\eta)^{c-1} \\ &=\; \sum_{h=1}^{2} \alpha_h xi^{a_h}\eta^{b_h}(1-\xi-\eta)^{c_h} \end{aligned} \tag{A.35}$$

Hence,

$$I_{T\xi\xi} = \int_0^1 \int_0^1 \sum_{h=1}^{2} \sum_{s=1}^{2} \alpha_{ih}\alpha_{js}\ \xi^{a_{ih}+a_{js}}\eta^{b_{ih}+c_{js}}(1-\xi-\eta)^{c_{ih}+c_{js}}\ d\xi d\eta \tag{A.36}$$

Each integral in the summation of Equation (A.36) is evaluated using

$$\int_0^1 \int_0^1 \xi^a \eta^b (1-\xi-\eta)^c d\xi d\eta \;=\; \frac{a!\; b!\; c!}{(a+b+c+2)!} \tag{A.37}$$

Other types of integral are evaluated in a similar way.